

# $\mu$ -reactors for Heterogeneous Catalysis

Robert Jensen

May 2012



# Preface

The work presented here have been carried out at the Technical University of Denmark (DTU), Department of Physics, at the Center for Individual Nanoparticle Functionality (CINF) from August 2008 to May 2012 with Professor Ib Chorkendorff as my supervisor and Professor Ole Hansen as co-supervisor. CINF is funded by the Danish National Research Foundation which is greatly acknowledged for its support for this project.

I have so far had a wonderful time at CINF, and the list of people to thank seems endless, but I will nevertheless give it a try.

First and very much most of all, I would like thank my family and friends. Especially my wonderful wife and best friend in the world, Sine, and our children Gro and Sia. The three of you are by far the most important part of my life. Your help and support during this project is of infinite importance to me!

I would of course very much like to thank my supervisor, Ib. Even though we both can have our rather strong opinions on various issues, I think we somehow always manage to find common ground in the end. You have provided excellent help and support during the entire project and it has been a pleasure to work with you.

All clean-room work has been performed by Thomas Pedersen, and without his efforts, not a single measurement would ever have been performed. Together with Ole Hansen, you are in my world simply known as the clean-room wizards. The two of you seem to have answers to almost any question and are always able to come up with solutions for all kinds of problems and later implement them as actual products. The importance of clean-room work in this project simply cannot be overestimated.

An overwhelming amount of gratitude should be expressed towards our mechanical and electronic workshops, especially Dan, Peter, Peder and Anders. Without your help, most of this work would not have been possible.

Working at CINF is a truly joyful experience, very much because of the many good colleagues at the department. I would like to thank basically everybody, but a few people needs to be specifically mentioned. Jane Nielsen, now our head of department, was the person who originally hired me at DTU and later acted as the catalyst that turned me into a Ph.D. student. Without Jane this thesis would never have existed. Ole Trinhammer was my colleague for almost two years in Nanoteket, and I am grateful to have been able to work with you. Anders Nierhoff has produced all the cluster samples for the various experiments, for that I would also like to say thanks. Peter Vesborg was one of the original inventors of the  $\mu$ -reactor platform, and your willingness to share your wealth of experience with the platform is very much appreciated. Mathias Kjærgaard Christensen has been a master student at the setup for the last year, and have done a wonderful job in the period, you have been a productive member of the team as well as a good friend. Of course all other people at

---

CINF should also be mentioned, however it is just a bit too many and thus I will just give a collective thank you to everybody.

At this point two CINF people might consider themselves forgotten in this list, but no, I just saved the best for last. Thomas Andersen and Kenneth Nielsen, even though my social skills are nowhere good enough tell you in person, at least I can write it here; you are simply fantastic! Thomas has been first my lab neighbor and later joined the  $\mu$ -reactor team when we started building the NG setup. Kenneth has been my office neighbor and over the years this great neighborliness has provided infinite amounts of procrastinations. I owe you both a very big thanks for making the last four years such a great time.

Finally, I would like to thank Erik Bækgaard, Bent Selchau, Peter Thorsen and certainly not least Steen Bach for introducing me to the wonderful world of science!

# Abstract

This thesis is the summary of my work on the  $\mu$ -reactor platform. The concept of  $\mu$ -reactors is presented and some of the experimental challenges are outlined. The various experimental issues regarding the platform are discussed and the actual implementation of three generations of the setup is described in detail. Since heating and temperature measurement is an extremely important point in heterogeneous catalysis an entire chapter is dedicated to this subject. Three different types of heaters have been implemented and tested both for repeatability and homogeneity of the heating as well as the maximal achievable temperature. The currently best solution for heating and measuring temperature is to use several integrated Pt-strips as ohmic heaters and a separate 4-point Pt meander structure as a resistance thermometer.

It is shown how it is possible to quantify the available amount of active catalyst surface area by reacting off an adsorbed layer of oxygen with CO. This procedure can be performed at temperatures low enough that sintering of Pt nanoparticles is not an issue.

Some results from the reactors are presented. In particular an unexpected oscillation phenomenon of CO-oxidation on Pt nanoparticles are presented in detail. The sensitivity of the reactors are currently being investigated with CO oxidation on Pt thin films as a test reaction, and the results so far are presented. We have at this point shown that we are able to reach full conversion with a catalyst area of  $38 \mu\text{m}^2$  with a turn over frequency of approximately  $10^5 \text{ site}^{-1} \text{ s}^{-1}$ . The apparent activation energy for all sizes of thin films is found to be  $\sim 1.2 \text{ eV}$ . We expect to be able to go to even lower amounts of Pt and corresponding higher turn over frequencies by increasing the temperature further.

Various methods of gaining insight into the reactor besides the normal quadropole mass spectrometer are discussed. In particular a chapter is devoted to the application of a Time-of-flight mass spectrometer on the setup.

Finally the thesis contains an outlook of the possible future of the setup, and several suggestions for improvements are discussed.



# Dansk Resumé

I denne afhandling findes en gennemgang af mit arbejde på  $\mu$ -reaktorplatformen. Begrebet  $\mu$ -reakter introduceres og nogle af de eksperimentelle udfordringer gennemgås. De forskellige eksperimentelle forhold omkring platformen diskuteres og den fysiske implementering af tre generation af forsøgsplatformen gennemgås i detaljer. Da opvarmning og temperaturmåling er af afgørende betydning i heterogen katalyse, bruges et helt kapitel på gennemgang af dette. Tre forskellige metoder til opvarmning og temperaturmåling gennemgås, heraf er to af dem udviklet som en del af dette projekt. Opvarmningsmetoderne er testet både for repesterbarhed og homogenitet af opvarmningen såvel som for den højeste opnåelige temperaturer. Det er den nuværende opfattelse, at den bedste løsning på temperaturspørsgsmålet er at anvende flere separate integrerede Pt-strukturer som varmer via ohmsk opvarmning, samt en separat 4-punkts meander struktur som fungerer som et modstandstermometer.

Enkelte resultater af målinger med  $\mu$ -reaktorerne gennemgås. Specielt diskuteres et overraskende fænomen, hvor aktiviteten af Pt nanopartikler oscillerer i tid når partiklerne fungerer som katalysatorer for CO oxidation. Følsomheden er reaktorerne er i øjeblikket ved at blive undersøgt med CO oxidation som test-reaktion, og vi har foreløbig demonstreret fuld omsætning på en  $38 \mu\text{m}^2$  Pt tynd film. Dette giver en omsætning på omrent  $10^5 \text{ site}^{-1} \text{ s}^{-1}$ . Den tilsyneladende aktiveringsenergi er for alle film-størrelser målt til ca.  $\sim 1.2 \text{ eV}$ . Vi forventer at kunne måle på endnu mindre mænger at Pt og endnu højere omsætningshastigheder ved at hæve temperaturen yderligere.

Yderligere metoder til at opnå indsigt i de reaktioner som foregår i reaktoren diskuteres. Specielt er et helt kapitel dedikret til anvendelsen af Time-Of-Flight massspektromter på setup'et.

Endelig indeholder afhandlingen et kapitel med en kort gennemgang af en række forbedringer og udvidelser som man i fremtiden kunne forestille sig kunne bygges til  $\mu$ -reaktorplatformen.



# List of included papers

## Paper 1

Self-sustained carbon monoxide oxidation oscillations on size-selected platinum nano particles at atmospheric pressure

Submitted to Angewandte Chemie.

## Paper 2

High Mass Resolution Time of Flight Mass Spectrometer for Measuring Products in Heterogeneous Catalysis in Highly Sensitive Microreactors

Accepted for publication in Review of Scientific Instruments

## Paper 3

An Open Source Data Storage and Visualization Backend for Experimental Data

In preparation. To be submitted to Journal of the Association for Laboratory Automation.



# Contents

<b>1</b>	<b>Introduction</b>	<b>1</b>
1.1	The state of the world . . . . .	1
1.2	The impact of this project . . . . .	2
1.3	$\mu$ -reactors for Heterogeneous Catalysis . . . . .	3
1.4	Summary of this thesis . . . . .	4
<b>2</b>	<b>Experimental setup</b>	<b>5</b>
2.1	The $\mu$ -reactor platform . . . . .	5
2.1.1	Bonding . . . . .	6
2.2	General measurement principle . . . . .	7
2.3	Brief historical tour . . . . .	8
2.4	Next Generation . . . . .	10
2.4.1	The Tale of the Leaking O-rings . . . . .	11
2.4.2	Pneumatic valves . . . . .	13
2.4.3	Pumps . . . . .	14
2.4.4	Miscellaneous improvements . . . . .	14
2.4.5	Safety mechanisms . . . . .	15
2.5	Experiment automation . . . . .	16
2.6	Data storage . . . . .	18
<b>3</b>	<b>Temperature</b>	<b>19</b>
3.1	Temperature control . . . . .	19
3.2	Heating mechanisms . . . . .	20
3.3	Operating the RTD-heater . . . . .	22
3.4	Temperature profiles . . . . .	23
3.5	New heater . . . . .	25
<b>4</b>	<b>Measuring the Active Area of a Catalyst</b>	<b>29</b>
4.1	Procedure . . . . .	29
4.2	Area measurements of nanoparticles . . . . .	31

<b>5 Oscillating reactions</b>	<b>35</b>
5.1 Existing literature . . . . .	35
5.2 Experimental procedure . . . . .	37
5.3 Exploring the parameter space . . . . .	40
5.3.1 Temperature dependence . . . . .	41
5.3.2 Pressure and CO concentration dependence . . . . .	41
5.3.3 Size dependence . . . . .	44
5.4 Oscillation mechanism . . . . .	44
5.5 Conclusion . . . . .	45
<b>6 Sensitivity measurements</b>	<b>47</b>
6.1 Experimental procedure . . . . .	47
6.2 Data treatment . . . . .	49
6.2.1 Capillary flow . . . . .	49
6.2.2 Background signals . . . . .	50
6.2.3 Mass spectrometer calibration . . . . .	52
6.3 Results . . . . .	54
6.4 Lessons to be learned . . . . .	56
<b>7 Analytic techniques</b>	<b>57</b>
7.1 Feasibility study . . . . .	57
7.2 Postmortem analysis . . . . .	58
7.3 Non-bonded samples . . . . .	59
7.4 Optical methods . . . . .	60
7.5 Time-Of-Flight Mass Spectrometry . . . . .	61
<b>8 Time Of Flight Mass Spectrometry</b>	<b>63</b>
8.1 Instrumentation . . . . .	63
8.1.1 Vacuum components . . . . .	63
8.1.2 Electronics and data acquisition . . . . .	66
8.1.3 Ionization . . . . .	67
8.2 Data output . . . . .	68
8.3 Numerical model . . . . .	69
8.3.1 Simulation of the reflectron . . . . .	70
8.4 Results . . . . .	72
8.4.1 Benzene Hydrogenation . . . . .	72
8.4.2 Ammonia Oxidation . . . . .	74

<b>9 Hot Electron Devices</b>	<b>77</b>
9.1 Hot Electron Chemistry . . . . .	77
9.2 The Hot-Electron Device . . . . .	77
9.3 Experimental setup . . . . .	79
9.4 Results . . . . .	79
9.4.1 Hot Electron Chemistry . . . . .	80
9.4.2 Electron emission . . . . .	83
9.5 Conclusions on the hot electron project . . . . .	84
<b>10 Future plans</b>	<b>85</b>
<b>Bibliography</b>	<b>89</b>



# Chapter 1

## Introduction

### 1.1 The state of the world

The world is facing many challenges within the coming years. Oil prices are rising and so is the CO<sub>2</sub> level in the atmosphere. More and more countries become increasingly dependent on supplies of fossil fuels from fewer and fewer sources. And this is just to mention the problems being discussed in the popular media, in real life many other challenges are facing us. However, all of these problems can also be seen as interesting challenges that need new solutions, and this is where the scientific community steps in to hopefully provide solutions for some of these problems. Of course this will require inputs from many areas of research, heterogeneous catalysis is only a small part of this very large and complicated field.

It is an interesting thought, that we as humans actually already know and masters several technologies that can potentially solve large parts of the energy problem. Such solutions very much includes a long range of energy saving initiatives such as better insulation in housing, buildings with less demands for cooling, more tele-working reducing the demand for transportation etc. However, it seems to be a law of nature that despite all efforts to lower energy consumption, on average the consumption integrated over the entire world, inevitable goes up. This means that it will be necessary to find ways of getting access to cheap energy, preferably without resorting to fossil fuels even more polluting than what we are currently using.

In the field of energy technology, several candidates exists that are fully capable of providing substantial (if not complete) parts of the world's total energy needs. These technologies includes solar cells, solar-thermal electricity, hydro-power, nuclear power and wind turbines. All of these technologies have their pros and cons, however, as I am myself particular fond of wind turbines, I will take the liberty of using this technology as an example for a quick back-of-the-envelope calculation. The total energy consumption of the world is currently around 16 TW, but to make things simple we take it to be  $P_{world} = 20 \text{ TW}$ . A typical wind turbine at the moment would be around 3 to 4 MW<sub>peak</sub>. A standard value for the capacity factor (that is, the fraction of peak power that is on average produced by the turbine) is between 0.25 and 0.33 and thus it seems reasonable to take  $P_{turbine}^{sustained} = 1 \text{ MW}$ . These convenient choice of numbers provides us the number of wind turbines to satisfy the world's energy needs:

$$N_{WT} = \frac{20 \times 10^{12}}{1 \times 10^6} = 2 \times 10^7 \text{ wind turbines}$$

This number does not include energy storage loss. The design lifetime of almost all wind turbines on the market is 20 years (which in the real world seems to be a lower limit on the lifetime). Thus the required number of wind turbines pr. year is  $N_{WT}/y = 2 \times 10^7/20 = 10^6$  turbines. In units of peak power this corresponds to  $\sim 3 \times 10^6 \text{ MW}_{peak}$ . Currently the world's yearly wind turbine production is on the order of  $4.1 \times 10^4 \text{ MW}_{peak}$ [1], which means that with the current production rate, wind turbines will within 20 years produce on the order of 1% of the world's total energy demand.

As a rule of thumb, the price of the bare turbine, not including cabling and mounting, is around  $1.5 \times 10^6 \text{ €}/\text{MW}_{peak}$ . Typical prices for cabling and mounting end up with a total price between 2 and 5 times higher than this, obviously most expensive for sea based turbines. A conservative estimate of the total cost would thus be  $10^7 \text{ €}/\text{MW}_{peak}$ . It is straightforward to calculate an estimate of the yearly price for providing 100% wind energy to the entire world:

$$\text{Total cost} \sim 3 \times 10^6 \times 10^7 = 3 \times 10^{13} \text{ €/y}$$

not including storage loss.

For comparison the total world GDP[2] was approximately  $\sim 5.3 \times 10^{13} \text{ €}$ . This is only slightly more than the estimated price for 100% wind power energy. However, one should remember that this is an extremely rough estimate and just the fact that it comes out lower than the world GDB should justify a more thorough calculation on the subject, however this is luckily well outside the scope of this introduction. One thing to notice, however, is that the  $3 \times 10^{13} \text{ €/y}$  includes every single watt consumed by the world for any purpose. Realistically, the amount of power needed will be well lower than this since not all of the world's energy consumption is currently fossil. In 2011 'only' 81% of the energy consumption was from fossil resources (counting nuclear energy as non-fossil)[3].

Finally, it might be reasonable to ask not only to the economics but more relevant (and interesting) also to discuss the actual physical energy resource. Given enough money and good will, is the world even big enough to provide space for  $2 \times 10^7$  wind turbines of 3 MW? Luckily this question is easy to answer. As a rule of thumb, the energy density pr. area for wind turbines, is around  $8 \text{ MW}_{peak}/\text{km}^2$ . Using this number, we easily get an estimate of the required area:

$$A = \frac{2 \times 10^7 \times 3.5 \text{ MW}}{8 \text{ MW}/\text{km}^2} = 8.8 \times 10^6 \text{ km}^2$$

Corresponding to 1.8% of the area of the globe or 6% of the world's land area. All in all it is evident that it will not be impossible to provide energy to the world, given sufficiently political will. Wind turbines are just a single source of renewable energy, calculations similar to this could be performed for solar cells, solar thermal energy or nuclear power. In reality it will be optimal to mix the various energy forms both by type as well as by geographic location in order to minimize the storage demands. Calculations of the optimal mix of energy sources has not to my knowledge been carried out on world scale, but it has been done for the much simpler case of purely renewable electricity in Europe. In this case the optimal mix between wind and solar energy is calculated to be 55% wind turbines and 45% solar cells[4].

## 1.2 The impact of this project

When dealing with subjects as large as basically the future of the entire world, it is quite important to realize that the work of a single person is most likely rather insignificant in the

big picture. Thus it is always wise to make oneself quite clear what is the potential impact of ones work, just to get the proportions right. In my case, I have been working on a platform, not a specific system. Thus the potential impact of the work is to provide a platform that will help other people, who have specialized in various individual processes, to develop better catalysts. To make catalysis help providing solutions to some of the issues sketched above we should be able to find catalysts that either reduce the energy consumption of the world, increase the energy production or perhaps provide new and better ways for storing energy as well as releasing it when and where it may be desired.

On the lines of saving energy, a new ammonia catalyst could be an excellent contribution, currently a large fraction of the world's energy consumption is spent on ammonia production for fertilizers. On the lines of energy production, the catalysis community's part of a solution would most likely involve finding ways to exploit new resources in better ways. A hypothetical suggestion could be developing catalysts to produce liquid fuels from organic waste or perhaps even from algae or other sea-living organic material that might be available in large quantities, if humans start farming the ocean on a large scale. Finally, a good place for catalysis to help with constructive solutions could be in the area of energy storage and subsequent release at another time or place. This could be in the form of finding ways to scale down energy consuming processes (such as the mentioned ammonia production). With many smaller plants it would be much easier to use the energy at the time and place where energy is available, opposite to current large scale plants which need to run continuously to work efficiently. A more traditional type of storage would of course be the many projects currently working on creating liquid fuels or hydrogen, typically either by CO<sub>2</sub> reduction or water splitting, but also many other processes have been proposed. The concept is always to use the renewable resource, whenever it is available, to produce a product with high energy density. In this way the product can be stored easily and used later when the renewable resource is not producing sufficiently to satisfy demands.

### 1.3 $\mu$ -reactors for Heterogeneous Catalysis

As the title of this thesis indicates, the main focus is not so much on actual scientific results as it has been centered around creating a world-class experimental setup for testing many kinds of heterogeneous catalysis. This decision is taken both because this is my personal main interest and because these aspects of the system is not going to be covered anywhere else. It does not mean that the platform has not been used to do research. During my time at the setup, we have performed a long list of investigations, in close corporation with a number of bachelor, master and Ph.D. students, specializing in the individual processes. Thus the results from this work will eventually come out through their papers and theses.

The list of systems investigated during this period includes:

- CO oxidation on Pd nanoparticles and thin films
- Methanation on Pd nanoparticles and thin films
- HD-exchange reactions on ultra small Pt nano clusters of 10 and 20 atoms
- CO oxidation on Pt nano clusters of size 10 atoms up to 9 nm
- Methanation on Pt nanoparticles
- Ammonia oxidation on Pt nanoparticles

- Ammonia oxidation on various metal thin films
- Methanol synthesis on Cu thin films
- Methanol synthesis on Cu/Zn thin films

For most of this work the main focus has been on establishing correlations between structure and reactivity, typically in the form of size dependence of the catalyst for the particular reaction.

## 1.4 Summary of this thesis

This thesis is divided into several chapters. Here I will briefly outline the contents of the various parts.

**Chapters 2 and 3** These chapters contains all the technical discussions of the  $\mu$ -reactors and the setup in general. Here the reactors are introduced and the various technical issues are discussed. Chapter 2 covers everything except heating, which is then found in chapter 3.

**Chapter 4** In this chapter a method of estimating active surface area of a catalyst is presented. For various reasons, the area measurement is specific to a single type of system, in this case platinum.

**Chapter 5** Here I take detour from the main focus on the platform, and discuss an actual result. The data presented shows oscillations in reactivity of Pt nanoparticles during CO oxidation. We find that the nanoparticles will show reactivity oscillations of timescales from seconds up to more than an hour, even at atmospheric pressure.

**Chapter 6** Here we are on the borderline between platform characterization and real new data. The topic of the chapter is a measurement of the sensitivity of the setup, measured by CO oxidation on small platinum thin films. As far as the project has come at this point, we are entirely on the platform characterization part of the playing field. However, we have hopes that we will eventually be able to reach turn over frequencies so high, that we are able to see derivation from Arrhenius behavior. If we succeed in this, it will to my knowledge be the first time this has been measured for CO oxidation on platinum.

**Chapter 7 and 8** These chapters discuss some of the options to apply surface science methods to the system. In chapter 7 a long list of candidates is presented and in chapter 8 the successful application of Time-Of-Flight Mass Spectrometry to the  $\mu$ -reactors is shown.

**Chapter 9** A short chapter describing the first part of my Ph.D. which was about hot electron chemistry.

**Chapter 10** In the final chapter, I present my view of what could and should be the future of the  $\mu$ -reactor setup. Specifically I present a number of suggestions of various improvements that could be made to the platform.

# Chapter 2

## Experimental setup

### 2.1 The $\mu$ -reactor platform

The  $\mu$ -reactor platform is invented at CINF and is originally published in 2009 [5]. The device itself and the fabrication process is described in details in [6]. The clever idea about the design is that even though most of the incoming gas-flow is pumped away immediately, every molecule that actually enters the reactor area, will be led into the mass spectrometer resulting in very high sensitivity of the device. The design shows a number of advantages compared to a traditional catalytic reactors:

- The total volume of the reactor is just 236 nL, meaning that we are able to measure on very small amounts of catalyst. This could for example be samples produced in a cluster source.
- Only very small amounts of the reacting gasses needs to be mixed, meaning that explosive or otherwise dangerous mixtures can be measured without safety issues
- The thermal mass is very low. The temperature of the reactor can therefore be raised or dropped very quickly
- The glass lid of the reactor gives easy optical contact to the catalyst, meaning that the reactor can be used for photo catalysis. This has not been a part of my work, but other people at CINF are doing great photo catalytic work on the same platform.
- The diffusion length of the reactants and product gases in the reactor volume is almost an order of magnitude longer than the radius of the reactor volume ensuring full contact of the gas with the catalyst. We have tested this property by repeating CO oxidation measurements on small Pt spots located at different points in the the reactor, all spots are able to achieve full conversion showing that the gas is mixed in the reactor[7].

Of course the design also has its downsides, the most import problem is probably the fact that it is almost impossible to apply any traditional surface science techniques on the catalyst because the reactor is hermetically sealed and no easy way of opening the lid is known. Also the maximum temperature achievable is much lower than in traditional UHV-setups. We are ultimately limited by the melting point of the lid which is on the order of  $\sim 700^\circ\text{C}$ . Traditional UHV setups have no problems reaching temperatures well above  $1000^\circ\text{C}$ .

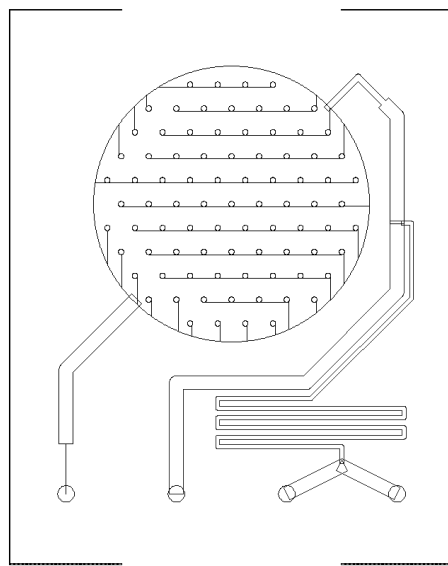


**Figure 2.1** – CAD drawing of the reactor design. Gas inflow happens from the two inlets to the right, which are connected to the mixing zone. The main flow exits through the main outlet (second hole from the left). The products leave the reactor through the capillary outlet furthest to the left.

The actual  $\mu$ -reactor chip is Si-based, clean room fabricated and has a size of 20x16.1 mm. The reactor consists of two inlets, a mixing zone allowing for diffusional mixing of reactants, an outlet, a reactor volume of 240 nL and a 5.4  $\mu$ m wide, 1500  $\mu$ m long capillary used for sniffing gases from the reactor volume. The mixing and outlet channels have a depth of 250  $\mu$ m, while the reactor and the capillary have a depth of 3  $\mu$ m. On top of the entire structure is grown a 50 nm layer of SiO<sub>2</sub> to act as an inert substrate for the catalyst under test.

### 2.1.1 Bonding

Once the reactor is made in the clean room and the wanted catalyst to be tested is deposited in the reactor volume, the sample of course needs to be sealed to form a complete reactor. This is done through the process of anodic bonding, which is thoroughly described in earlier theses from CINF group[8, 9, 6] and will only very briefly be described here. The point in anodic bonding is to hermetically seal a pyrex lid to a silicon wafer which is done by applying a high potential to the lid compared to the silicon and heat the structure to a temperature where the pyrex becomes ionically conducting which happens around  $\sim$ 280°C. In this configuration ions from the lid will be transported to the wafer and at the same time forming strong chemical bonds that seals the lid to the wafer. Once the bonding is complete it will be so strong that the interface will not be any weaker than the rest of the reactor structure. The bonded reactor has been tested to 5 bars of pressure, but it is most likely strong enough to contain much higher pressures. Unfortunately, no method of reversing the bonding process is known and the lid cannot be removed from the sample once the bonding is performed.

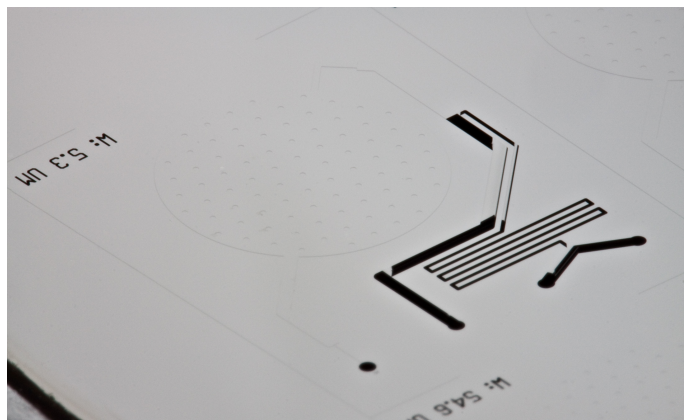


**Figure 2.2** – The reactor directly from the clean room. On the unbonded sample, only the deep etched parts of the reactor is clearly visible, but also the reactor area and the capillary can be seen if one looks carefully. Photo by Thomas Pedersen.

In the  $\mu$ -reactors, we often deposit samples that we do not want to heat before measurements. Especially not in air. For this reason, we often use a cold-bonding method which was developed here at CINF[10]. When cold bonding the reactor is carefully positioned on top of a cold-finger which will keep the reactor area at temperatures close to room temperature thus protecting the catalyst while the rest of the sample is heated.

## 2.2 General measurement principle

In order to perform actual measurements, one needs more than just a bonded silicon reactor. It is also necessary to have some kind of gas-handling, a way of heating the reactor, as well as a detection mechanism for the reactants and products. As much of the rest of this thesis will discuss, this can be implemented in many specific ways, but the overall concept is very general and should be introduced before moving on to the details.

The reacting gases are supplied to the two inlets by flow controllers capable of controlling the gas flow in various ranges, typically on the order 0–10 mL/min. The flow controllers have an analog interface which allows the flow to be set by applying a 0–5 V voltage and the measured flow is returned also in the form of a 0–5 V signal. This makes it very easy to computer interface the flow controllers with standard DAQ-cards.

The capillary flow is fed into a quadropole mass-spectrometer (QMS) for analysis. The QMS is mounted in a fully traditional, however, rather small UHV chamber pumped by a turbo pump. It is of great importance to keep the base pressure as good as possible in the chamber since this background is superimposed on all measurements and it will often be the effective sensitivity limit of the measurements. If the chamber is properly baked and otherwise treated according to good UHV practice a base pressure of  $\sim 2 \times 10^{-10}$  mbar can be reached. However, since many of the activities on the  $\mu$ -reactors involves dosing more water and air residues than would optimally be desired in a UHV system, the typical day-to-day pressure is on the order of  $1 \times 10^{-9}$  mbar.

All surplus of gas from the inlets is passed directly through to the outlet via a pressure controller allowing control of reactor pressure. One could wonder why we need this main

outlet flow at all, since this gas flow is not used and does not contribute to the measurement. The reason is that the capillary flow is simply too small to handle in the external gas-system. We need reasonably high flows both because there is a lower limit towards how small flows mass-flow controllers can control reliably and because the tubing contains a non-vanishing volume, especially since we are using 1/4" tubes in the entire system to ensure that we can withhold high cleanliness in the system. Also the pressure controller needs some amount of flow to be able to keep a constant pressure in the system. That being said, it is possible to run the system with rather low flows if this is wanted, eg. in the case of expensive isotopically labeled gasses. Continuous operation with gas-flows lower than 0.5 mL/min pr. gas species is certainly possible.

During experiments the chip is mounted in a metal block which is connected to the gas-handling system. The sealing between the chip and the metal block is done by O-rings. The typical O-ring material of choice is Kalrez due to its ability to be heated to very high temperatures. For low temperature operation, also Viton can be considered, since this material is both cheaper and can be cooled to lower temperatures before it becomes brittle. Unfortunately rubber O-rings are not leak-tight, especially not when they are heated, which means that we have an inflow of air across all four O-rings. This is very unfortunate in situations where oxygen is not wanted, e.g. methanol synthesis or other processes with products that are easily oxidized. Also, the air inflow through the O-ring sealing the capillary outlet complicates interpretation of data a lot since it will give a background of air on top of the signal from the product gas. To eliminate both problems the O-rings are continuously flushed by a flow of Argon. If the flow is chosen sufficiently high, it will out-compete the air-inflow and result in a more or less pure Argon inflow, which is much more acceptable, both regarding the chemistry and regarding data interpretation. Another solution to the problem is to evacuate the entire surroundings of the metal block, this option is discussed later in this chapter.

The reactor has a fairly short residence time which can easily be estimated from the known values of the volume and the gas flow through the capillary. Since one mole of ideal gas has a volume of 24 L at room temperature, we can easily find the number of molecules in the reactor:

$$N_{reactor} = \frac{240 \times 10^{-9} \text{ L}}{24 \text{ L}} N_A = 10^{-8} \cdot N_A = 6 \times 10^{15} \text{ molecules}$$

The capillary flow has been measured to  $\sim 6 \times 10^{14} \text{ s}^{-1}$  [9] thus giving a residence time of

$$T_{res} = \frac{6 \times 10^{15}}{6 \times 10^{14} \text{ s}^{-1}} = 10 \text{ s}$$

### 2.3 Brief historical tour

Since I was not the first Ph.D. student on the  $\mu$ -reactor platform, I did not build the original experimental setup. The original setup is extensively described in the theses of Peter Vesborg [8] and Jakob Olsen [9]. This chapter will be a short summary of the state of the setup as of when I came (which happens to be the same time as Peter and Jakob left it). The  $\mu$ -reactor concept has a much longer history but this is really not a concern of this thesis. A schematic of the setup as of the day I arrived is seen on Figure 2.3. The setup had several problems which it was necessary to address before the setup was ready for measurements beyond proof-of-concept measurements. First of all, it is evident from Figure 2.3 that all the gas-handling is pumped directly by a roughing pump. This means that the the system will be

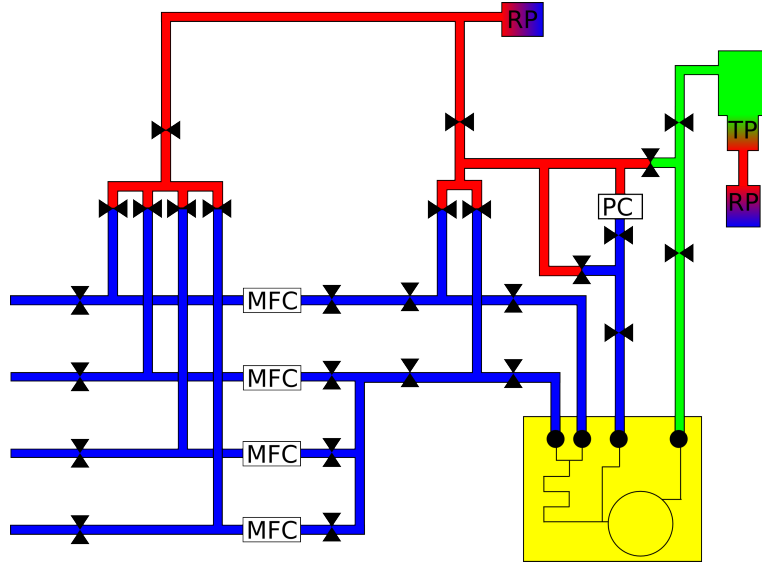


**Figure 2.3** – The  $\mu$ -reactor setup as of the day I arrived. Blue tubes contain the incoming gas flow and is typically operated at 1-2 bars. Red tubes are pumped with a roughing pump and are typically operated at  $\sim 10^{-3}$  mbar. Green tubes are pumped by a turbo pump and are typically operated at pressures around or below  $\sim 10^{-6}$  mbar during experiments. The drawing of the reactor chip itself is only schematic and does not reflect the actual layout.

constantly contaminated by oil residues from the pump which is the primary constituent in the residual pressure from a roughing pump. This also means that it is impossible to do a proper pump-down of the capillary before opening to the mass-spectrometer and thus the background pressure in the main chamber will typically be rather high, primarily because of water, residual air and perhaps oil from the roughing pump depending on how far the capillary was pumped down.

Another problem is the valves in front of the flow-controllers. It is well known that flow-controllers are not very internally leak-tight even when the flow is set to zero. This means that if one wants to eliminate the background of the gasses available on the setup, one needs to close the valve in front of it. However with a manual valve, this makes it impossible to eliminate backgrounds from gasses that are actually used during the experiment. Finally many gas-lines were implemented with gasket-less Swagelok type connections, which are not UHV-compatible. Along with rebuilding the system it was obvious to also change all gas handling to copper sealed VCR connections.

For this reason, my first project on the setup was to update the setup to prepare it to perform actual measurements since the proof-of-concept measurements were more or less all performed at this time. The first iteration on this update is seen in Figure 2.4 and Figure 2.5. The most important change is the fact that no part of the setup is now pumped by roughing pumps. All tubing that needs to be regularly evacuated are now connected to a buffer volume which is in turn pumped by a turbo-pump through a 1/4" tube. The role of the buffer volume is to provide a large volume to absorb bursts of gas before they reach the turbo pump. This is especially important when you place a turbo pump at the vacuum side of a pressure controller since these devices will typically undershoot quite a bit when they go down in pressure. If the turbo pump is attached directly to the pressure controller

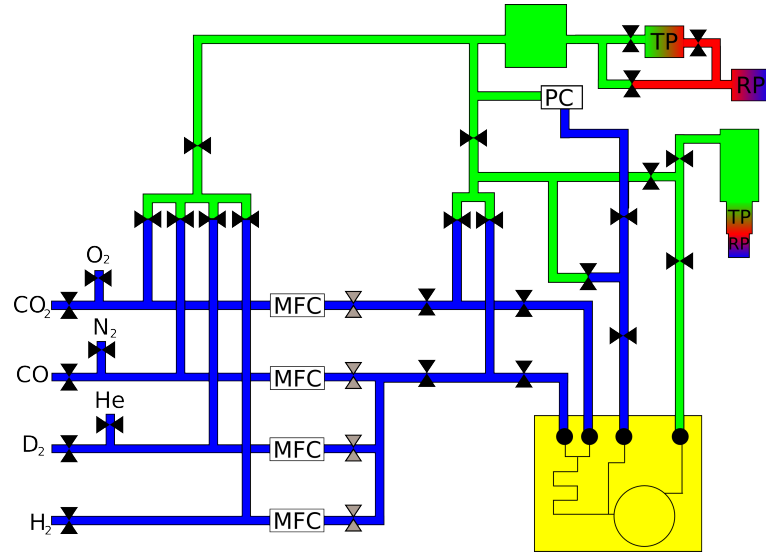


**Figure 2.4** – The  $\mu$ -reactor setup after the first update. Grey valves are pneumatically activated. Besides these valves, the main new feature is the introduction of a turbo pump to ensure oil-free vacuum in the entire gas handling system. Often we mount two different gasses to each MFC, of course only one can be used at any time, but in this way it is fairly easy to switch between the various gasses.

these undershoots will be extremely hard on the turbo, the buffer volume's purpose in life is to smoothen out these burst. The system works beautifully and makes it possible to pump down the entire system to approximately  $10^{-5}$  mbar with absolutely no oil in the residual gas. Even though this is of course not real UHV it is still a background pressure approximately 8 orders of magnitude below the operating pressure of the setup. A small drawback on the new design is that all of the main gas flow must go through the turbo-pump thus somewhat limiting the total acceptable flow. However, experimentation has shown that we can go as high as  $\sim 10$  mL/min without drawing excessive currents in the turbo. This flow is high enough for most purposes and certainly it is high enough that pressure measurement of the reactor becomes unreliable due to flow resistance in the main outlet. For this reason we typically try to stay well below 10 mL/min anyway.

The system was also updated with four pneumatically operated valves in front of the flow-controllers. These valves are programmed to close every time the flow for the corresponding controller is set to zero. In this way we can decrease the background from unused gasses significantly. Besides the work on the mechanical parts of the setup, we also completely changed the way heating and temperature measurement was performed, however, due to the complexity of this subject it has been moved to a separate chapter (chapter 3).

## 2.4 Next Generation

At some point we realized that with the amount of samples we wanted to measure at the same time as we wanted to keep modifying and improving the setup, we simply did not have enough instrument time to do it all. For this reason we decided to build another setup using

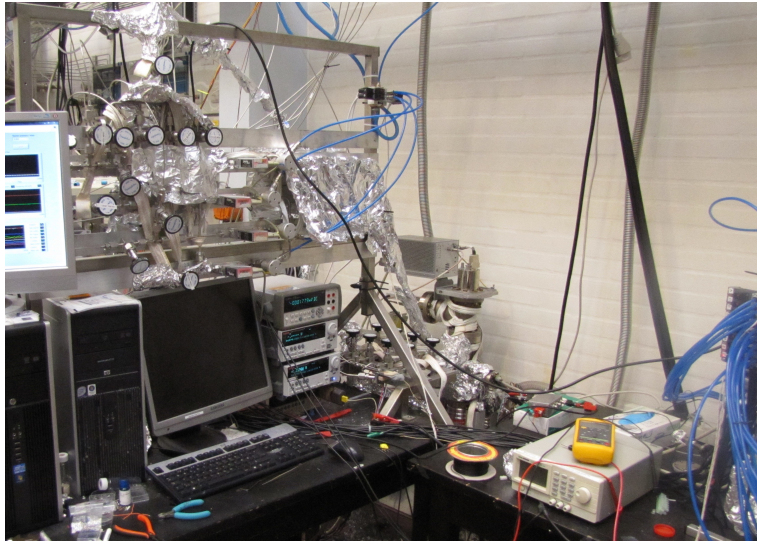
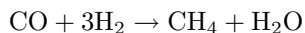


**Figure 2.5** – The updated version of the  $\mu$ -reactor setup. Photo: Mathias Kjærgaard Christensen.

the experience gained from the old setup. The two by far most important things to improve compared to old setup was first of all to eliminate the need for a permanent argon flow and to mount pneumatically controlled valves on most of the setup to ensure that the system can be remotely operated.

#### 2.4.1 The Tale of the Leaking O-rings

At first glance, the solution to the leaking O-rings of flushing with argon might seem as a good solution, but it does have several drawbacks. For one thing it is hard to tell how well it is actually working. Of course one can measure with the mass-spectrometer if huge amounts of air leaks in along with the argon, however, smaller amounts might be difficult to detect even though it might still be enough to be a problem. If one for instance is running a methanation reaction,



it would be highly problematic if even small amounts of oxygen reached the reactor. Secondly, one should not underestimate the costs of having a reactor flushed continuously with argon. Originally when the setup was first designed, it was constantly in development and was often performing pure test measurements. However, today, it is not uncommon for the setup to run continuously for several weeks. The argon consumption in such periods is between one and two bottles (50 L, 200 bar) pr. week which turns out to be a non-negligible cost. Thirdly, it can sometimes happen that we simply run out of argon during a long experiment, especially over the weekend. When starting an experiment one needs to judge whether the remaining argon supply will last for the rest of the experiment and unfortunately it can sometimes happen that this estimate fails and the argon run out which will often render the results useless. This also means that it is basically impossible to keep a sample in the setup over a holiday and run a few experiments from home, since the argon supply will not last more than approximately 4–5 days.

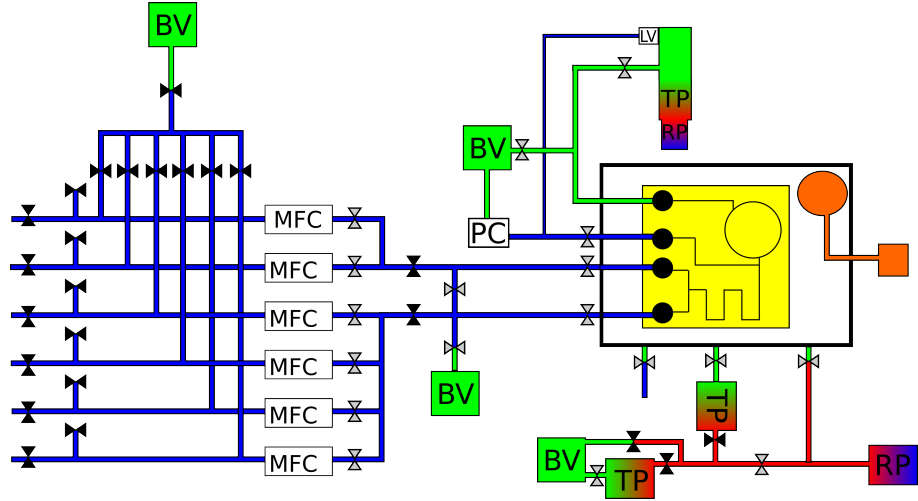


**Figure 2.6** – The so-called 'Next Generation' setup. To simplify the drawing, the buffer volume has been drawn several times. The black square represents the containment volume. The valve pointing into nothing is used for ventilating the containment volume. The orange structure connected via a feed-through into the containment volume is the cooling braid. The box named 'LV' is the piezo actuated leak valve.

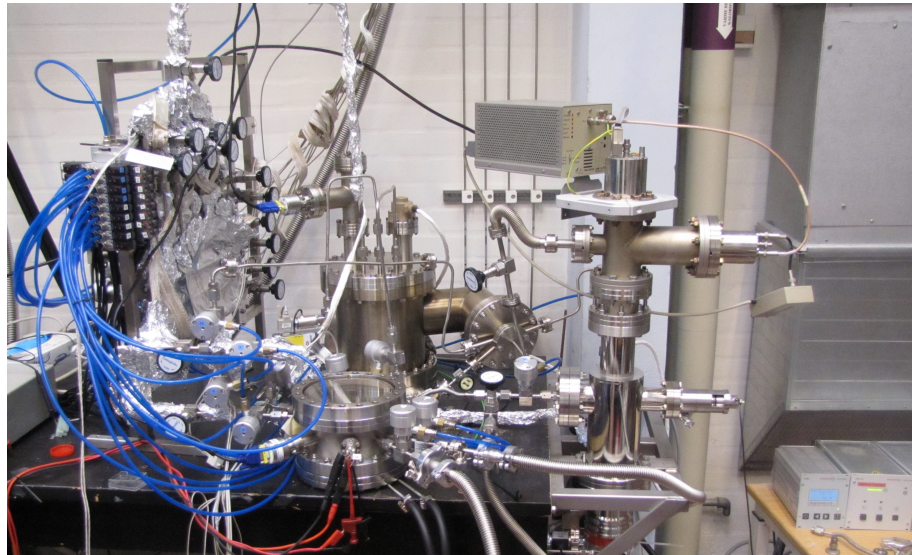


**Figure 2.7** – The Next Generation Setup. Photo: Mathias Kjærgaard Christensen.

For all these reasons it was clear that the NG setup should have another solution to the problem of the leaking O-rings. The best solution would of course be to have a leak-tight sealing between the reactor and the metal tubing, but this strategy has been tried before[9] and failed. Instead we chose the brute-force solution of simply evacuating the entire surroundings of the  $\mu$ -reactor. The workshop manufactured a small chamber (known in daily language as the 'containment volume'), which is basically a short tube closed by two 8" flanges. The tube is equipped with several mini-cf flanges for mounting electrical connections and a thermocouple. Pressure is measured using a MKS 925 MicroPirani[11], which will measure from  $10^{-5}$  mbar to atmosphere and contains a serial communication interface. The gas handling is implemented as 1/4" tubing welded to the flange and connected via VCR fittings to bellows on the inside which is again welded to the metal interface block. For the top 8" flange (that is, the 'lid' of the construction) we currently have two choices. Either we can mount a full-sized window providing optical contact to the sample, or a traditional blind flange with a hole drilled by our wonderful workshop at the position exactly above the sample. Here we can mount a 2" germanium wafer. Since germanium is transparent in the infrared part of the light-spectrum this window allows us to take thermographic images of the sample under vacuum.

#### 2.4.2 Pneumatic valves

Replacing the manual valves with pneumatically controlled valves was a high priority for several reasons. First of all, it takes time to pump down the capillary sufficiently to be able to open the valve to the main chamber. Often this means that the sample is ready to start measuring sometime outside normal working hours. With a pneumatic valve between the capillary and the main chamber it becomes possible to start the measurements from the comfort of the operators own home. With the old setup one needs to wait until the next morning.

Another great advantage of pneumatic valves is that it opens up for much better pumping of the gas system. On the old setup, the only way to evacuate the gas-system during an experiment is to set the pressure controller to 0 and pump out through the sample. Since this is an extremely bad pumping route it takes very long time to pump down in this way. In the new design, we have attached pneumatic valves that will allow direct access through 1/4" tubes between the gas system and the buffer volume. This allows for much better and faster pumping.

Experimentally it takes a bit of work to operate pneumatic valves. The valves we have chosen are from Swagelok because we know them to be leak-tight and because they have the same dimensions as the manual valves we have typically been using. These valves are normally-closed by a spring load and will open by applying pressurized air at approximately 3 bars. This means we need a way of actuating the pressurized air which is most easily done by solenoidal valves since they can be directly electrically controlled. However, to have sufficiently dynamic range on the solenoid to be able to both open and close sufficiently well a rather high voltage of 24 V is needed. Since in the end we want to control this programmatically, we need a multichannel computer controlled 24 V supply which is not cheaply available. For this reason we convinced our electronic workshop to build a truly wonderful 20 channel 5 V to 24 V converter. This allows us to control the entire thing using standard TTL 5 V signals which is very easily available. In practice we use National Instrument DAQ-cards but many other options are available for this kind of task. In the end the procedure of opening a single valve may sound rather complicated; Computer

→5 V→24 V→solenoid valve→pressurized air→valve opening. However in practice it works like a charm and problems with the intermediate steps are basically limited to the initial wiring which does take quite a lot of work.

### **2.4.3 Pumps**

The new setup consists of no less than three separate vacuum chambers and including the old setup we end up at five chambers. Each of these chambers are equipped with separate turbo pumps bringing us to a total of five turbo pumps. Each turbo of course needs a corresponding roughing pump, and we also need a roughing pump to pump down the containment volume every time a sample is changed, ending up at a total of six roughing pumps to cover all the needs. But adding six roughing pumps to the system is not really a realistic option, partly because roughing pumps are expensive and partly because of very low-tech problems regarding having so many roughing pumps in the lab. For this reason we have designed the system in a way, where 'only' three roughing pumps are needed to run both  $\mu$ -reactor systems. One pump is shared between the main chambers of the old and the NG setup. Since the main chambers are UHV chambers, the gas-load is low and we have no problems with pumping capacity. Back flow of gas between the two chambers through the shared roughing line can be a small problem, but modern turbo pumps have very high compression and the problem is basically limited to hydrogen, which actually can back flow through a turbo. However, this has not turned out to give real-world problems since we do not use hydrogen very often and using it on both chambers at the same time is a very unlikely event. The second roughing pump is dedicated to the buffer volume turbo of the old setup and is simply mounted directly on the turbo with suitable tee-pieces and valves to allow pumping down the buffer volume from atmosphere if necessary. This pump also backs the Time-Of-Flight instrument (introduced in chapter 8) when it is attached to the  $\mu$ -reactor system. The third roughing pump backs the buffer turbo of the NG chamber as well as the turbo pump on the containment volume. However, this is also the pump that does the initial pumping of the containment volume every time it is vented to change the sample. To achieve this we need to close the valves to the turbos while pumping down since the roughing pressure will temporarily be too high for the turbos. Since we change samples quite often we soon realized that we need an automatic procedure for this opening and closing of the valves behind the two turbos. This was solved by an solenoidal actuated bellow valve from Lesker. This valve is actuated by a 24 V signal and ensures that the turbos are protected when the roughing line is used to pump down the containment volume.

### **2.4.4 Miscellaneous improvements**

Besides the obvious improvements we wanted for the NG setup we also added a number extra features which are not quite as much need-to-have but are nonetheless nice and useful additions to the setup. First of all we added a thick copper feed-through connected to a copper braid ending in a thin copper plate that can be mechanically positioned on top of the sample. By cooling the feed-through from the outside of the containment we are now able to cool the sample. The lowest achievable temperature has not been tested yet. So far we have only checked that the cooling actually works, which indeed it does. Most likely the limit will be set by the O-rings which will not go much lower than -60°C[12] depending on the choice of O-ring material.

Another useful modification is the addition of a sniffer line from the reactor outlet via a

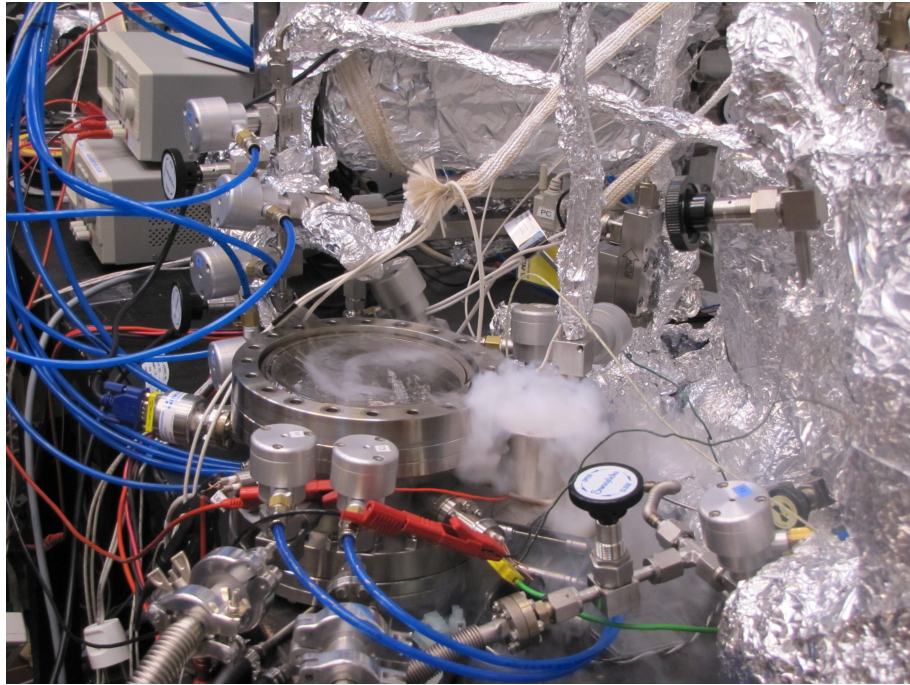


**Figure 2.8** – Testing of the cooling feed-through. Finally UHV science gets some visual appeal!  
Photo: Mathias Kjærgaard Christensen.

computer controlled piezo-actuated leak valve into the main chamber. The line is implemented as a 1/8" gas-line that connects the reactor outlet to the main chamber via the leak valve. It is very important that the line is as short as possible and with a small diameter since this line contains the gas mixture of the experiment at high pressures, and since this mixture might be explosive the total volume should be minimized. The advantage of the line is that it opens up the option of doing in-situ blank experiments without removing the sample. Since mass spectrometers can give results that can be slightly difficult to interpret, it is often necessary to perform blank experiments to judge the mass-spec signal from just the reactants with no catalyst available. With the sniffer line it is possible to perform this test without changing the sample.

#### 2.4.5 Safety mechanisms

Because all our valves are pneumatically activated, we have the option of implementing a number of safety mechanisms which will protect the equipment if something goes wrong. These mechanisms fall in two distinct categories. One is the software controlled checks which will programmatically intervene the experiment if some parameter falls outside of the allowed range. The other type is the purely electrical mechanisms which will close relevant valves based purely on hardware triggers.

The programmatically controlled safety features includes that the software will continuously monitor the pressure in the containment volume. If the pressure becomes too high, typically because of bonding errors in the sample, the software will prevent heating of the sample.

This is done to prevent gas-convection to transport heat to the 8" glass lid which will not survive too large temperature gradients.

The purely electrical safety features are of course the most important, since they will react much faster and much more reliable than the software will be able to, especially because the need of activating a safety feature might easily be due to bugs in the software. The system is based on set-points on the gauge controller. The controller, an Agilent XGS600[13], contains 8 open-collector outputs which will turn on or off based on pre-programmed pressure ranges. The electronic workshop has build an 8-channel open-collector→24 V box which will open or close the pneumatic valves based on the set-points. This means that the main chamber valve will close immediately if the pressure in the main chamber exceeds a pre-programmed pressure. Typically the safety limit is set to  $10^{-6}$  mbar. For the containment and buffer volume, the check is done on the roughing lines since the pirani gauges mounted directly on the chambers are not read out by the XGS controller. The typical safety limit for these chambers is 1 mbar in the roughing line, if the pressure exceeds this value, it is assumed we have a leak and the valves above the turbos will be closed.

## 2.5 Experiment automation

The  $\mu$ -reactor platform often performs experiments that are both long and often involves quite a lot of process steps. For applications like this, it is unfeasible to run the experiments manually. For this reason, we have developed software that reads a so-called flow file and performs the experiment according to this file. The concept of a flow file is so powerful that it is a very rare event that the setups are run in manual mode. This more or less only happens when teaching students on the setup. The advantages of the automated procedure even for rather simple measurements is that we get a very high degree of reproducibility between samples. If two samples are run by the same flow file we are sure they receive a treatment as identical as we possibly can. A typical example of a very simple flow file could look like this:

```
#Initially all flows should be zero
Time; 0
Flow1;0
Flow2;0
Flow3;0
Flow4;0
Temp; 0
Press;0
Speed;1
Time; 30
#Clean with lightoff
Flow1;5
Flow3;1
Press;1
Time; 10
include;light_off_ramp
Time; 10
Temp; 0
Time; 5
Flow1;0
```

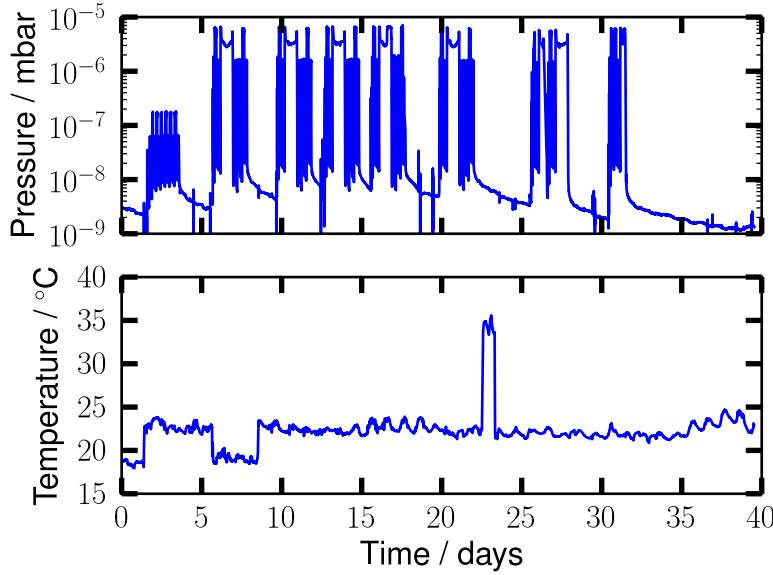


**Figure 2.9** – A simple example of the type of data stored in the CINF database, in this case some of the continuously logged status data from April and May 2012. In the top panel the main chamber pressure is plotted and in the lower panel the temperature of the main chamber turbo pump. The high temperature spike is from a scheduled shutdown of the central cooling water, it can be seen from the pressure graph, that no measurements was performed in this period of time.

```
Flow3;0
include;pumpdown
```

The file is parsed from the top towards the bottom. All actions stated between individual 'time' commands are executed at the same time. At each 'time' command the flow is kept constant at the current configuration for the stated amount of minutes. The code-example above will thus start out by evacuating the sample for 30 minutes before starting a flow of 5 mL/min O<sub>2</sub> (flow 1) and 1 mL/min of CO (flow 3) with the pressure controller set to 1 bar. After 10 minutes of gas-flow the temperature is increased in a linear ramp (the include statement will simply import another file of the same syntax, this one with consecutive time and temperature steps to create a temperature ramp). 10 minutes after the ramp has finished the temperature is set to zero (basically turning off the control loop and letting the sample cool to room temperature). Five minutes later, the flows are stopped and the reactor is pumped down by another include file. It is easy to see, that arbitrarily complex measurements can be written like this and the possibility to include standard files eases the task of setting up the measurements enormously.

## 2.6 Data storage

Along with an automated experimental setup should necessarily go a comprehensive data logging system to make it easy to real-time monitor what the setup is actually doing. Since no such logging system was present at CINF, we have made one to solve our specific needs and over time this has proven to be immensely useful. The core of the system is a centrally managed MySQL database running on a dedicated server (popularly known as 'servcinf'). All measurements performed on the  $\mu$ -reactor setup (and gradually many other setups) are saved directly to the database with no temporary storage at the local computer. This has many advantages, for example it is possible to real-time monitor the measurements through a web-browser from anywhere in the world. It also ensures that all data are secured even in the event that the computer crashes (an all too frequent event when using LabView for data acquisition....) and data are continuously backed up by the central IT-department. Also, the central server acts as a common entrance point when searching for old data, either one's own data or data from other CINF setups that could have results relevant for the current project. The data can be easily accessed either from the web-interface or directly from the database. Almost all figures in this thesis is thus made by very simple python-scripts which extracts data from the database and plots them in a consistent way. Besides storage of the individual measurements, the system also continuously logs health information of the chamber, such as chamber pressure, turbo pump temperatures, sample temperature, roughing pump pressures, etc. A small excerpt of this data is shown in Figure 2.9. In this way it is easy to catch a developing problem from eg. a roughing pump needing service or to pin-point when a UHV chamber has developed a leak.

# Chapter 3

## Temperature - heating and measuring temperature

Measuring temperature accurately is always a difficult task. For the  $\mu$ -reactor, the problem is especially tricky because the 2D-like structure and small thermal mass of the system means it is difficult to establish contact to a thermocouple. This is opposite to classical single crystal science where the thermocouple can simply be mounted inside the sample. To complicate things even further it is also highly difficult to achieve a constant temperature across the reactor. First of all the contact between the highly heat-conducting silicon wafer and the comparatively cold metal interface block means that a constant heat transfer occurs along the chip whenever the chip is heated. This of course leads to temperature gradients along the chip. Also convention losses to the surroundings will contribute with non-homogeneous heat-loss. Thus, even given an ideal heating mechanism that simply delivers a constant power pr. area to the entire chip, the result would be a non uniform temperature that would be hottest at the center of chip, colder along the edge and coldest at the contact between the interface block and the chip. To complicate things even further, no such 'ideal' heating device exists, in fact it is not easy to deliver power in a uniform way.

### 3.1 Temperature control

No matter how heat is transferred to the sample, one will typically want to bring the sample to a given temperature, not to source a given amount of watts, which is what is the directly controllable parameter. Some kind of temperature control is thus needed to ensure that a suitable power is applied to reach the wanted temperature. Many both hardware and software solutions exists for such a control mechanism, in our case we have chosen to run the control loop in home-made software. The current implementation is made in LabView which for better and (mostly) for worse is the default language of choice at DTU. The home-made implementation ensures that we know what is going on behind the scenes of the software, and that we have the flexibility to change all part of the setup ourselves.

In catalysis, it is of very high importance to be able to reach and stay at a given constant temperature for extended amounts of time, even if the conditions of the surroundings change over time, which will typically happen for measurements running as long as is the case in the  $\mu$ -reactors. The typical choice, which is also used by us, in such situations is a PID-control.

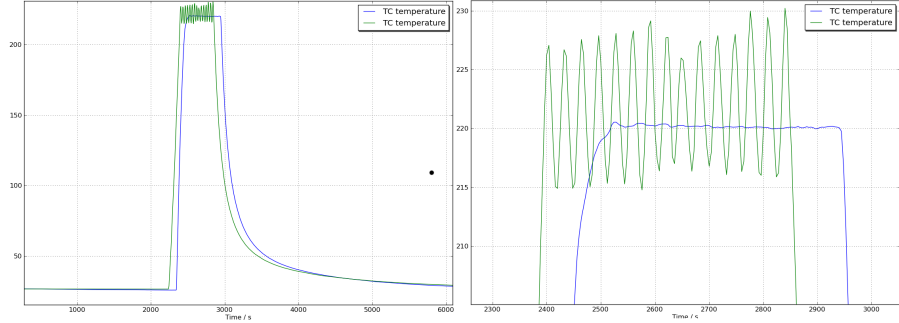


**Figure 3.1** – Illustration of the improvements achievable by optimizing the PID algorithm. Green curve is the old implementation and the blue curve is the new implementation. The two tests are both performed with the same heater, only the control software is different.

For every time step,  $\Delta t$ , the wanted output is calculated from the temperature error function,  $E = T_{setpoint} - T_{measured}$ . Given knowledge of  $E(t)$  at all times, the wanted output can be calculated as

$$O(t) = P + I + D = k_p E + k_i \int_0^t E + k_d \frac{dE}{dt} \quad (3.1)$$

with  $k_p$ ,  $k_i$  and  $k_d$  denoted proportionality, integral and differential terms, respectively.

Implementing a PID-control is a very easy task. Just implement equation 3.1 and experiment a bit to get decent values for the constants. However, implementing a good PID is slightly more complicated, since often in a specific system, one can find optimizations that are not captured by the general formalism. In our case we have a particularly easy system to regulate, mostly due to the good thermal time constant in the system. This means that one can significantly out-perform the direct implementation of equation 3.1. In our case we have a direct comparison because the original temperature control was indeed simply a direct implementation, which was originally made by a bachelors student [14] and was used in that form for a long period of time. When we started to push the  $\mu$ -reactors from prototypes to real measurement devices, a new and better algorithm was needed. A simple but very effective improvement is made by realizing that the purpose of the differential term is to counteract unwanted behavior, such as overshoot. In many systems better ways exists to prevent this and at the same time, the term will often lead the overall PID to oscillate around the set-point. A new algorithm was implemented with  $D = 0$  and the added heuristics that if  $O(t) > O_{max}$  then  $I(t + \Delta t) = I(t)$  no matter the value of  $E$ . This has the effect that  $I$  will not tend to grow to large values when the temperature is still far from the set point. The optimal value of  $O_{max}$  must be found experimentally just as  $k_p$  and  $k_i$ .

The difference between these two strategies is illustrated in Figure 3.1 where the response from both implementations to a step-function in temperature is plotted.

## 3.2 Heating mechanisms

In the first iteration of the setup, heating was done via a small ceramic block with a hot filament inside that was spring mounted to the backside of the chip. This has several advantages in the way of mechanical handling and very easy interfacing of the heater, apply a suitable DC-voltage and you are ready to heat. However, the method also has many

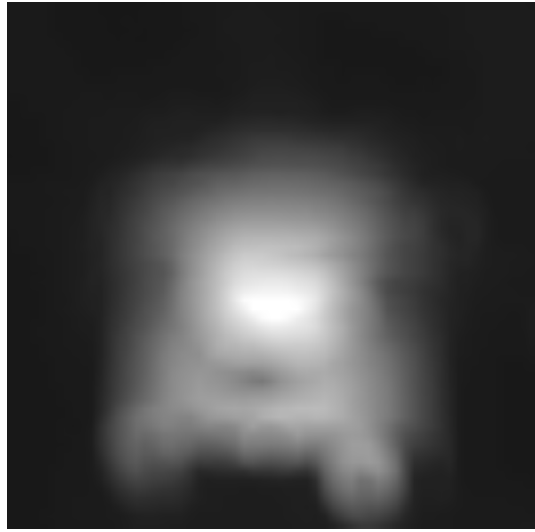


**Figure 3.2** – Thermographic image of the sample heated by the original heating element. Notice the very pronounced spot-heating at the contact point of the heater.

drawbacks. Most importantly, it turned out that we had severe problems measuring the temperature, but also point-heating was a great problem. Since it is very difficult to mount the heater completely parallel to the sample, inevitably a single small point of the heating element will be in contact with the sample resulting in point heating. A thermographic image shows this problem very clearly as seen in Figure 3.2. Moreover because of the mechanical spring mount, this point heating was not consistent. This meant that two nominally identical heating runs could easily result in very different temperature profiles across the chip. As if these properties were not bad enough it is also not trivial to measure the temperature of the sample. Mounting a thermocouple from the backside is not possible due to the heating element, meaning that temperature has to be measured on the lid. In practice this was done by manually placing a thermocouple on top the sample. The combination of non-consistent point heating and thermocouple position obviously resulted in very large uncertainties in the temperature.

To fix this problem we developed a new solution in close cooperation with the clean room wizards. The idea this time was to integrate the heater directly onto the chip (a concept that also fit very nicely with the overall  $\mu$ -reactor idea) and then use the heater itself to also measure the temperature. After some discussions we ended up with the structure seen in Figure 3.3. The structure is implemented in the cleanroom by e-beam evaporating 100 nm of Pt on top of an adhesion layer of 3 nm of Ti through a shadow-mask. This deposition method guarantees that absolutely no Pt finds its way to the front-side of the reactor, which is very important since as it is demonstrated in chapter 6, even minute amounts of Pt can show reactivity to various processes. The integrated heater will immediately solve all problems regarding reproducibility of the heating. All samples are heated in exactly the same way since the clean room process has a very high degree of accuracy. Originally we also expected that this design would mostly eliminate the problems of inhomogeneous temperature across the reactor area, but as we shall see later in this chapter, the temperature distribution is still far from perfect.

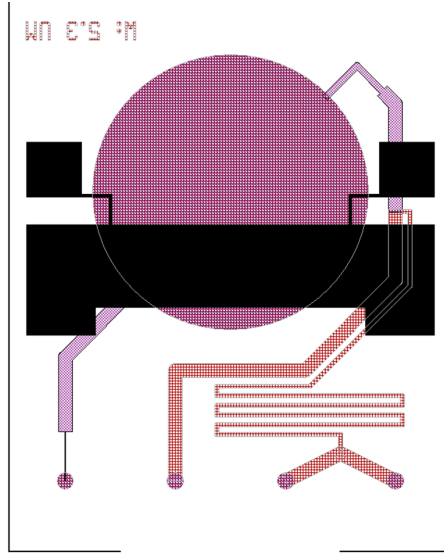


**Figure 3.3** – The integrated Pt heating structure. This is the heating mechanism that has been used for almost all work in this thesis.

With the integrated heater, it has turned out that we can fairly easily reach temperature of approximately  $350^{\circ}\text{C}$  and with a bit of luck up to slightly above  $400^{\circ}\text{C}$ . At these temperatures the limiting factor is mostly the power supply for the heating as well as the rather high current densities in the heater, which will eventually degrade the continuous Pt film.

### 3.3 Operating the RTD-heater

As seen in Figure 3.3 the combined heater and RTD is implemented as a Pt strip with four contacts. Temperature is thus measured as the four point resistance of the Pt strip calibrated to a thermocouple at room temperature. The thermocouple stays on top of the sample for the entire measurement; even though poor thermal contact will prevent it from recording the correct temperature, the apparent temperature will still be a consistent function of the actual temperature and thus the thermocouple can be used as a sanity check of the RTD measurement. The challenge now is to heat the sample through the same Pt strip while still being able to measure the resistance reliably. To do this one essentially needs a Source-Measure instrument to ensure 100% perfect synchronization between the measurements of the voltage and current which are both changing continuously, partly because of the non-constant temperature and partly because the control-loop constantly updates the needed power to stay at the set-point temperature. In our case we use a Keithley 2635A SMU[15] which will source up to  $1.5\text{ A}$  at  $20\text{ V}$ . This is sufficient to reach temperatures slightly above  $400^{\circ}\text{C}$ . The sample is contacted through four Pogo-pins mounted in a ceramic block, the block is mounted with four screws on a metal structure that is again screw-mounted on the metal interface block. The mounting screws of the block can be individually adjusted to ensure contact of all four pins. To increase the maximum achievable temperature and to measure a slightly more realistic temperature from the thermocouple, two layers of insulation is placed on top of the sample.

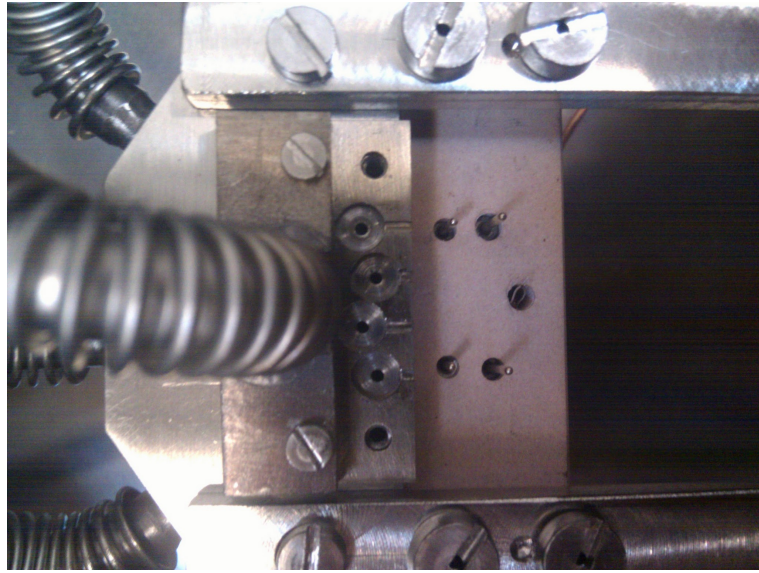


**Figure 3.4** – The ceramic block holding the Pogo pins along with the screw-connections to the metal interface block. The four holes are the holes for the inlets and outlets of the  $\mu$ -reactor. The gas line pointing out from the metal block is the feed line for the Argon flow.

### 3.4 Temperature profiles

Originally we expected that the integrated heater would magically solve all our temperature distribution problems. The idea was that the very high heat conductance of silicon would ensure that the power delivered to the strip was evenly distributed to the sample. However in hindsight it is easy to see that this was a hopelessly naive expectation. In reality we have a quite large heat gradient across the sample. Fortunately, since we are measuring the temperature at exactly the same place as we are heating, we are not under-estimating the temperature. More likely are we measuring the absolute highest temperature with all other parts of the reactor being colder than the measured temperature and thus we tend to under-estimate the performance of a given catalyst under test because only a fraction of the sample is at the expected temperature.

The way we estimate the temperature distribution is by imaging the sample with a thermographic camera. The camera is excellent at providing images of the temperature distribution but not equally well suited for measuring the absolute temperature, since this calibration is dependent on the emissivity of the sample which is again dependent on several things, including the temperature of the sample. For this reason we typically bring the sample to a fixed temperature as measured by the RTD and then either adjust the emissivity value of the camera to show the correct temperature, or just scale the result. For temperatures below  $300^{\circ}\text{C}$  an emissivity value of  $\sim 0.92$  gives quite good results in the entire temperature range. For temperatures higher than this, one typically needs to lower the emissivity value to match the RTD-temperature. The result of this analysis was as already mentioned rather disappointing. In reality we have a significant heat gradient of almost  $30^{\circ}\text{C}$  along the reactor. This is of course way to much to be acceptable in the field of catalysis where most processes are exponential in temperature and since the current heater design also have other practical

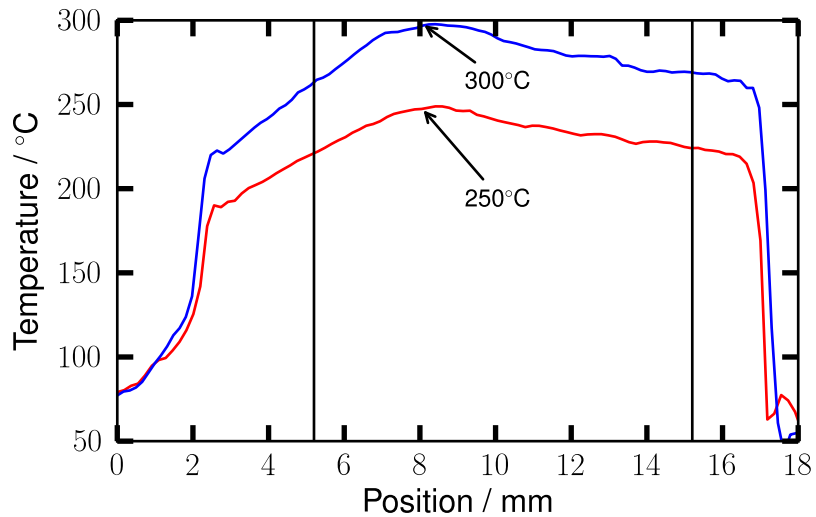


**Figure 3.5** – The temperature profile of the sample at two different temperatures. The temperature measurement has been scaled to match the RTD temperature. Vertical lines indicate the reactor area.

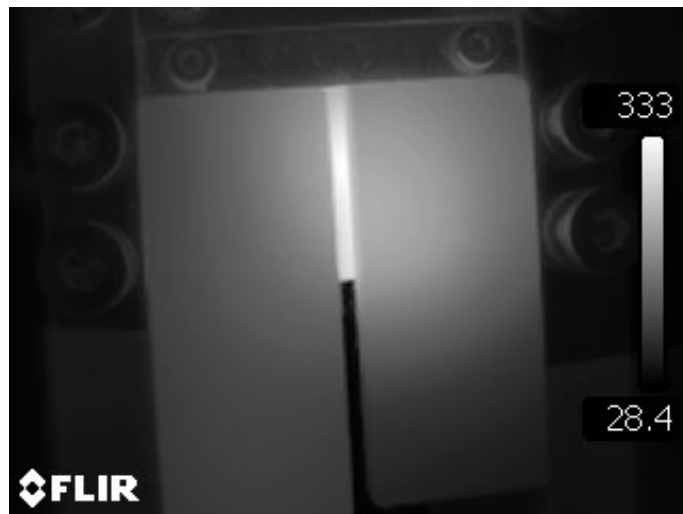


**Figure 3.6** – Thermographic image of the insulated sample at 300°C. The corresponding temperature profile is drawn in Figure 3.5.

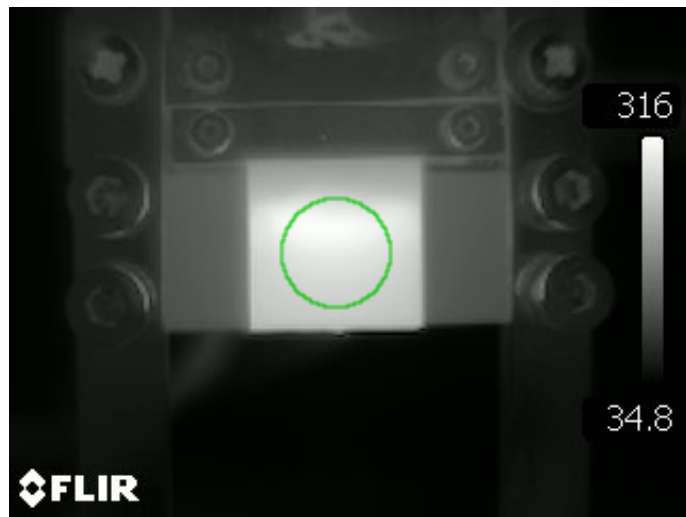


**Figure 3.7** – Thermographic image of the same sample as Figure 3.6, also at 300°C, this time without insulation to be able to see the entire reactor.

problems, we have started to work on a better solution for heating the sample.

### 3.5 New heater

One problem with the current design is that the SMU is a very expensive way of performing an operation as simple as sourcing current for a heating element. This also means that it is hard for us to increase the temperature further since Source-Measure instruments that will source more power is even more expensive. At the same time we have the problem with non-uniform heating which also hints that we might need a new design for the heater. The reason we originally combined all functions into a single strip was that we were afraid that we would get problems contacting the samples if we had too many contacts on the rather small area. However the experience gained from operating the heater is that contacting is really not too much of a problem. For this reason we have recently designed a new heating system based on the experience gained from the old heater. This time we have three separate heating element as well as a four-point RTD directly under the reactor volume. This means that we can now measure the RTD temperature using standard (and cheap) DMMs and the heating can be performed with real power supplies and thus we no longer have problems sourcing enough power into the sample. We are now only limited by the temperature where the pyrex lid will become soft, which is expected to be in the range 650–700°C. Besides the changes in the heater, we also increased the length of the sample from 20.1 mm to 27 mm to increase the distance between the sample and the heat sink in the mounting block, also in an attempt to minimize the temperature gradient across the reactor.

Of course with three separate heaters, it becomes quite a challenge to find the perfect power distribution between the individual heaters. Experimentation with this is not easy, since every time a new layout is to be tested, it is necessary to make a new shadow mask for depositing this particular heater, a process that takes quite an amount of both time and money in the clean room. For this reason we kept the experimentation to a minimum and

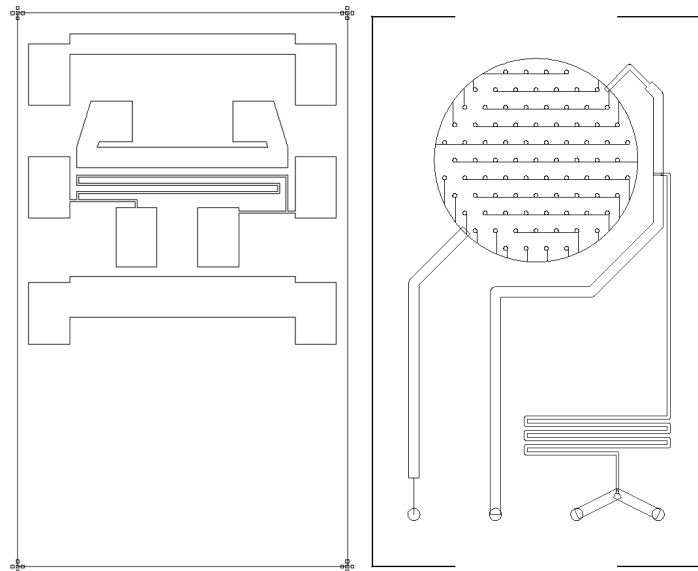


**Figure 3.8** – CAD-drawings of the longer reactor and the 10-point structure. The three strips are used for heating and the 4-point meander is used as the RTD. Original CAD-drawings by Thomas Pedersen.

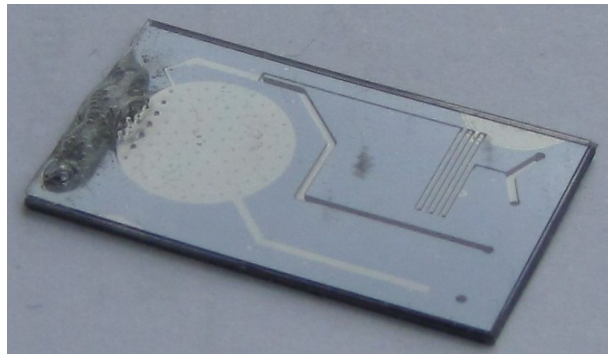


**Figure 3.9** – The actual actual chip implemented from the drawings in Figure 3.8. This particular device has a large bonding error between the meander structure and the surroundings and thus would not be able to function. At the top of the reactor, the melted lid demonstrates that we no longer have problems sourcing enough power into the device...

reasonably fast settled on a final layout. The point is that we will never be able to reach the perfect distribution anyway, and thus it is far more efficient to simply settle on a layout and then fix the problem with tunable external high-power resistors. In this way we can easily go through endless iterations by tuning the resistors and check the distribution in real-time on the thermographic camera. At the time of writing we are, unfortunately, not finished with this optimization, and the final temperature profile is not yet known. However, some initial experimentation leaves us with good expectations for the final result. As an evidence that we no longer have problems sourcing enough power, Figure 3.9 shows an image of a sample that was accidentally heated too high during a test.



## Chapter 4

# Measuring the Active Area of a Catalyst

Very often when doing measurements in the  $\mu$ -reactor, one will want to know the available active area of the catalyst. In some cases it can be very simple, for instance when working with metal thin-films. In these cases the area is more or less equal to the geometric area of the film, unless the catalyst is polluted with surface contaminants. In other cases, such if one wants to check if the catalyst is clean, or if the sample consists of nanoparticles, it is much less clear how to estimate the surface area. Often one will know how much catalyst was deposited, but how will we know, if the nanoparticles sintered or an attempt of cleaning has failed?

### 4.1 Procedure

The classic UHV procedure for measuring surface area of a catalyst is the TPD. The sample is exposed to a gas (typical CO) with subsequent heating of the sample. The amount of CO coming off is a measure of the surface area. However, this method is not quite as well suited in the  $\mu$ -reactors. We have tried to perform TPDs[16] and it certainly works, but sensitivity is rather poor. The problem is that in order to make a high-quality TPD you need really efficient pumping since only one gas species is involved; CO is dosed and CO is measured. In UHV this problem also exists but due to the generally very high pumping capacity of UHV chambers it is possible to bring down the CO background reasonably fast. In the  $\mu$ -reactors we have long pieces of 1/4" pipes which makes it difficult to eliminate the CO background after the dose. Thus one needs to do the TPD on this high background, with corresponding bad signal-to-noise, or wait for a very long time, which is both inefficient and also includes the risk that some of CO might desorb while waiting, unless the sample is cooled below room temperature. For all these reasons we wanted to find another method of area measurement, even if it means accepting the price of finding separate methods for each type of system.

The solution we are using so far, is developed for Pt and will most likely not work for most other systems, since it relies on the specific catalytic properties of Pt. The idea is to circumvent the background problem by measuring other masses than what is dosed. This of course means that the process must involve a step of catalytic conversion of the dosed species into a product of another mass. Since Pt is so remarkably efficient at oxidizing CO

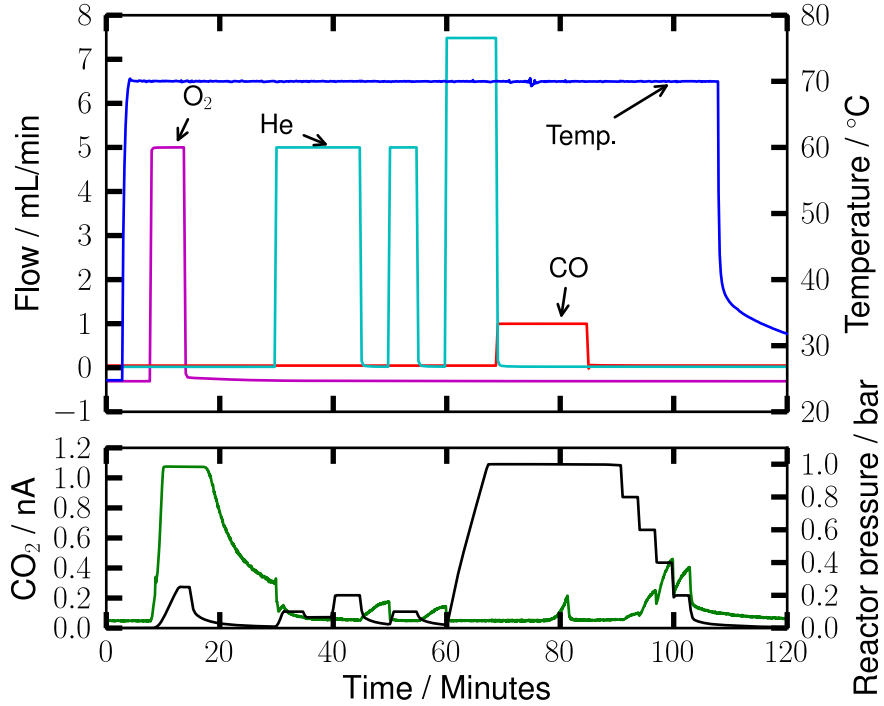


**Figure 4.1** – Plot of the area measurement procedure. Upper panel shows the flows of the incoming gasses and the lower panel shows the resulting CO<sub>2</sub> signal in the mass spectrometer (green) as well as the reactor pressure (black). The peak at  $\sim 80$  min represents the surface area. For a zoom of this peak, see Figure 4.2.

we chose a titration-like procedure which in short looks like this:

- Dose oxygen
- Evacuate reactor
- Dose CO and look for CO<sub>2</sub> in the mass spec

The oxygen dose (0.2 bar for 5 min) adsorbs a layer of oxygen on all free surface sites. The literature value for the full coverage is 0.25ML, however recently it has been shown the adsorption of oxygen on Pt is temperature dependent, and sub-surface layers will form at temperatures above  $\sim 125^\circ\text{C}$ [17]. The oxygen layer is very stable and will not desorb while the gas-phase oxygen is pumped and flushed away. In this way the QMS background is brought down significantly since we are now measuring on a species that was not explicitly dosed. However, the background is not totally eliminated since both CO and O<sub>2</sub> contributes with a background of CO<sub>2</sub> in the mass-spec, however the signal to noise is much better than a pure TPD. In reality the procedure is somewhat more complicated than described here, since we also need to dose a carrier gas before the CO to ensure a proper flow from the

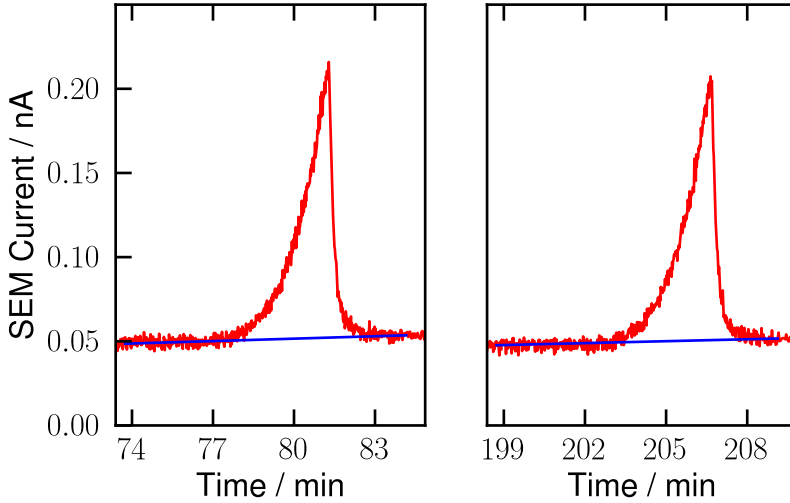


**Figure 4.2** – Zoom of the two first area measurements on the sample showed in Figure 4.1. The blue line is the background, which is not included in the area. The area of the first peak is 12.94 nC. The area of the second peak is 12.05 nC.

reactor and into the capillary outlet. For this we typically use helium. Also the helium is used to flush away the oxygen after the initial dose since this is faster than just pumping on the long tubes, especially on the old setup where we can only pump the tubes through the outlet of the sample. The complete procedure for area measurement is plotted in Figure 4.1. The entire procedure is performed at 70°C, in principle we can also run at room temperature, but since the conversion of adsorbed oxygen are much slower at this temperature, the slightly elevated temperature significantly increases the signal to noise ratio. The actual choice of temperature is a compromise between higher temperature which improves the measurement but might at the same time change the area we want to measure by e.g. sintering. After quite a bit of experimentation, the current value of 70°C seems to be a good compromise, signal is good and sintering is not expected to be relevant for Pt at this temperature[18].

The result of such a procedure is seen in Figure 4.2. This is a particularly simple example of two consecutive area measurements on a clean thin-film sample with an area of 7,85 mm<sup>2</sup> corresponding to 10% of the reactor area.

## 4.2 Area measurements of nanoparticles

Of course to be useful, the area measurements will also need to work on nano particle samples rather than just thin films. For this reason we have tested the procedure on several samples with deposited Pt nano particles. The particles were made with our cluster source here at CINF. The source is described in several publications[19, 20], but in short it consists of a gas-aggregation source where metal clusters are formed by gas-phase condensation in a magnetron sputter source. The condensed ions are then size-selected by a quadropole mass selection filter. The cluster source is supposed to be able to produce Pt nanoparticles with diameters in the range of 2–16 nm, however, the operators typically start to complain if one

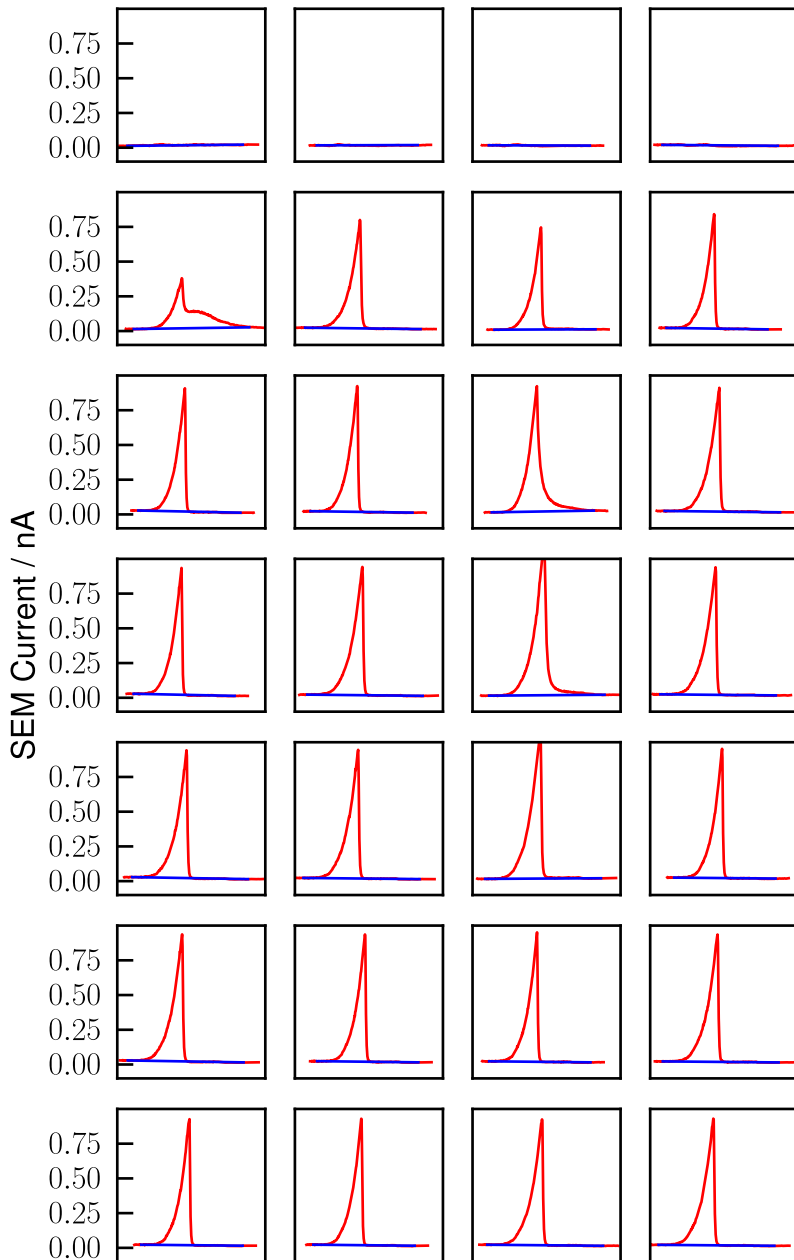


**Figure 4.3** – Plot of all measured areas on the cluster sample. Each panel shows the titration peak similar to Figure 4.2, on this particular sample a total of 28 area measurements was performed. It is evident that the signal is quite self-consistent, all measurements on a reasonably clean sample shows almost identical peaks only distinguished by differences in peak height. The duration of each plot is 100 s.

asks for particles below 3 nm or above 9 nm, so in practice this is the available range from this source. The data presented here is for a sample of 5 nm Pt clusters. The amount of clusters is estimated by measuring the beam current immediately before positioning the sample in the cluster beam. The deposition is timed in order to reach a geometric coverage of 40% of the reactor area, with the coverage calculated as the 2D-projection of spherical clusters of 5 nm. It is important to remember, that the clusters are mass-filtered, not shape filtered and spherical or Wulff-shaped clusters is not necessarily a realistic approximation. However, the convention on the cluster source is to always calculate coverage in 'spherical equivalents' ie. hypothetical spheres with mass corresponding to the filter mass. If the clusters are indeed spherical, it seems reasonable to expect them to wet the surface and land on the substrate as half-spheres, in this case it is easy to get a rough estimate of the expected active surface area. First we find the radius of the corresponding half-sphere:

$$V_{sphere} = V_{half-sphere} \Rightarrow \frac{4}{3}\pi R_s^3 = \frac{2}{3}\pi R_{hs}^3 \Rightarrow R_{hs} = 2^{1/3}R_s$$

Now we need to find the area exposed by a half-sphere with a radius corresponding to the 2D projection of a sphere of radius  $R_s$ :

$$\frac{A_{half-sphere}}{A_{circle}} = \frac{2\pi 2^{2/3} R_s^2}{\pi R_s^2} = 2^{4/3} \approx 2.5$$

That is, in the situation where spherical particles are formed and these particles lands as half-spheres, the expected measured area should be 2.5 times the nominal coverage. In our case we have a 40% cluster sample and want to compare to the 10% thin film already presented in this chapter. In this situation the expectation for the measured area should be that we will measure a relative area of

$$\frac{A_{cluster}}{A_{thin-film}} = \frac{40 \times 2.5}{10} = 10$$

The area measurement was performed by running four area measurements before any attempts at cleaning the sample. After this, the sample was subjected to a number of different treatments with two area measurements in between. Each area measurement is performed exactly as described in Figure 4.1, only the treatment in between the area measurements are changed. In Figure 4.3 all the raw data from the measurements are plotted for easy comparison to Figure 4.2. The treatments for this sample is:

- Heating to 420°C in 1 bar O<sub>2</sub>
- Heating to 300°C in 1 bar He
- Heating to 300°C in 0.5 bar CO
  
- Heating to 350°C in 1 bar O<sub>2</sub>
- Heating to 300°C in 0.5 bar CO
  
- Heating to 250°C in 1 bar O<sub>2</sub>
- Heating to 300°C in 0.5 bar CO

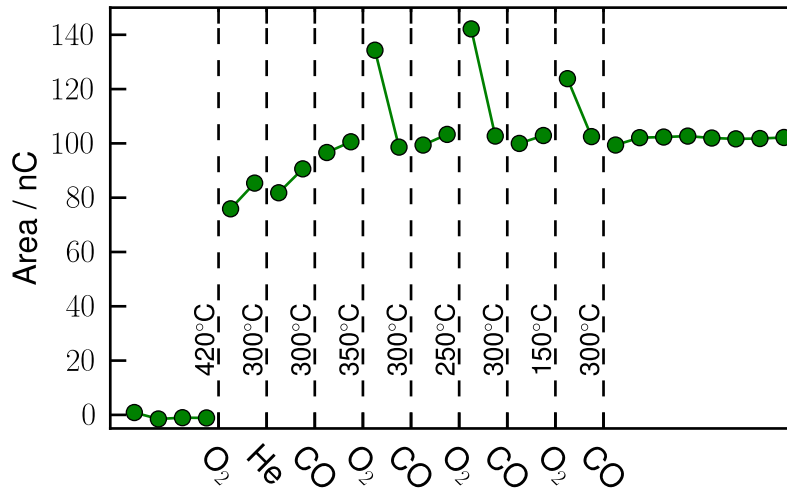


**Figure 4.4** – Summary of the measured areas on the cluster sample. Each vertical line represents a given heat-treatment, the temperature is indicated along the line, and the gas-species is written on the x-axis. Each data point is the result of a complete titration procedure as indicated in Figure 4.1.

- Heating to 150°C in 1 bar O<sub>2</sub>
- Heating to 300°C in 0.5 bar CO

The result of all the measurements are summarized in Figure 4.4 and the result is actually quite interesting. First of all it is evident that the sample shows no active surface area right after deposition and bonding, only after cleaning in oxygen do we see a measurable area. After this we see an asymptotically increasing area which one would guess is more an effect of the cleaning cycles themselves than on the heat treatments in He and CO. Finally, it is also evident that it is as expected possible to achieve higher oxygen coverage by heating a fairly clean sample in oxygen. Every area measurement immediately after this treatment shows an unusually large area. A final important observation is that the reproducibility seems to be excellent, the final eight consecutive area measurements shows almost identical results. The actual value of the area measurement for what must be presumed to be a clean sample is 102 nC which is approximately 8–8.5 times higher than the measured area for the thin film. This fits quite well with the expected factor of 10. Considering the amount of uncertainties in the cluster deposition, this high degree of agreement is properly somewhat of a coincidence. However, good sensitivity, high repeatability and very mild conditions for the sample means, that this method of area estimation is quite successful and can be used as a valuable tool when measuring on platinum catalysts.

## Chapter 5

# Oscillating reactions

At some point in time, we were running a bachelors project[16] concerning size dependence of reactivity of Pt nanoclusters in the  $\mu$ -reactor setup.

As part of the investigation we ran a simple CO oxidation experiment to calibrate equipment and get some basic data from the cluster sample for Mikkel to get started. This experiment was finished a Saturday and since nobody was around to change the sample, the setup was available for random experimentation. One of the things we had on the list of 'experiments to perform when we get the time' was a lightoff experiment with very low CO concentration to see how much this would bring down lightoff temperature (an ultra short introduction to the lightoff phenomenon is given in chapter 6), and thus it was obvious to let the setup spend the rest of the weekend on this.

After running this experiment we looked at the data (Figure 5.1) , and we were initially not very satisfied with the result. The data seems to show not only the expected CO conversion but also a very large amount of signal-noise. Normally the data is of much better quality, so we tried to investigate what could be the problem, and in this process it is natural to analyze the noise to see if it contains a hint about the root of the problem. A zoom of the data with a timescale short enough to resolve the individual spikes in the signal is shown in Figure 5.2. Much to our surprise, the noise turned out to be very well ordered, the two signals was going up and down in perfect anti-correlation. This of course strongly indicates that the signal is not caused by a simple noise source such as electrical noise or loose cabling in the mass-spec. The fact that the two signals was anti-correlated would be most easily explained by changes in the activity of the sample even though this was not our expectation for this reaction. To test the hypothesis, we performed the experiment several times on the same sample and came to the conclusion that the phenomenon was fully reproducible; if the sample is exposed to a very oxygen-rich CO/O<sub>2</sub> mixture and slowly ramped up in temperature, it would start oscillating. Soon we realized that this was a truly interesting phenomenon and we started a thorough investigation.

### 5.1 Existing literature

Once the initial excitement had settled and we came to the ordinary day to day work on the oscillations, we of course looked in to the literature to see if this had been seen before. A very famous example of oscillating reactions on Pt was discovered by Ertl and co-workers[21] more

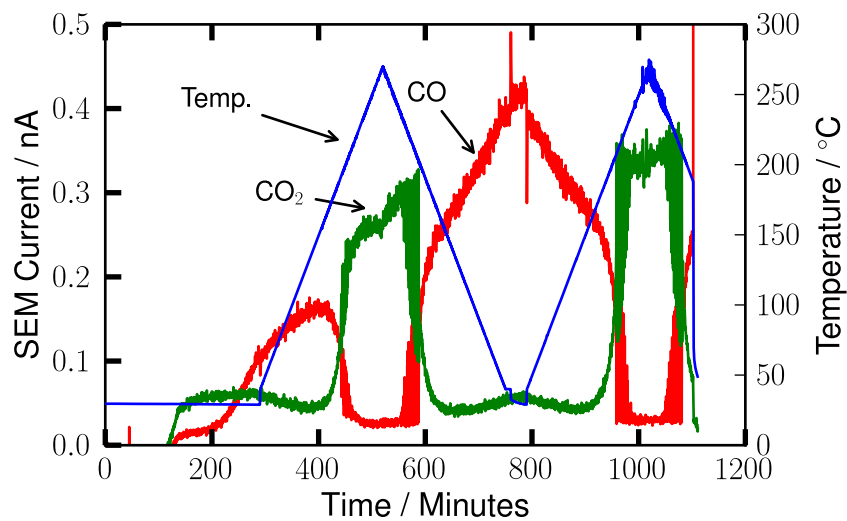


**Figure 5.1** – The first data set, showing oscillation behavior. On this time scale, the oscillations looks like noise.

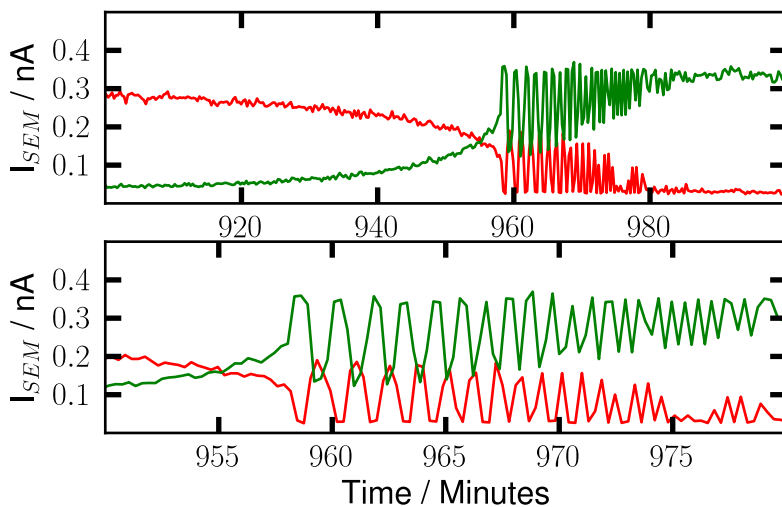


**Figure 5.2** – Two zooms of the 'noise' signal. Notice how mass 28 and mass 44 are perfectly anti-correlated.

than 20 years ago and the reaction at that time was actually also CO oxidation. However, the oscillating reactions discovered by Ertl was performed under UHV conditions and involves surface reconstructions on a Pt single crystal. Our experiments are performed at 1 bar on nanoparticles, and it is thus hard to imagine that the oscillation mechanism should be the same in our case. However, other people have found oscillations under reactions much more comparable to ours. The group of Joost Frenken has performed several high pressure studies on Pt and Pd single crystals, using both STM[22, 23] and more recently X-ray diffraction [24]. Oscillations has also been seen on extended thin films[25] as well as wet-synthesized nanoparticles, [26, 27]. Finally, also DFT calculations have been performed on systems like this[28].

Many of these papers have impressive in-situ measurements of the system while the oscillations are running and consensus seems to be that oscillations originate from the surface switching between an oxidized and a reduced state with the oxidized state being the most active. Since we do not have access to traditional surface science techniques in the  $\mu$ -reactors, our focus has been on getting truly high quality mass spectrometry and to investigate a fairly large parameter space, among this the temperature dependence, which has to our knowledge have not been done before.

## 5.2 Experimental procedure

After some experimentation we found an experimental procedure, which almost consistently ended up with an oscillating sample. As with almost all experiments, we do not do any pre-treatment (except of course the anodic bonding) before mounting the sample in the setup. Initially after mounting the sample, a light-off CO-oxidation measurement is performed (shown in Figure 5.3) where the temperature is increased at  $3^{\circ}\text{C}/\text{min}$  until the sample ignites and achieves full conversion of CO to  $\text{CO}_2$ . At a  $\text{CO}:\text{O}_2$  ratio of  $\sim 0.08$  and a geometrical Pt coverage of the reactor area of  $\sim 0.1\%$ , light-off occurs at approximately  $180^{\circ}\text{C}$ . The temperature ramp is typically continued a bit above light-off temperature, mainly to be sure to actually achieve light-off. Typically we continued the ramp up to  $260^{\circ}\text{C}$  where after the temperature is again decreased also at  $3^{\circ}\text{C}/\text{min}$  until we reach room temperature. The temperature is again increased at  $3^{\circ}\text{C}/\text{min}$  until sustained oscillations occur. Since we leave the setup unmonitored the temperature of sustained oscillations must be estimated beforehand, but typically a temperature between  $200^{\circ}\text{C}$  and  $220^{\circ}\text{C}$  works nicely. An example of an initial treatment is seen in Figure 5.3 where both the symmetrical light-off ramp and the subsequent increase in temperature to achieve sustained oscillations is seen. Often the sample will show oscillations either directly upon light-off or on the falling temperature ramp. The oscillations on all samples are qualitatively similar but the oscillation period varies from a few seconds (comparable to the time constant of the reactor) up to more than an hour. Once a sample starts to oscillate it will perform self-sustained oscillations for as long as the experiment is allowed to run. We have not observed a single sample stop oscillating once the self-sustained oscillations had started.

An example of a single very slow oscillation is seen in Figure 5.4. After a short on-cycle (at  $\sim 1030$  min) where all CO is converted to  $\text{CO}_2$  the reaction shows a fast deactivation. After the deactivation the sample quickly regains  $\sim 30\%$  conversion (at  $\sim 1040$  min). Hereafter the conversion increases slowly over time until approximately 50% conversion is reached (at  $\sim 1118$  min). Shortly after reaching 50% conversion the sample again ignites and converts all CO to  $\text{CO}_2$ . After a short full conversion period the sample again deactivates and the cycle repeats itself.

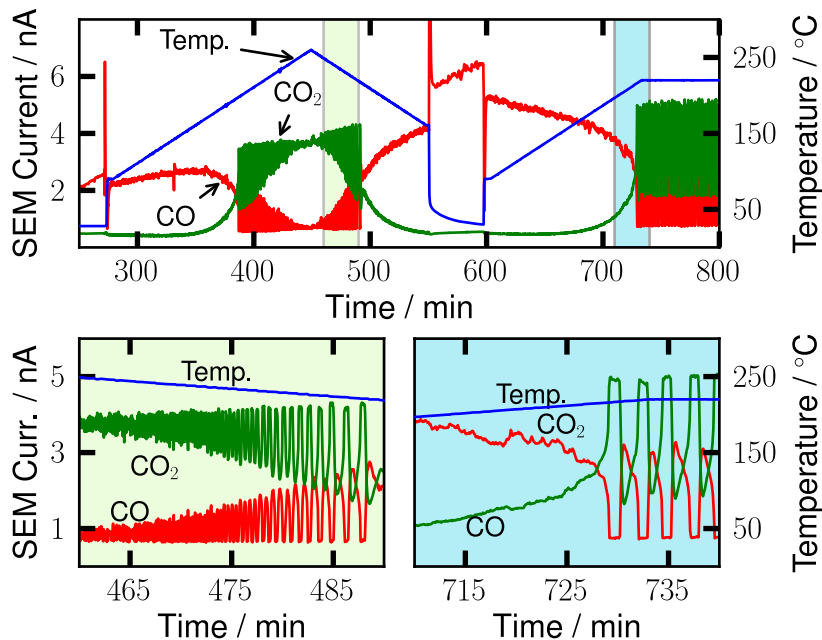


**Figure 5.3** – A typical example of the initial treatment of a new sample. After performing a light-off ramp, where oscillations can be seen, the temperature is increased to a constant value where sustained oscillations take place. The non-zero value of CO during high conversion periods is consistent with the expected QMS background signals from  $\text{CO}_2$  and  $\text{O}_2$ .

We of course spend quite a lot of effort to ensure that the phenomenon is a true property of the catalytic system and not an artifact of the experimental setup. Due to the long timescales between full conversion and low conversion plateaus the oscillations cannot be attributed to the reactor itself which of course have a much shorter timescale. Furthermore, we did a series of experiments to exclude that this could be due to the flow controllers or perhaps the temperature control system. Firstly, in the clean-room Thomas prepared lids for the reactor with a deep etch on the lid at the position of the reactor. This of course greatly increases the timescale of the reactor and thus we should be able to tell if the oscillation phenomenon should be due to unforeseen coincidence between the reactor and other characteristic timescale of the system. This sample also oscillated. Of course we also reproduced the oscillations on the NG setup. Even though this setup is in principle a copy of the old setup, it is sufficiently different that it is hard to imagine experimental artifacts to be identical; in the new setup we have a different PID implementation, different length of the tubing as well as other flow controllers. Also this test showed oscillations with the same initial treatment. Finally we also did quite an effort to reproduce the phenomenon on Pt thin film of comparable coverage without ever seeing a single oscillation. We do not really understand why we cannot get thin-film samples to oscillate, it is known in literature to be possible[25], but we cannot reproduce this. However, at least the fact that these sample does not oscillate also strongly point towards the phenomenon not being an instrumental artifact.

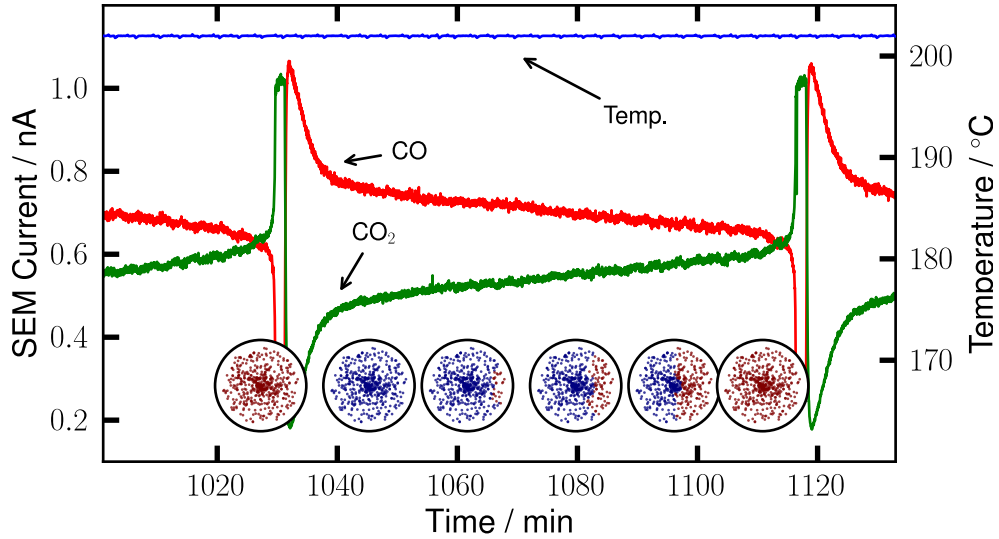


**Figure 5.4** – A full oscillation period first showing a steep ignition of the sample followed by an almost immediate deactivation. For the next 65 minutes the sample slowly recovers activity until full conversion is reached again and the cycle repeats itself. This extremely long oscillation period is not commonly seen and was a result of careful parameter tuning. Typical oscillation periods are normally between  $\sim 30\text{ s}$  and  $\sim 30\text{ min}$ . Inserted circles illustrates the proposed model. At high conversion the platinum is oxidized (red) while in low conversion the sample is reduced (blue).

After prolonged measurements over several days an increase in oscillation period was observed as shown in Figure 5.5. Initially, the oscillation period is  $\sim 2.5\text{ min}$  and it increases linearly with time until  $1500\text{ min}$  of total oscillation time. Hereafter the oscillations become more irregular as shown in the lower panel of Figure 5.6 . At experiment end the oscillation period is between  $20\text{ min}$  and  $45\text{ min}$ . Figure 5.6 shows extracts of mass spectrometry data of oscillations extracted from the same four days measurement. Data from shortly after the initial treatment, after  $2800\text{ min}$  of oscillation time and after  $5900\text{ min}$  are shown. After  $5900\text{ min}$  the oscillations are more irregular which is consistent with the data shown in Figure 5.5. Also, oscillations in between full conversion oscillations with smaller amplitude and much higher frequency than the full on-off cycles become more visible as time progresses. This overall phenomenon of less stable and slower oscillations is consistent across all measured samples. The large scatter in oscillation period can be attributed to the smaller oscillations in between on/off cycles. Occasionally, these small amplitude oscillations will trigger a full switch thus introducing more short-period oscillations despite the trend of increasingly longer oscillation period. A possible explanation of the phenomenon could be sintering of the particles during the oxidation and reductions cycles. However, as shown in Figure 5.7, the ratio between CO and CO<sub>2</sub> integrated over a full oscillation period remains constant throughout the entire experiment time, i.e. the samples maintain a constant average rate independent of oscillation frequency. Thus we do not expect sintering to be the cause since an average loss in activity of the sample would then be expected. Unfortunately, this means that we have to accept that we so far do not have a satisfactory explanation of the increasing

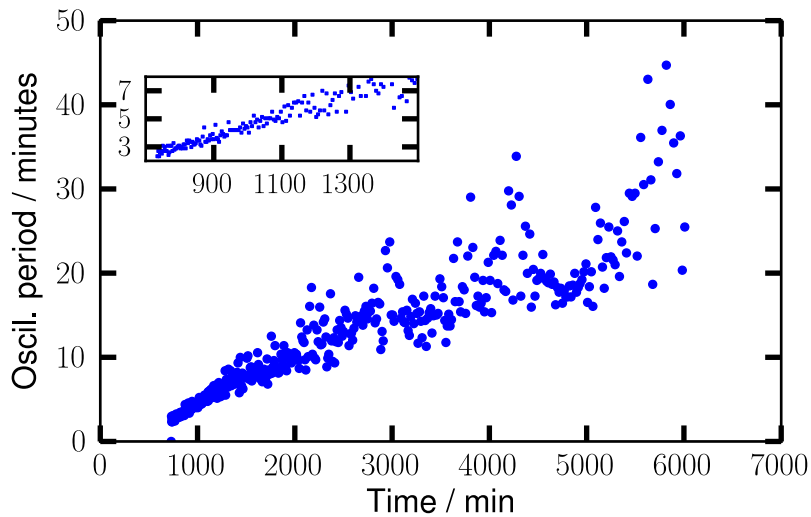


**Figure 5.5** – Summary of the oscillation period as a function of time for a sample oscillating under constant temperature, pressure and reactant composition. The sample went through a total of 439 oscillations in 4 days. Time is defined from experiment start and hence includes initial treatment. The inset shows the initial steady increase in oscillation period. The red lines indicate max and min oscillation time to guide the eye.

period.

### 5.3 Exploring the parameter space

One great advantage of the  $\mu$ -reactor setup is that we can fairly easily investigate a rather large parameter space of many different physical properties. In this system, the number of parameters to test is almost infinite, so we had no problems finding several properties to investigate. One significant complication in this exploration is that the reproducibility between samples is frustratingly low. Two nominally identical samples show very different oscillation frequency and thus it is very hard to conduct systematic studies. However, since each individual sample show a very predictable behavior of slowly increasing oscillation period, it is still possible to learn something by changing the value of temperature, pressure, etc. and watch for the change in oscillation frequency.

The reason for the lack of reproducibility is properly due to a combination between irregularities in the deposition and the significant temperature gradient in the reactor. This means that if two otherwise identical samples are deposited at slightly different positions in the reactor, the actual sample temperature will be different, even if the measured RTD temperature is the same. This in combination with rather large uncertainties in the deposited amounts for these low coverages are a very likely explanation for the poor reproducibility. Hopefully the temperature issue will be greatly reduced by the new heaters, and we are also looking into options for getting better deposition consistency.

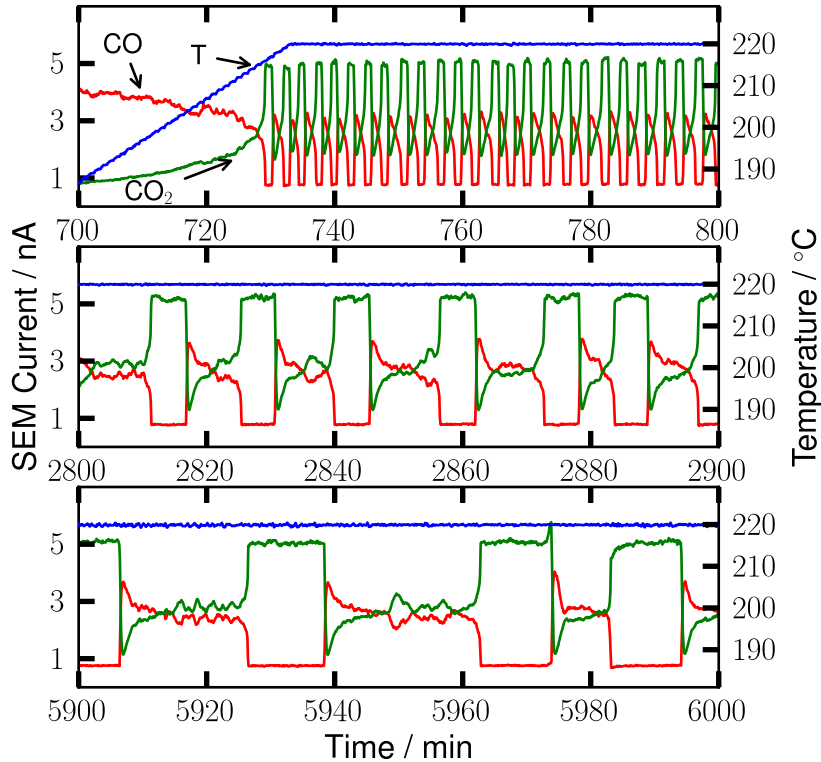


**Figure 5.6** – The oscillation period becomes more irregular with time while the total integrated conversion remains constant. Furthermore, small oscillations in between full conversion cycles become more prominent as time progresses.

### 5.3.1 Temperature dependence

An interesting feature in the data is the very large temperature dependence of the oscillation frequency as shown in Figure 5.8. By changing the temperature  $5^{\circ}\text{C}$  the oscillation period was changed by more than a factor of 10. The magnitude of the change is not completely consistent across all measured samples but all samples show a very large temperature dependence. In some cases a provoked change in temperature will consistently turn on and off the oscillations. This is illustrated in Figure 5.9. This property agrees with an earlier suggested model [24] and it is, to our knowledge, the first time the temperature dependence of oscillations at atmospheric pressure has been measured.

### 5.3.2 Pressure and CO concentration dependence

The pressure dependence of the oscillations was also investigated. In the pressure range of 0.1 bar to 1 bar no change of the oscillation frequency or qualitative behavior that could be

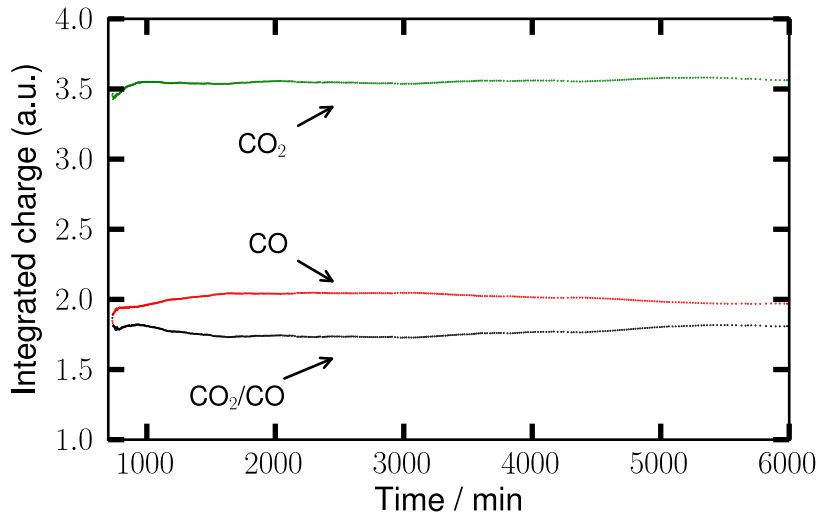


**Figure 5.7** – Plot showing the value of the  $\text{CO}_2$  signal (green) and  $\text{CO}$  signal (red) averaged over each oscillation cycle. The black line shows the ratio between the two signals. It is evident that the total conversion is almost constant for the entire period despite the fact that the oscillation period has increased by a factor of  $\sim 20$ .

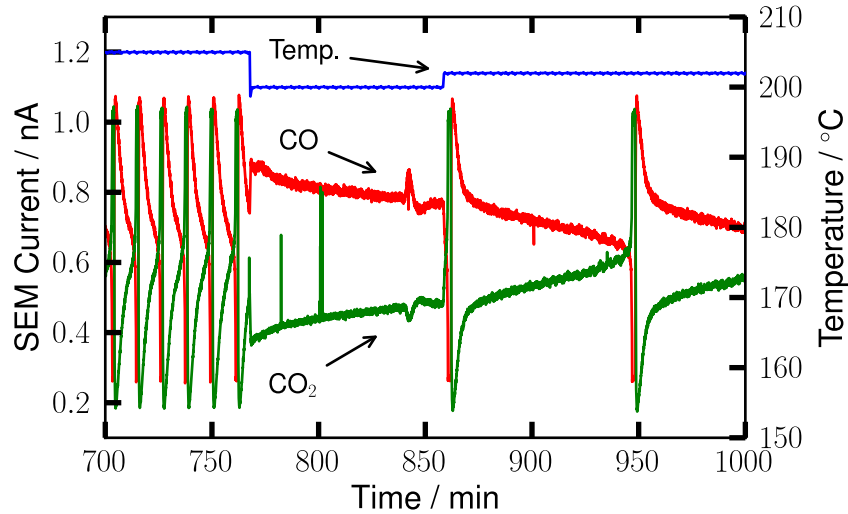


**Figure 5.8** – Illustration of the strong temperature dependence of the oscillation period. After about 10 hours of steady oscillations at  $205^\circ\text{C}$  the temperature is lowered by  $5^\circ\text{C}$  immediately decreasing the oscillation frequency. The temperature is hereafter increased by  $2^\circ\text{C}$  resulting in an increase in oscillation frequency. At  $205^\circ\text{C}$  the oscillation period was approximately 500 s. while the oscillation period is approximately 5000 s. at  $203^\circ\text{C}$ .

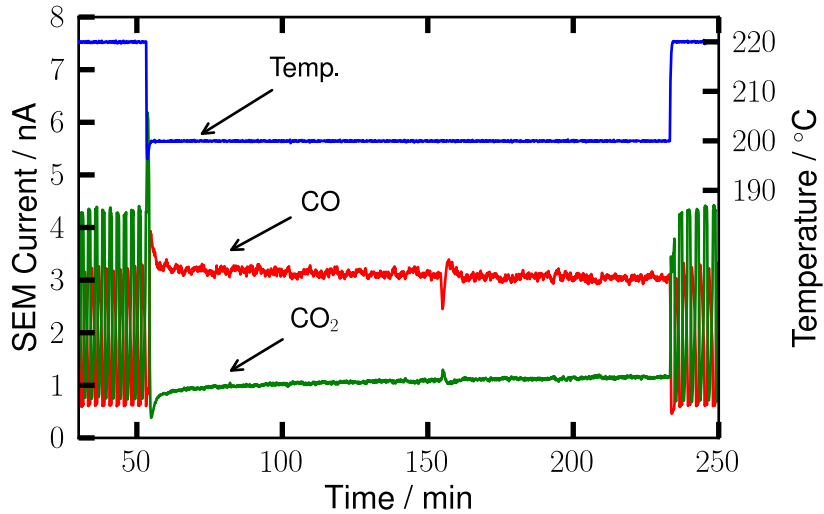


**Figure 5.9** – Another example of the very pronounced temperature dependency. In this case the oscillations are consistently turned on and off by changing the temperature  $20^{\circ}\text{C}$ .

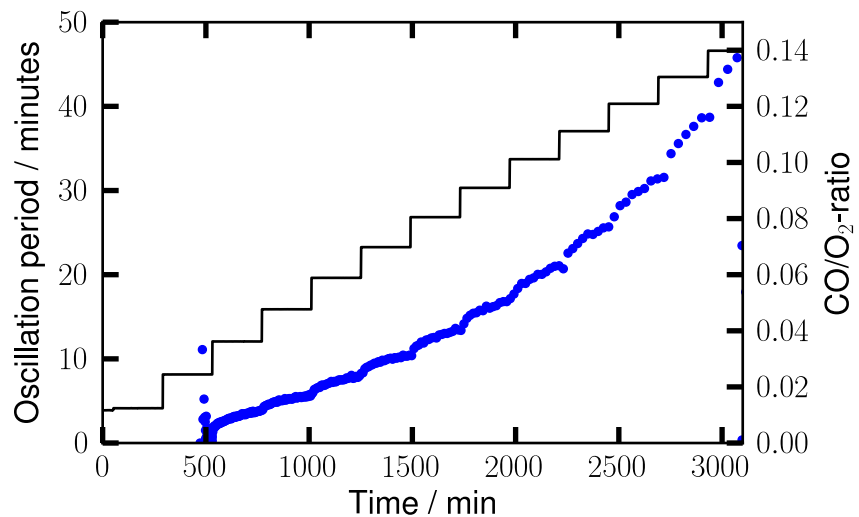


**Figure 5.10** – Summary of the CO concentration dependence experiment. As with all other measured samples, the oscillation period increases with time, but also small step-like increments are seen for each increase in the CO concentration.

attributed to the pressure was found. Only a weak dependence on the CO/O<sub>2</sub> ratio was observed; the period increases slightly with increasing CO-concentration. However, the effect is small compared to the general trend of slower oscillations as the experiment progresses. In Figure 5.10 the oscillation periods are summarized and the actual mass spectrometry data of the entire experiment is shown in Figure 5.11.

Oscillations were only seen in CO/O<sub>2</sub> ratio below 0.175. This ratio agrees well with literature[25, 23] where oscillations have been observed in oxygen rich CO/O<sub>2</sub> mixtures. The needed low concentration of CO in the inlet gases can be attributed to the much higher sticking coefficient of CO on Pt which poisons the nanoparticle surface during the low reactivity region of the cycle.

### 5.3.3 Size dependence

Nanoparticles with sizes ranging from 3 nm to 9 nm have been tested but 3 nm particles with a geometrical coverage of 0.1% of the reactor area gave the most stable oscillations. However, no change in duty cycle or frequency that could be attributed to the size of the nanoparticles was found. As mentioned, the reproducibility between samples are frustratingly low and since the size dependence must necessarily involve comparing different samples, the large variation between samples possibly shadows a nanoparticle size effect.

## 5.4 Oscillation mechanism

It has previously been shown using STM[22], FT-IR[27], Monte Carlo simulations[26] as well as DFT[28] that the activity of Pt towards CO oxidation at atmospheric pressures is highly dependent on the oxidation state of the surface. A detailed proposal for the reaction mechanism on Pd has been developed by Hendriksen *et. al.*[24] and our data are consistent with this model.

According to the proposed model by Hendriksen, the bare metal surface is less active than the oxidized surface. Oscillations originate from a switch between an oxidized surface and the bare metal surface. Initially, with CO present in the inlet gas a smooth metal surface is exposed due to the general high adsorption energy of CO on metal surfaces. As the Pt nanoparticles convert the CO to CO<sub>2</sub> the partial pressure of CO will decrease and a Pt oxide will start to form in the high partial pressure of O<sub>2</sub> thus increasing the rate. The model suggests that the oxidized nanoparticles will roughen during CO oxidation, resulting in the formation of an increasingly rough oxide surface. As the oxide becomes rougher the bare metal surface is increasingly favored because the metallic state has a lower surface energy than the oxide in the presence of CO. This results in a sudden return to the lower rate rough metal state. Since the surface mobility is higher for the reduced surface[24], the roughness of the surface will gradually decrease and result in a slow transition from rough metal surface to a smooth metal surface. When the sample is sufficiently smooth it will again oxidize, increase the conversion rate, and thus complete the oscillation cycle.

In this study Pt nanoparticles were investigated which, compared to a single crystal or a thin film, have a very rough surface. It is to be expected that the particles will initially favor the reduced state. As the reaction runs the gas composition towards the outlet of the reactor will become more oxidizing increasing the oxidation rate of the particles (illustrated in the bottom of Figure 5.4). Gradually, as the particles towards the outlet oxidizes, the turn-over frequency will increase and the general CO concentration will decrease promoting

more and more particles to oxidize which will gradually be seen in the QMS as an increase in CO<sub>2</sub> and a decrease in CO. As the CO concentration decreases the light-off temperature will decrease hence approaching the constant temperature of the sample resulting in a sudden steep increase in reactivity. It is important to note that the fraction of oxidized particles needed to achieve full conversion is not known, since this will depend strongly on the detailed ultra local temperature distribution around each nanoparticle, and since CO oxidation is strongly exothermic, the particles might be significantly hotter than the global temperature of the reactor. We have made quite an effort to try to image this hypothetical local temperature increase, but we have so far not succeeded.

If all particles are not oxidized at light-off they will now oxidize much faster due to the low CO-concentration. The further increased rate will not be visible in the QMS since the reactor is already in full conversion. As most of the particles are now oxidized they will become more and more roughened and gradually return to the reduced state. Fewer and fewer oxidized particles will be responsible for the activity increasing the roughing rate of the remaining active particles. Just before the overall activity drops only a fraction of the particles participates in the reaction and the deactivation will happen very suddenly, hence completing the oscillation cycle.

## **5.5 Conclusion**

As discussed in the introduction, not many specific results has made its way to thesis. However, this particular system has become a bit of a favorite partly because it was serendipitously discovered, and partly because it seems to fit so well for investigation in the microreactors. Even though we do not have access to in-situ methods, we are still able to provide new insights into this interesting phenomenon. It is currently a great frustration that the inter-sample repeatability is so bad, but at the same time this is also a great motivation to improve the temperature distribution as well as the deposition technique. Once these problems are solved, one could hope to be able to map out several parameters including the size dependence of the oscillations, which is of course of great interest in our group.

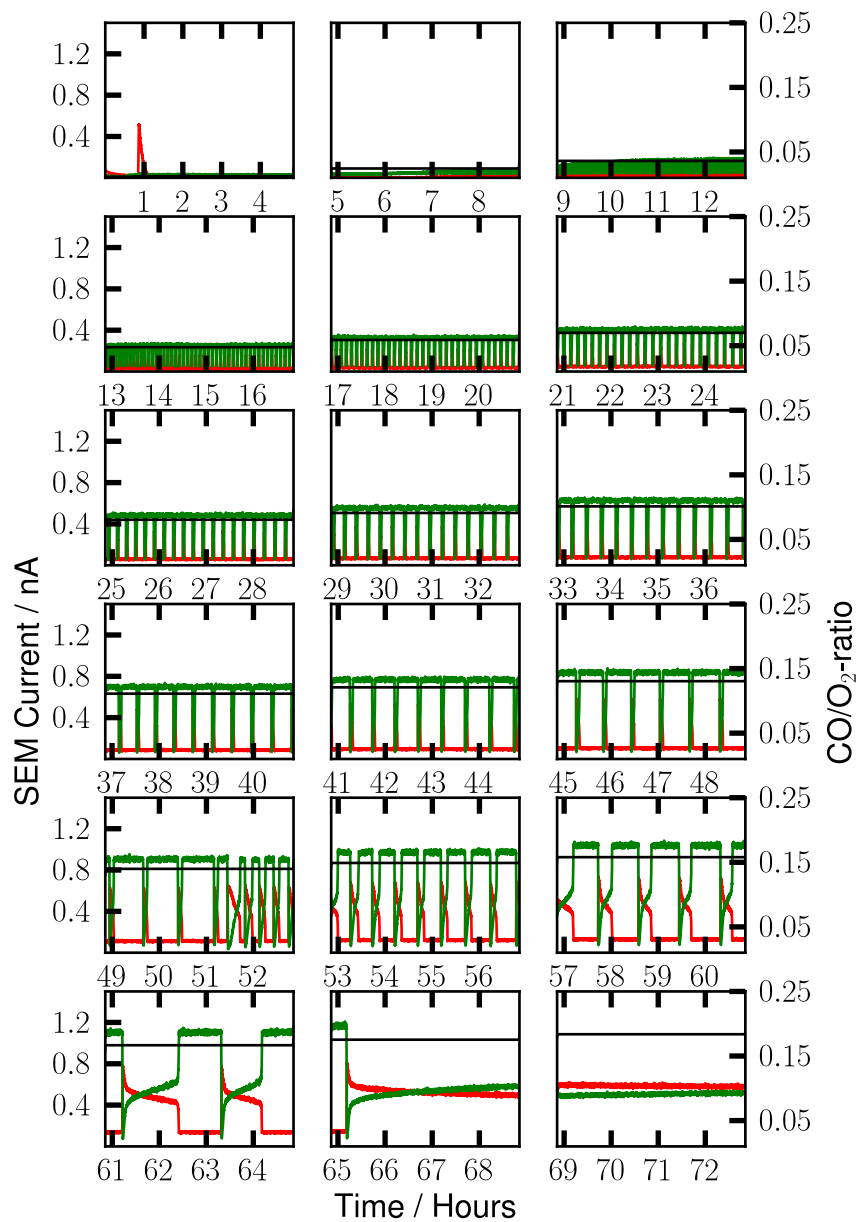


**Figure 5.11** – Complete series of data from an oscillating sample, showing CO (red) and CO<sub>2</sub> (blue). The temperature is constant at 210°C during the entire measurement. For every frame the CO-concentration is increased.

# Chapter 6

## Sensitivity measurements

One of the original design goals of the  $\mu$ -reactors was that the reactors should have a high sensitivity to be able to measure on very small amounts of catalyst. This high sensitivity was confirmed during the measurements on the oscillations since it turned out that we were in fact able to reach full conversion on samples with even very small amounts of catalyst. At some point we thought that it would be interesting to test how small amount of catalyst we can actually get to full conversion. To test the sensitivity we have performed a series of tests using CO oxidation on Pt thin films as test reaction.

### 6.1 Experimental procedure

The experiment is in principle very simple, although rather time consuming. We had our good friends in the clean room make a series of samples with consecutively smaller and smaller Pt-spots and then ran a series of CO oxidation experiments. Unfortunately, not all samples were measured due to various kinds of bad luck, but we did manage to measure on a rather large diversity of sizes, as seen in table 6.1.

CO oxidation on Pt is a reaction that follows a so-called light-off curve when the sample is heated. This phenomenon originates from the fact that CO has a much higher sticking coefficient than oxygen on Pt[29]. Due to this high sticking coefficient, every free site on the sample will immediately be occupied by CO once the sample is exposed to the reacting gas. The lack of free sites on the sample prevents oxygen from adsorbing on the catalyst and prevents the catalytic conversion. When the temperature of the sample is increased, the residence time of CO on the sample will become shorter and shorter and eventually the

#	Radius / $\mu\text{m}$	Area / $\mu\text{m}^2$	Reactor coverage
N5	3.5	38.5	$4.9 \times 10^{-7}$
N8	15	707	$9 \times 10^{-6}$
N9	25	1960	$2.5 \times 10^{-5}$
N10	50	7850	$1 \times 10^{-4}$
N11	250	196000	$2.5 \times 10^{-3}$

**Table 6.1** – The Pt samples that has so far been measured in the sensitivity measurement.

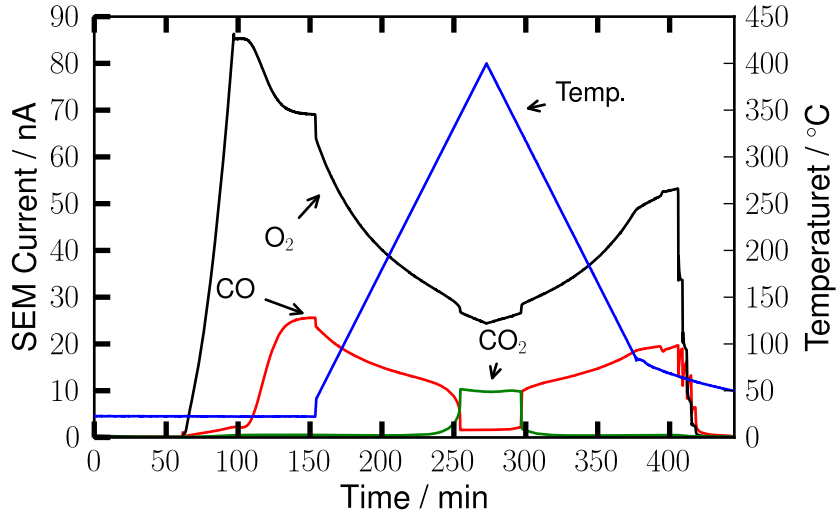
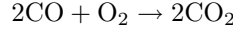


**Figure 6.1** – The general procedure for the sensitivity measurements. In this case sample N8 with a radius of  $15\text{ }\mu\text{m}$  is shown. The sample is heated in a lean mixture of CO and O<sub>2</sub> and the temperature is gradually increased until light-off occurs.

oxygen will gain access to free Pt-sites. Once this happens, the oxygen will react with the CO according to the reaction equation:



An oxygen molecule will burn off two CO molecules and produce CO<sub>2</sub> which has an extremely short residence time on Pt, leaving two additional free sites[30]. These new free sites will provide room for even more oxygen molecules and it is easy to imagine how the Pt surface will 'ignite' and react off all CO very suddenly. This phenomenon is known as lightoff and has a clear experimental signature in the form of an extremely sudden onset of the reaction as well as significant temperature hysteresis. This is due to the fact that when the sample cools down it still has free sites and thus it will sustain conversion to far lower temperatures than the ignition temperature.

The experiments were all performed by the following procedure. Oxygen and CO are dosed in a ratio of 4:1 for  $\sim 9000\text{ s}$ . At this time the flows has stabilized and we have constant signals in the mass spectrometer. The temperature is then increased by  $3^\circ\text{C}/\text{min}$  at least until full conversion is reached. Finally, the sample is cooled, also at  $3^\circ\text{C}/\text{min}$ , until the sample is no longer able to cool at this rate. From this point the sample is allowed to cool a bit further until finally the sample is again evacuated.

As the spot size gets smaller and smaller, we need to go to higher and higher in temperature to achieve full conversion of the reacting gas. As mentioned in chapter 3, the current heater design is not really performing well when going much higher than  $\sim 400^\circ\text{C}$  and thus heating is so far the limiting factor in these experiments. The highest temperature we have reached was  $\sim 420^\circ\text{C}$  which was almost enough to reach full conversion on a Pt spot of  $38\text{ }\mu\text{m}^2$ .

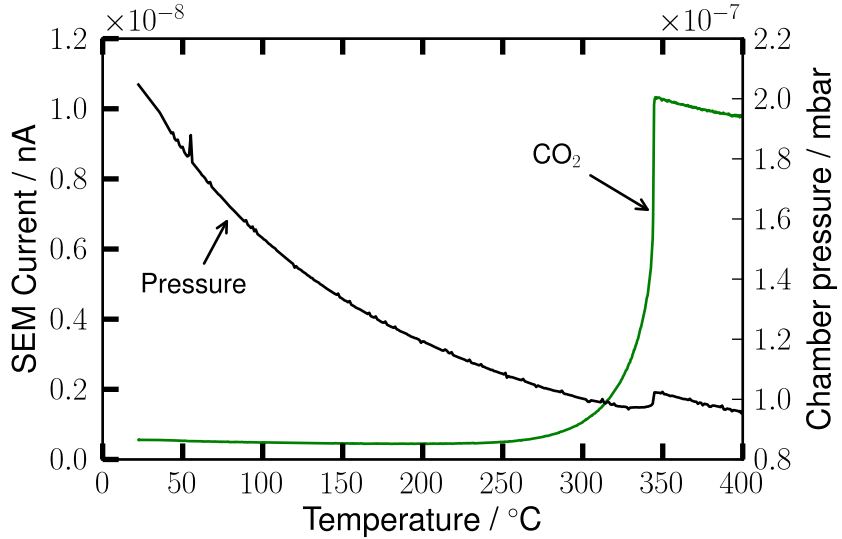


**Figure 6.2** – Due to increased flow resistance in the capillary, the pressure in the main chamber drops with temperature. It is easy to see that the apparent pressure increases once the sample reaches full conversion, this is an artifact because of the high ionization cross section of CO<sub>2</sub>.

## 6.2 Data treatment

Even though the experiment sounds simple, data treatment is actually slightly complicated due to the nature of the  $\mu$ -reactor. Several steps are involved and in the following each step of the data treatment is presented.

### 6.2.1 Capillary flow

The reactors have the intrinsic property, that the capillary flow is decreased as the temperature increases due to an increase in the flow resistance with temperature. This means that even for constant conversion (as would be the case for full conversion) the product signal in the mass-spec will decrease with increasing temperature. Strictly speaking it is not necessary to correct for this effect since we are currently using the mass spectrometer signal directly to calculate the turn over frequencies of the CO oxidation. However, if one later wants to do a more sophisticated analysis, quantification of the flow is of great value. To quantify the capillary flow, one will typically use the main chamber pressure as a measure of the flow. However, this is also a non-trivial operation because of the way the pressure is measured in the chamber, namely by an ion gauge. Ion gauges measure pressure by ionizing the residual gas and collect the ions on a thin collector wire in the center of the device. The pressure is then read as the current on the collector times a calibration factor[31]. The correction factor is what gives us problems in the current application since the product, CO<sub>2</sub>, has a sensitivity factor that is considerably different from CO and O<sub>2</sub>. Compared to nitrogen the values are[32]: CO: 1.05, O<sub>2</sub>: 1.01, CO<sub>2</sub>: 1.42. Since CO<sub>2</sub> is the only involved gas to have a factor significantly different from 1, we should expect to see the apparent chamber pressure to increase when the sample gets into lightoff as demonstrated in Figure 6.2. Both because of this effect and because our ion gauge signal is a bit more noisy than one would like, it would

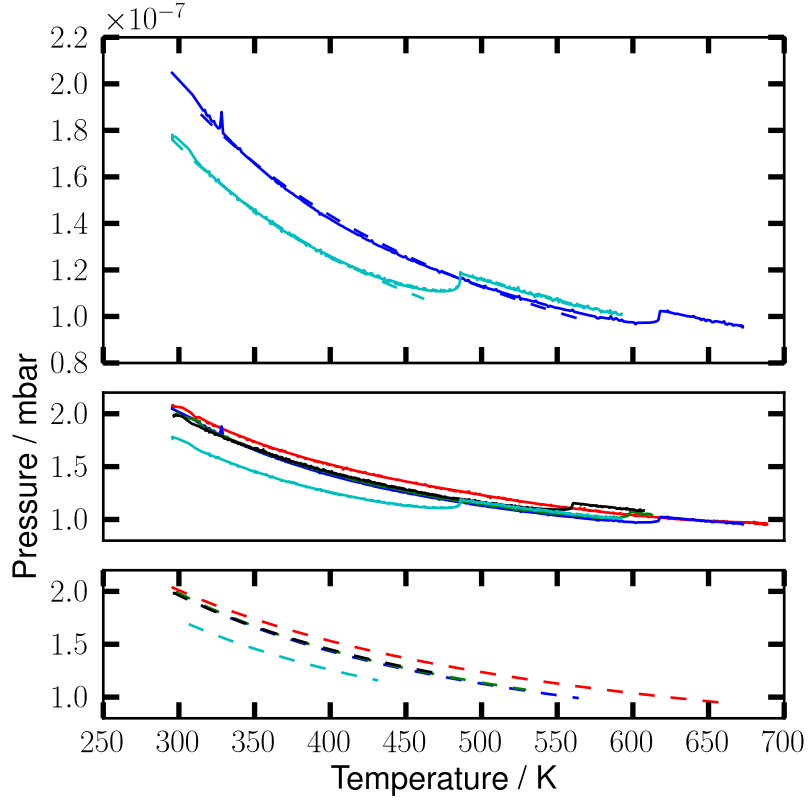


**Figure 6.3** – Fitting of analytic functions to the temperature dependence of the flows. For clarity the upper panel shows only two sets of data along with the corresponding fit. Middle panel shows all raw data and lower panel shows all corresponding fits. Color code: N5: Red, N8: Blue, N9: Green, N10: Black, N11: Cyan.

be desirable to find an analytic expression to estimate the flow as a function of temperature. A bit of experimentation with various expressions for fitting the flow dependence, shows that the behavior can be well described by a function of the form:

$$F = \frac{k1}{k2 + T}$$

In Figure 6.3 this expression has been fitted to all five measurements and it is seen that data can be fitted reasonably well and we end up with a smooth expression for the flow as a function of temperature.

### 6.2.2 Background signals

To quantify the CO<sub>2</sub> production from the sample, it is necessary to correct for the background signals in the mass-spectrometer. Since the experiments are run in a rather large excess

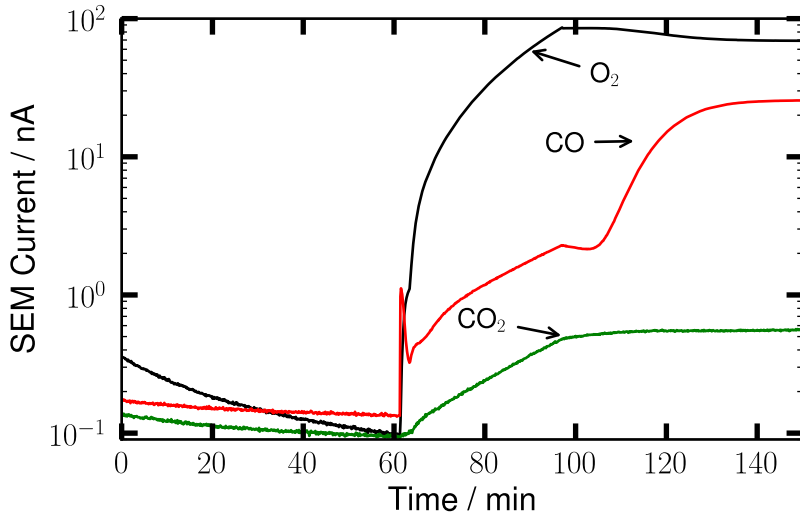


**Figure 6.4** – Mass spectrometer signals from CO, O<sub>2</sub> and CO<sub>2</sub> before the heating starts. It is evident that the CO<sub>2</sub> background primarily follows the oxygen signal.

of oxygen, oxygen will always be present in the flow into the main chamber. In the mass-spectrometer, the oxygen will give rise not only to a signal at mass 32 (the oxygen itself), but also a signal at mass 44, which is in our case CO<sub>2</sub>. The reason for this is that the mass-spectrometer filament will always contain carbon and because of the very high temperature of the filament, this carbon will react efficiently with the oxygen and produce CO<sub>2</sub>. One could also imagine that the CO and O<sub>2</sub> would react on the filament, but examination of the CO<sub>2</sub> signal shows a much closer correlation to O<sub>2</sub> alone than to the combination of CO and O<sub>2</sub>. Most likely, the pressure in the main chamber is simply too low for gas-phase reactions to happen.

This means that the total measured CO<sub>2</sub> signal will, at least as a simple first approximation, be the sum of three signals, namely the actual CO<sub>2</sub> production, the background from the presence of oxygen and the permanent residual background in the main chamber. Reading from Figure 6.4, it is found that the CO<sub>2</sub> background is approximately  $8.2 \times 10^{-3}$  times the oxygen signal. In Figure 6.5 the background correction is performed for sample N8. It is evident that the correction greatly extends the temperature range with Arrhenius behavior. In Figure 6.6 the background correction is performed on all measured samples.

Once all the corrections are performed as well as possible, it is time to extract an activation energy and a prefactor for each platinum spot. The point of the experiment is to see how small the spot can be and still withhold a constant activation energy as well as a prefactor linearly dependent on the spot area. To do this, we fit the data to the the Arrhenius equation:

$$k = Ae^{-E_a/k_bT}$$

which will give the activation energy as well as the prefactor. The fitting is performed by a small python script which takes data from the CINF database and fits the data.

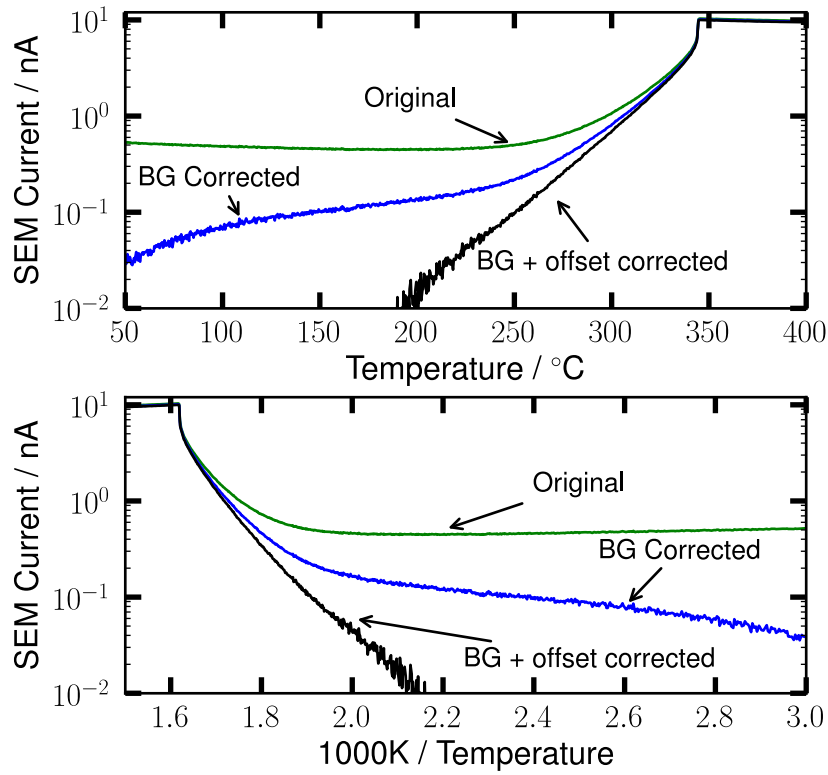


**Figure 6.5** – Example of the background correction. The green line is the raw M44 signal from the mass spectrometer. Blue line is the same signal subtracted  $8.2 \times 10^{-3}$  times the oxygen signal. Black line is the blue line minus a constant value of 0.12 nA, which corresponds to the constant M44 background in the chamber.

### 6.2.3 Mass spectrometer calibration

A mass spectrometer does not measure the ion current directly, but measures the signal after it has passed through the Secondary Electron Multiplier (SEM). The amplification on the SEM is of course heavily dependent on the voltage across the dynodes but unfortunately it also depends on many other factors such as the oxidation state of the SEM and the mass of the impeding molecule. On top of this, the mass filter itself is also not guaranteed to have a fixed transmission efficiency across the entire measuring range. Finally it is difficult to estimate the fraction of molecules that enters the mass spectrometer, compared to the fraction that are directly pumped away in the main chamber. All these factors means that it is highly difficult to estimate the absolute yield of a given molecule. Only the indirect quantity SEM current is truly known. However, it is possible to make at least a rough estimate of the overall sensitivity factor, as long as one remembers that the value should not be considered to be very accurate. Looking at Figure 6.4, it is evident that the conversion

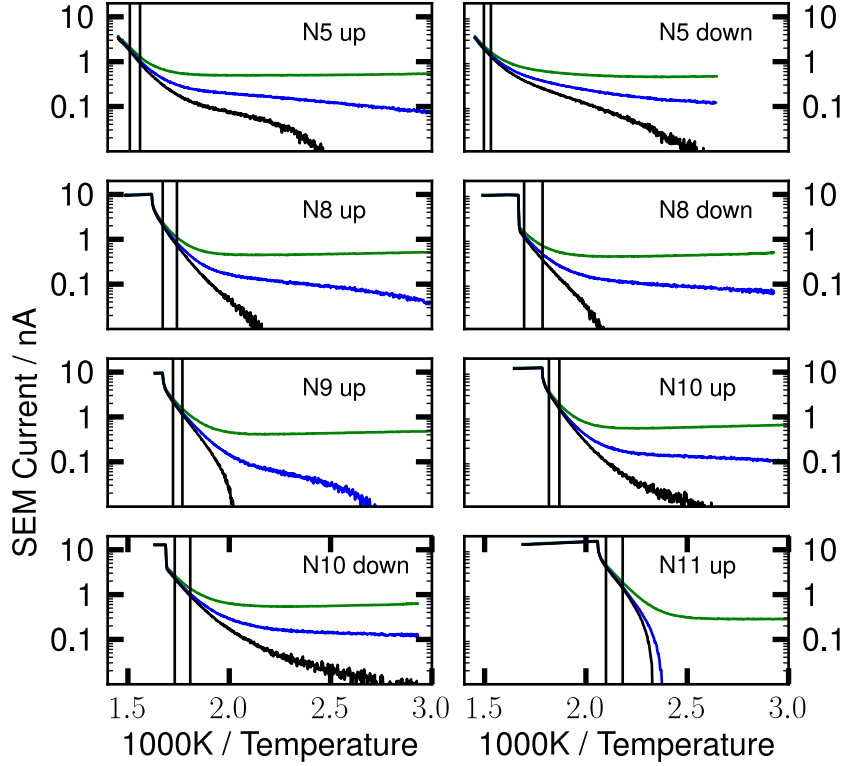


**Figure 6.6** – Background correction for all measured samples. The vertical black lines indicates the range used for the Arrhenius-fit.

at 140 min is zero, and thus the combined signal of the O<sub>2</sub> and CO should correspond to the nominal flow of  $6 \times 10^{14}$  molecules/s, since no other molecules are leaving the reactor. Reading off the figure tells us that the measured currents for O<sub>2</sub> and CO, respectively, are 69.4 nA and 25.5 nA. This means that as a first approximation we can estimate the combined sensitivity factor to be

$$S \approx \frac{(69.4 + 25.5) \text{ nA}}{6 \times 10^{14} \text{ molecules/s}} = \frac{1.6 \times 10^{-13} \text{ nA}}{\text{molecule/s}} = \frac{1.6 \times 10^{-22} \text{ C}}{\text{molecule}}$$

The value of  $S$  was estimated from sample N8, but as can be seen easily in figure 6.3, not all samples have the same flow and thus they cannot all have the nominal flow of  $6 \times 10^{14}$  molecules/s. However, since we have no easy way of measuring the absolute flow, for now we will simply have to define a sample, in this case N8, to have this flow. With this estimate of  $S$  we can now make a plot with approximate absolute numbers on both axis.

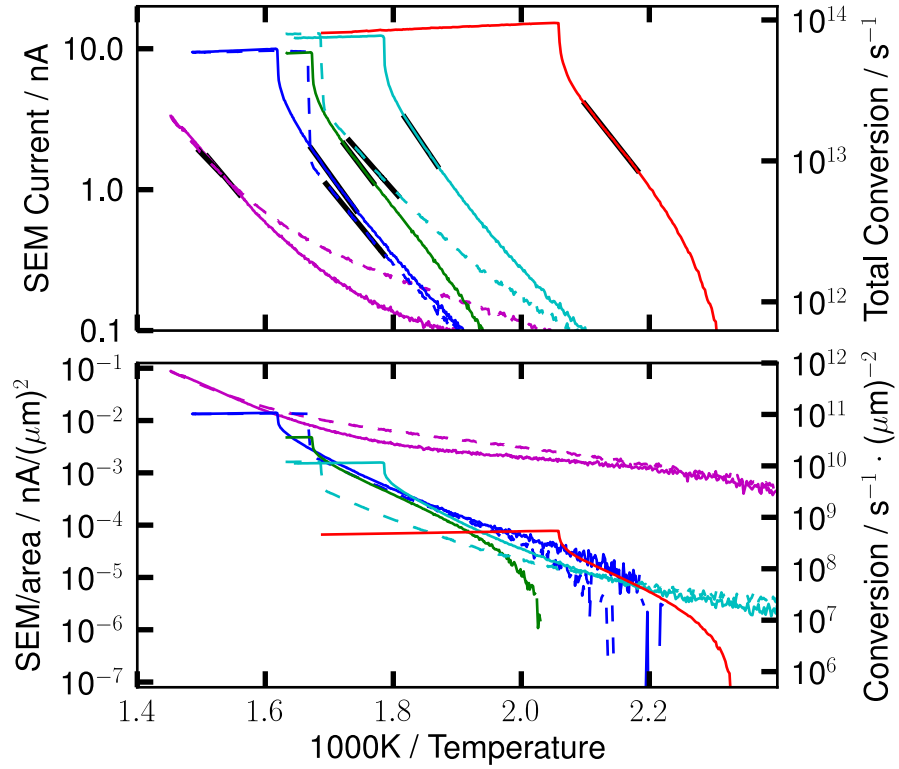


**Figure 6.7** – Arrhenius plot of all measured samples. Upper panel show the absolute numbers. Lower panels shows the result scaled to the sample area. Left axis shows the directly measured SEM current, right axis shows the current converted to molecules using the measured sensitivity factor.

### 6.3 Results

The result of the analysis is plotted in Figure 6.8. It is as always important to keep in mind which values are subject to which approximations. In this case the calculated turnover frequencies are subject to the rather uncertain estimate of a flow of  $6 \times 10^{14}$  molecules/s from reactor N8 as well as the assumption that the mass spectrometer has kept a constant sensitivity during the course of all measurements. However, the calculation of the activation energy is dependent only on the general linearity of the mass spectrometer and to a lesser degree to the quality of the background subtractions.

The extracted activation energies are all of the order of  $\sim 1.1 - 1.3$  eV which is consistent with the literature value for CO oxidation on Pt thin films[33]. No sign of a dependence of the activation energy with spot size is seen within the measured range and thus it must be expected that we can extended the measurements to even smaller spot sizes just by increasing the temperature.

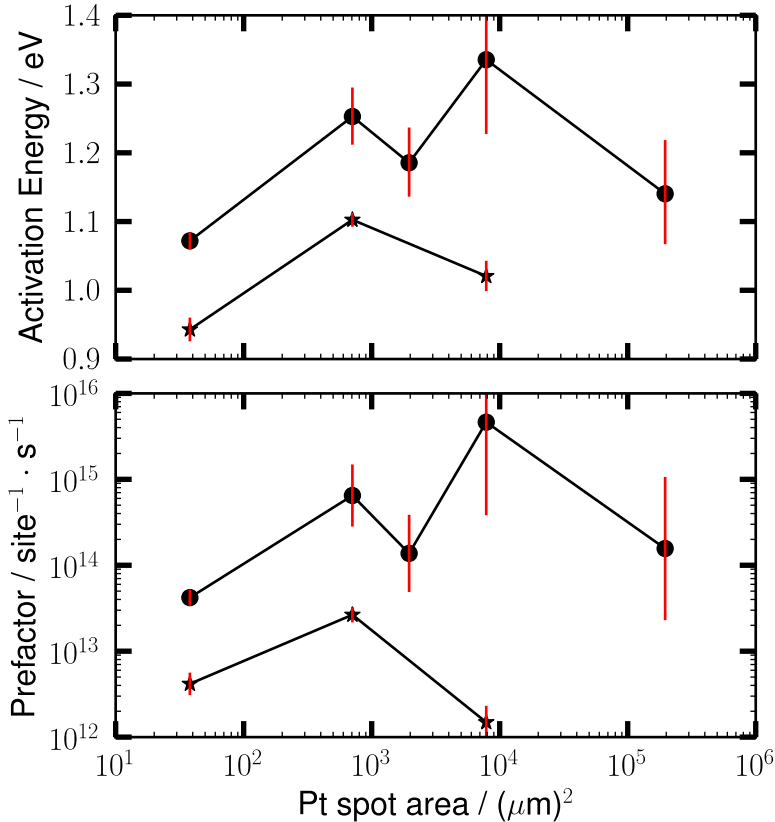


**Figure 6.8** – Extracted activation energies (top panel) and prefactors (lower panel). Circles represent a measurement on the rising temperature ramp, stars the falling temperature ramp. Error bars (in red) are roughly estimated by slightly extending the fitting region.

The density of surface sites on Platinum is approximately  $6.5 \times 10^6 \mu\text{m}^{-2}$  (as calculated from the tabulated Pt-Pt distance for a single crystal). From Figure 6.7 the highest measured conversion can be read to be  $\sim 7 \times 10^{11} \text{s}^{-1} \mu\text{m}^{-2}$  which thus corresponds to

$$TOF_{Max} = \frac{7 \times 10^{11} \text{s}^{-1} \mu\text{m}^{-2}}{6.5 \times 10^6 \text{site} \times \mu\text{m}^{-2}} \approx 10^5 \text{ site}^{-1} \text{s}^{-1}$$

however this is not necessarily the highest achievable turnover frequency, merely is it the highest we have so far been able to reach due to the temperature limits with the used heater design.

It is an interesting thought, that a single nanoparticle with a diameter of 5 nm exposes an area of approximately

$$A_{NP} \approx 4\pi \times \left(\frac{5}{2} \text{nm}\right)^2 = 78.5 \text{ nm}^2 \approx 8 \times 10^{-4} \mu\text{m}^2$$

which means that the so far smallest film measured has an area corresponding to

$$N = \frac{38}{8 \times 10^{-4}} = 47500 \text{ nanoparticles}$$

Even though this is still a large number, we are rapidly approaching the regime of measuring on a countable number of particles. Considering that we expect to be able to reach even higher turn over frequencies and that it is certainly not necessary to reach full conversion to perform measurements, we are really not too far away from the original goal of Center for Individual Nanoparticle Functionality, ie. to measure on a single nanoparticle.

## 6.4 Lessons to be learned

Besides the obviously interesting point in measuring how high the turn-over frequency can actually be, this results also put focus on the fact that extremely small amounts of catalyst can be responsible for much reactivity. In the case of the  $\mu$ -reactors this is important in at least two ways. First of all it means, that we must be extremely careful to avoid any kind of metal pollution in the reactor, especially platinum. This can be slightly more tricky than it sounds, since in the cleanroom, metal pollution is never far away, and we actually have seen examples of barium pollution in the reactors with any attempt to find the source being fruitless. Also, one should remember that we have the heater on the backside of the reactor, which is made of platinum. It is of crucial importance to be able to deposit this heater without even trace amount of metal finding its way to the other side of the reactor. This is ensured by e-beam evaporating the platinum through a shadow mask. Other ways of depositing the heaters also exists, but these techniques often involves various wet-chemistry steps which means that small amounts of unwanted platinum could find its way from the backside to the front side through the liquid phase.

The other important lesson to be learned is that one should be extremely careful when trying to apply in-situ methods. Even though in-situ methods is not easy to apply in a  $\mu$ -reactor, we are continuously considering our options in this field, since this would significantly increase the usefulness of the platform. However, even in the rather optimistic case, that we actually do succeed in finding methods that would provide in-situ information, we must always remember the fact that such small areas of the reactor might, at least in some cases, be responsible for all the conversion. This means that whatever technique is being applied might primarily sample areas of the sample that is not actually performing the conversion. A technique with low spatial resolution might be easy to get to measure on the converting part of catalyst, but the signal to noise ratio will be poor, potentially too low to see anything. A technique with better spatial resolution will give a much better signal to noise, but faces the very real risk of not seeing the relevant part of the sample at all.

# Chapter 7

## Analytic techniques

A major disadvantage of the  $\mu$ -reactor setup is the distinct lack of analytic techniques available to investigate the catalyst during measurements. In traditional reactors access to techniques such as XPS, AES or various infrared techniques gives extremely valuable insights into the state of the catalyst surface as well as sometimes even information about intermediate species on the surface. Such a luxury is not available on the  $\mu$ -reactor, the sealed nature of the reactor makes it extremely difficult to access the sample with classical techniques. Even postmortem analysis is difficult because no known way exist to open up an anodic bonding in a non-destructive way. During the project we have time and time again discussed the possibility of adding any kind of instrumentation that would reveal insight either in-situ during reaction or just means to investigate the surface before and after exposing it to reaction conditions. In this chapter, I will briefly discuss a number of techniques that has so far been discussed but not actually applied as well as some we have already tried.

### 7.1 Feasibility study

Several possible techniques has been proposed and some of them might actually be useful, some of the techniques we have discussed, but have not yet successfully applied, includes:

**Raman Spectroscopy** This would seem to be an obvious technique which in principle provides much useful information. However, after several discussions with the Raman experts at the department, we have come to the conclusion, that the technique is not sensitive enough to help us. So-called Surface Enhanced Raman Spectroscopy might be able to help, but also here several problems exists that will seriously complicate the application of this technique.

**FT-IR and other infrared techniques** This seems to be a fairly realistic option since FT-IR equipment is actually available at CINF. However, sensitivity is expected to be a major problem, and as an extra complication, the sample will need to be fully transparent. Actually, such a transparent reactor has been developed to be used in photo catalytic applications (a major area of research at CINF but not part of my work), but since this reactor consists almost exclusively of various types of glass, heat conduction is terrible and thus we would need to find a completely new way of heating the sample, possibly by emerging the sample

in a stream of hot air. However, mounting all this inside an FT-IR instrument does seem to be quite a challenge.

**Plasmonic structures** A few years ago, the group of Bengt Kasemo at Chalmers University published a novel in-situ technique utilizing a shift in the plasmon frequency of metal structures to measure various parameters in a system[34]. This technique is interesting because it is highly sensitive and in principle it is fairly easy to introduce in the  $\mu$ -reactors. The principle is that one before bonding the reactor deposits a number of small gold-disks on the lid of the reactor. These gold discs can be covered by enough  $\text{SiO}_2$  that there will be no risk of contaminating the reactor with the gold. By monitoring the plasmon frequency of the disks, one is able to measure various parameters such as temperature and gas-composition changes. Unfortunately, only a single parameter, the plasmon frequency, is measured and since it depends on many properties of both the catalyst, the gas phase and the reactor itself, it can be quite difficult to interpret the result. In corporation with the developers of the system, we have done several attempts to apply the technique in the  $\mu$ -reactors, but so far the project has failed due to problems with resonance between reflections from the bottom of the reactor and from the plasmonic structures. We, however, still have hopes that this technique can be applied in some form.

## 7.2 Postmortem analysis

It would seem obvious that the easiest way of gaining insight into the surface of the catalyst is to simply analyze the surface after it has been exposed to the relevant experiments. This will typically mean that the reactor is somehow opened up after the experiment. This is not as easy as it may sound, since the anodic bonding is extremely strong and the silicon reactor itself is very fragile. Simply removing the lid is by now considered to be impossible, there is simply no way of cleaving off the lid from the sample. Earlier it has been tried to simply break the sample using some sort of mechanical means to crack the sample into a hopefully limited amount of pieces. Some of these pieces will possibly be entirely within the reactor area and therefore the lid will come off rather easily because it is only bonded to a few pillars. This method works and has been used to open samples to do XPS, but it is a primitive and dangerous technique that might easily completely break the sample with no useful pieces left. This is particularly unfortunate since a sample interesting enough to perform this operation, would most likely be rather valuable.

For this reason a more reliable method is wanted. We went through several attempts before coming up with a working solution. Among the failed experiments was attempts to weaken the reactor with a diamond saw and then pressurizing the reactor to 2.5 bar of over pressure hoping the pressure would push out a piece of the reactor. This did not work, even the weakened reactor showed no sign of cracking at 2.5 bar. Etching the lid away with HF has also been considered but this is a really bad solution both because of the long list of safety concerns with HF and also because it is a very dirty way of opening the reactor. HF will inevitably leak into the reactor volume and contaminate the sample.

The answer to the problem was invented by our clean room wizard Thomas Pedersen and turned out to be to cut four lines with a diamond saw in a way that leaves the largest possible square of the reactor. If the cut is approximately 90% of the total depth of the reactor, it can quite easily be opened by hand once it is ready to be mounted in what ever instrument that should be used for the examination. This technique is demonstrated in Figure 7.1 where we

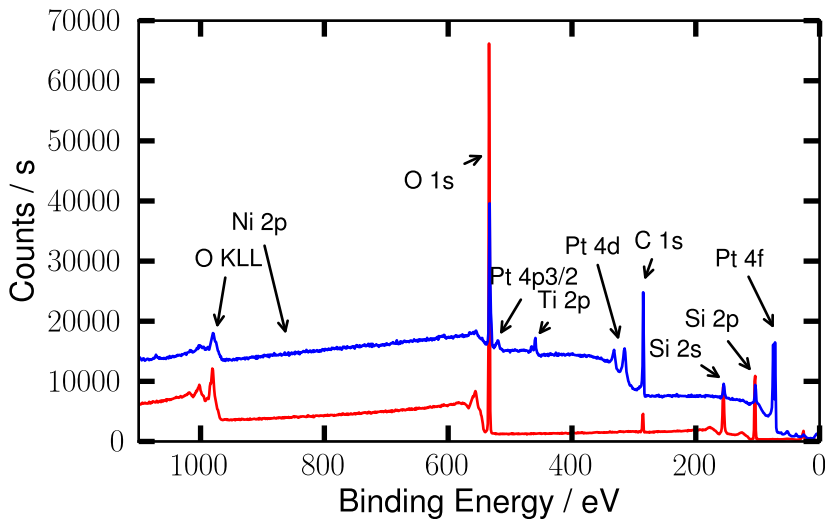


**Figure 7.1** – XPS spectrum of a sample exposed to very large amounts of CO at both high and low temperature. It is evident that no significant amount of nickel carbonyl has been deposited on the surface. The upper spectrum is focused on a Pt spot, the lower spectrum is focused on an empty part of the reactor.

have taken a sample exposed to very large amounts of CO to check if the sample is polluted by nickel carbonyl,  $\text{Ni}(\text{CO})_4$ , which is a known pollutant originating the CO reacting with Ni from the steel tubing. As can be seen from the Figure, we do not have a problem with nickel carbonyl pollution.

Of course postmortem analysis is not always a useful solution. The sample is irreversibly destroyed and there is no chance of ever mounting it in the setup again, and the method will therefore only be able to probe the final state of the sample, no intermediate situations can be measured unless one prepares a number of identical samples and stop them at various intermediate steps of the measurement. Also, the surface will necessarily be exposed to air to be cut out with the saw and to be mounted in a chamber equipped with XPS. This of course somewhat limits the scope of this kind of analysis since many interesting features of the sample will be long gone before the sample reaches the analytic tool.

### 7.3 Non-bonded samples

To solve the problem of the destructive process of the diamond saw, we tried another solution to be able to do XPS on our samples. Since one of our  $\mu$ -reactor setups operates the entire sample in an evacuated chamber, it is in principle possible to run experiments on heavily leaking samples without atmospheric air entering the sample and without risk of potentially poisonous gasses (in our setup the most poisonous gas is typically CO) escaping to the surroundings. This means that we can run experiments on samples that has not been bonded, simply by mechanically clamping the lid to the sample and mount it in the setup. This of course has a major disadvantage in the fact, that the reactor volume will leak heavily into the containment volume, and thus we loose the property that all reacting gas will enter the QMS

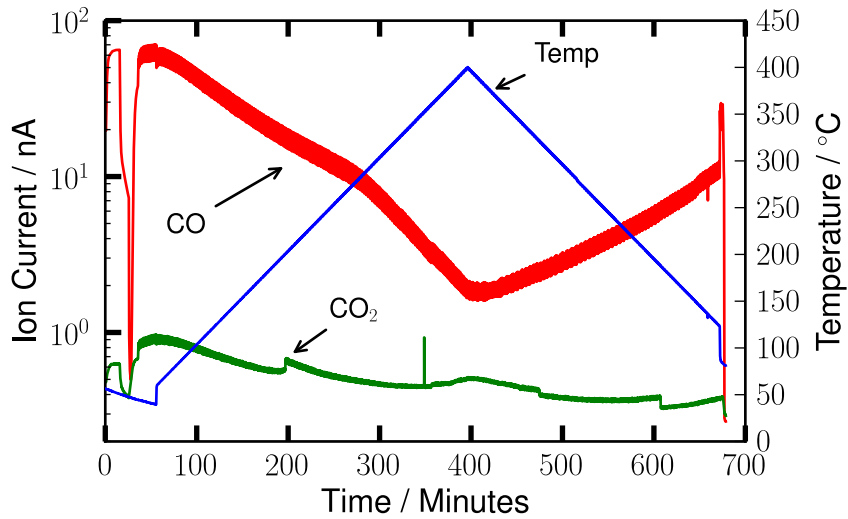


**Figure 7.2** – CO oxidation on a non-bonded sample. The lid is simply clamped to the sample. All qualitative features of CO oxidation on Pt can be seen despite the low sensitivity. The large noise level in this particular measurement was due to a problem with the electric connection to the flow controller, not a feature of the non-bonded sample.

and hence the sensitivity is lowered significantly compared to a properly bonded sample. However, the method has one great advantage in the fact, that we can now non-destructively run *ex-situ* investigations, typically XPS, re-mount the sample and run it again. The loss in sensitivity is not of great concern since the measurement would then be repeated on a bonded sample that is as identical as possible to the non-bonded sample to get mass spectrometry of much higher quality. The data from the non-bonded sample thus only needs be good enough that it can be documented that the sample that was taken out for *ex-situ* studies has experienced conditions identical to the bonded sample.

A proof-of-concept of this technique is shown in Figure 7.2 which shows CO oxidation on a Pt thin film. It is easy to see that the sample do reach light-off even though the poor sensitivity means that the signal is not nearly as good as for a properly bonded sample.

## 7.4 Optical methods

As discussed in chapter 5 we would very much like to try to look for a thermal sign of where the reactivity is taking place in the reactor. Since small parts of the sample could potentially become very hot, we have a vague hope, that we might be able to see this using a standard CCD camera. If this is possible, we open up the possibility of using classical optical methods which have a much higher resolution than thermographic cameras. We have done several attempts at this and have also successfully imaged the heating element, but so far we have not been able to find signs of local heating of the catalyst, however, we have not given up yet. Besides the rather ambitious project of imaging the temperature profile, optical methods can also be highly useful for more ordinary tasks. Many samples change color during oxidation or reduction cycles which could be useful to image while the experiment is running. Also, some

samples undergo macroscopic morphology changes during certain reactions, for example we have seen several continuous Pd thin films crack to pieces during methanation reactions, also this could be interesting to measure in a time resolved way.

## 7.5 Time-Of-Flight Mass Spectrometry

Another way of extracting other kinds of information from the  $\mu$ -reactors is to use a different detection technique besides the usual Quadropole Mass Spectrometer. We have tried this by attaching a Time Of Flight Mass Spectrometer. This has been a highly successful project and for this reason, this subject has been moved to its own chapter, the story of the TOF can thus be found in chapter 8.



# Chapter 8

# Time Of Flight Mass Spectrometry

As mentioned in chapter 7, the attachment of a Time Of Flight Mass Spectrometer to the new  $\mu$ -reactor setup, has turned out to be an extraordinary success. Since this has proven to be such a useful addition to the setup, I have chosen to dedicate a chapter to this technique.

## 8.1 Instrumentation

The instrument was bought as an assembly kit from Jordan TOF Products [35] and was put together here in the lab. The frame and the pumps for the system was scavenged from an old molecular beam setup that had been idling in the lab for some years and thus the complete setup is a wonderful mixture of many different kind of flanges and pumps which happened to be available, as can be seen in Figure 8.1 . The result of the scavenging turned out to be a 120 l/s ion pump, used to differentially pump the flight tube, and a 400 l/s ion pump and a 450 l/s turbo pump both used to pump the source region. At this point in time, we have not tried to bake the chamber and this means we have a rather poor background pressure of  $\sim 10^{-9}$  mbar in both the source region and flight tube. However, it will eventually make sense to bake the chamber since the background pressure contributes with dead-counts on the detector and thus degrades the signal to noise ratio of the instrument. All parts of the setup are fully UHV compatible and since we have quite good pumping capacity, it is to be expected that we can get well below  $\sim 10^{-10}$  mbar once the chamber is properly baked.

### 8.1.1 Vacuum components

The instrument consists of three main regions. The source and acceleration region, the field free drift region (called the flight tube), and the reflectron. Detectors are positioned both at the end of the flight tube (behind the reflectron) and at the entrance of the flight tube, which is where ions are detected when the reflectron is in use.

The source region (seen in Figure 8.2) is where the ions enter the instrument and where they are initially accelerated. The ions enter from the top of the drawing, that is, orthogonal to the flight direction. On the way into the instrument, ions will pass through a number of einzel lenses to focus them as well as possible. At a given point in time, a high voltage

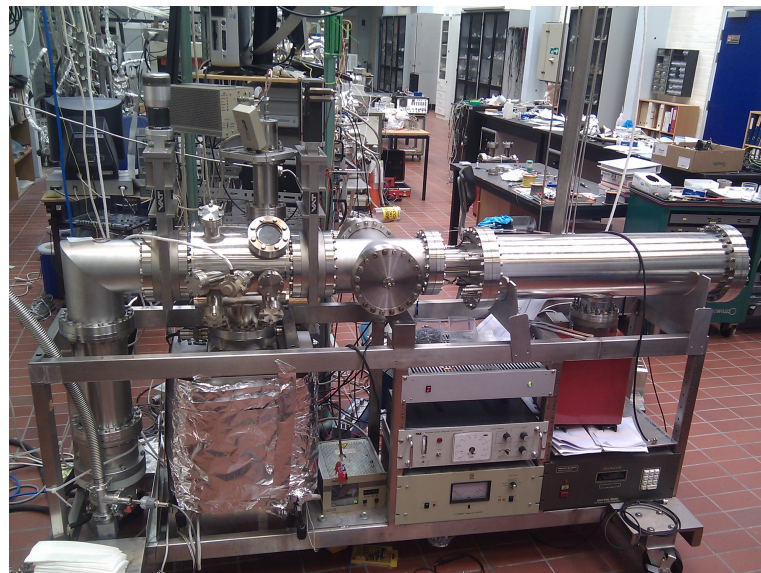


**Figure 8.1** – The Time-Of-Flight instrument in all its glory. The electronics rack is barely visible in the background.

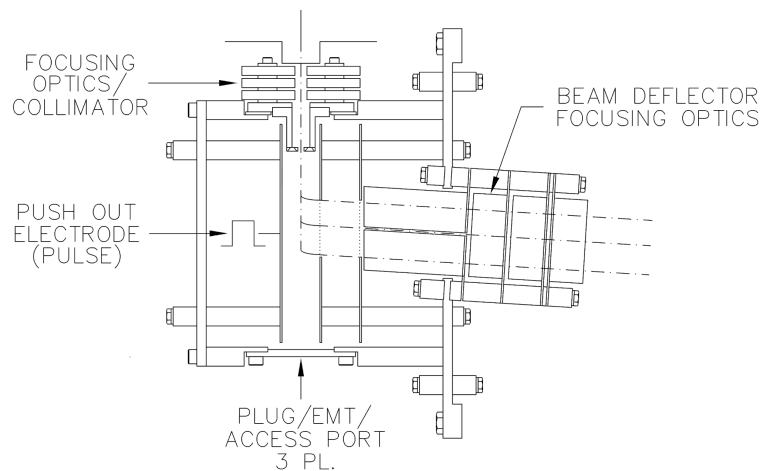


**Figure 8.2** – Schematic of the source region of the Time-Of-Flight instrument. Drawing by Jordan Instruments[35].

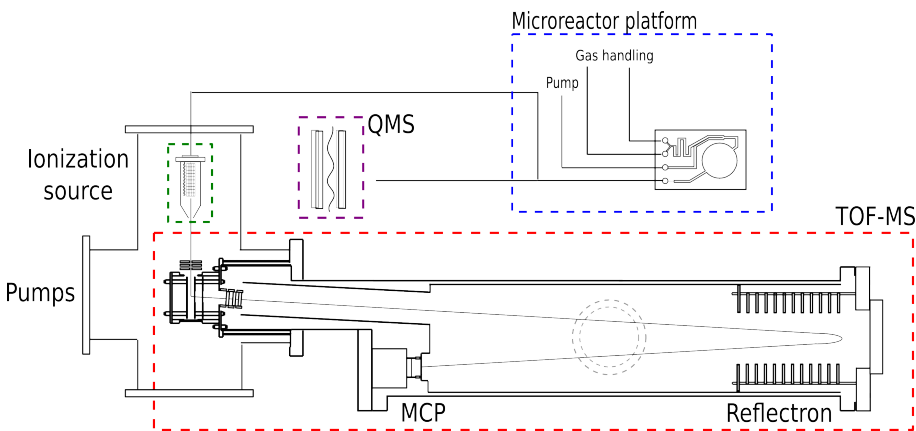


**Figure 8.3** – Schematic of the Time-Of-Flight instrument along with the connections to the  $\mu$ -reactor and the QMS. Drawing by Thomas Andersen.

pulse on the acceleration plate will accelerate the ions away from the source region and into the acceleration region where the ions are further accelerated up to the final drift velocity. Typical values for the initial pulse is  $\sim 400$  V and typical drift energy is on the order of  $\sim 2000$  V. Of course it is critical that the rise time of the acceleration pulse is as short as possible, in our case we use a DEI PVX-410 Pulser with a rise time less than 25 ns. From the acceleration region, the ions enter another set of focusing lenses as well as the deflector which is designed to compensate for the initial velocity orthogonal to the flight direction and will ideally ensure that the ions proceed into the flight tube in an angle of  $7^\circ$ .

After entering the flight tube, the ions will float freely for almost a meter (37.5 inches to be exact) before they enter the reflectron. The flight tube consists of two concentric tubes, the outside tube is the leak-tight barrier to atmosphere that ensures that we can hold a vacuum in the chamber. However, since this tube is exposed to the outside world, it would be most inconvenient if this tube was held at -2000 V, it would constitute a significant danger for operators as well as complicate the connection to other electronics significantly. This is where the second concentric tube, the so-called 'liner' enters the equation. This tube has a slightly smaller diameter than the outside tube and is mounted on small ceramic feet that rests on the outside tube and ensures that the liner is electrically floating compared to the main chamber. The liner is perforated at the position of the flight tube pump to ensure decent pumping of the liner.

The TOF can be operated in two ways, linear mode or reflectron mode. In linear mode all voltages on the reflectron is set to liner voltage. In this case, ions will continue straight through the reflectron and hit a detector positioned in the end of the flight tube. This is the simplest mode of operation but it also performs far worse than the reflectron mode, partly because of the longer flight distance with the reflectron, but more importantly because of the focusing effect of the reflectron, which we will come back to in section 8.3.

In the reflectron mode, suitable voltages are applied on grids in each end of the reflectron to ensure that ions are stopped and re-accelerated in the opposite direction where they will again enter the flight tube and because of the  $7^\circ$  tilt of the ions, they will hit the second detector and not end up in the acceleration region once more.

Both detectors are Multi Channel Plates which is a rather sophisticated kind of electron

multiplier. The main detector has a maximum bias voltage of -5 kV, an area of 12.6 cm<sup>2</sup> and it is completely flat across the entire detection area[36]. This very large and flat detector area makes the detector very tolerant for ions having slightly different initial positions in the plane orthogonal to the flight direction, since the various ions would make almost identical trajectories only slightly translated. The MCP consists of a large number, on the order of  $\sim 10^7$ , of small channels coated with a low work function material. The MCP is heavily biased between the front side and the back side, creating a steep voltage gradient across the device. When ions hit the surface of the MCP, it will release a number of electrons which due to the high voltage gradient will accelerate further into the channel. Since each channel is very shallow, the electrons will only travel a short distance before they again hit the surface and release even more electrons. In this way a single ion will be multiplied into a significant number of electrons, how many is heavily dependent on the voltage across the device. In our case, we have mounted a rather cheap MCP for the linear detection and a substantially better one, a so-called Z-gap detector, with a maximum bias of 5 kV for the reflectron detection. Interestingly, the detector is what ultimately sets the limit for the highest mass that can be detected. It turns out that for heavy ions the detection efficiency drops significantly with mass[37] because the energy of the particle is distributed on a larger and larger area which increases the risk that the initial impact of the particle will not release a single electron that can be further multiplied. Since we are, among other things, also interested in measuring on metal clusters, a high mass limit is essential. The current Z-gap detector has a nominal maximal detectable mass of 5000 amu, and furthermore, the chamber is equipped with feed-troughs for mounting a 15 kV detector if necessary. This should bring detection limit up to approximately  $10^6$  amu.

### 8.1.2 Electronics and data acquisition

Looking at the wonderful amounts of stainless steel in Figure 8.1, one could easily get the idea that all the interesting stuff happens inside the vacuum chamber. However, nothing could be more wrong, in reality much of the magic of the instrument takes place outside of the chamber in the rather substantial amount of electronics that drives the instrument. First of all, it turns out that one needs quite a lot of power supplies, not only do we need high voltages for the liner potential,  $V_{liner}$ , also the focus lens,  $V_{focus}$ , the deflection plate,  $V_{def}$ , the acceleration plate,  $V_{pulse}$ , two reflectron voltages,  $V_{R1}$  and  $V_{R2}$  as well as the MCP detector,  $V_D$  needs power supplies, all in the range of -4000 V – +4000 V. Additionally the four entrance lenses need a total of five different voltages (one lens also acts as a deflector and thus is in two parts). For one thing this means that we need quite a lot of power supplies, but this is a minor problem, most of the voltages can be supplied by two multi-output supplies. However, it is also evident that optimizing the system is not especially fun, since the parameter space is extremely large. Luckily it turns out that the entrance lenses can be optimized almost independently of the rest of the system, reducing the problem from an 11-dimensional problem to a five-dimensional problem and a six-dimensional problem. This is, however, still quite a lot and the initial tuning, just to get a measurable signal, proved to be somewhat of a challenge. In this situation, it is highly recommended to operate the instrument in linear mode since this takes out another dimension of the initial optimization problem. The acceleration pulse is generated in a two step process where a low voltage high-quality signal generator creates a continuous pulse train of square waves, typically we use a peak-width of 1  $\mu$ s and a repetition rate of 400 Hz. This low voltage signal is tee'd into two BNC cables, one connected to the high voltage pulser, and one to the trigger of the computer digitizer, which records the signal from the MCP. The digitizer is an Agilent DP214 bought

very cheaply on eBay. It features a maximum sampling frequency of 2 GHz which turns out to be fully sufficient to resolve the pulses from the MCP. Unfortunately, the digitizer only has 8 bit dynamic range, which is somewhat less than one would want, since this constrains the maximum dynamic range of the entire instrument. All data acquisition is computer interfaced through home-made software. In this way we are able to activate a TOF-scan remotely, which make it possible to synchronize the TOF with the rest of the  $\mu$ -reactor setup.

### 8.1.3 Ionization

The parts bought from Jordan of course constitutes the actual analytic instruments and is what is known as a Orthogonal Acceleration TOF which means that the ions to be measured enters the acceleration region orthogonal to the direction of flight. This is especially well suited to measure on externally generated ions, which is unfortunately not what we have when measuring on the  $\mu$ -reactors; the output from the capillary is obviously not ionized. However, the reason for choosing this type of instrument is, that we originally expected to use the TOF as a characterization tool for the two cluster sources at the department, and these instruments do have an ionized output. This little experimental detail meant, that we had to build our own ionization source to be able to use the instrument at all.

Optimally all ions will enter the acceleration region with very low energy orthogonal to the flight direction, zero energy in the flight direction and perfectly centered between the acceleration plate and the grounded grid. Of course in reality the ions will not have ideal position and energy, which will ultimately set the limit of the resolution of the instrument.

Our current way of ionization is both very simple, very cheap and very much sub-optimal. Originally we only wanted to make a very primitive and cheap ionization source to able to test the instrument by letting in gas directly from a leak valve, just to be able to tune and optimize the instrument before mounting it on the cluster source. For this purpose we realized that the classic UHV Bayard-Alpert ion gauge[31] might be a simple solution. After all, the gauge works by ionizing gas, however in the normal operation mode, no ions will escape the gauge, rather they will hit the collector and leave the gauge as neutral molecules. However, by removing the lid of the gauge and short-circuiting the collector to the grid, the ions will now be able to escape the gauge through the top where the lid is now missing. Using this configuration approximately half of the ions are expected to leave the ionization gauge[38] (the other half will neutralize by collisions with the grid). A current of approximately 3 A is run through the filament resulting in an emission current somewhere between 1 and 10 mA, in our current configuration we are not actively stabilizing the emission current, and we are typically not measuring it either. Fixing this is very high on the to-do list since the emission current is most likely not especially stable which of course is very bad for the self-consistency of the measurements. The grid is biased approximately 40 V positive compared to the filament to accelerate electrons emitted from the filament towards the grid. This voltage is very much a compromise, since for optimal ionization we would like much higher energies. The ionization cross section for most relevant gas species will peak between 100 and 200 eV[39]. Typically ionization gauges operate in the range of 120–150 V for exactly this reason[40]. However, high ion energy is exactly the opposite of what we want for an ion source for the TOF, where we would optimally want mono-energetic ions of approximately 5 eV. It is evident that the difference between optimal ionization and optimal performance of the TOF is very large and the fact that it can be brought to work at all is actually quite unintuitive. A possible solution to this rather unpleasant compromise could be to mount a collisional damper which will cool down ions to thermal energies.

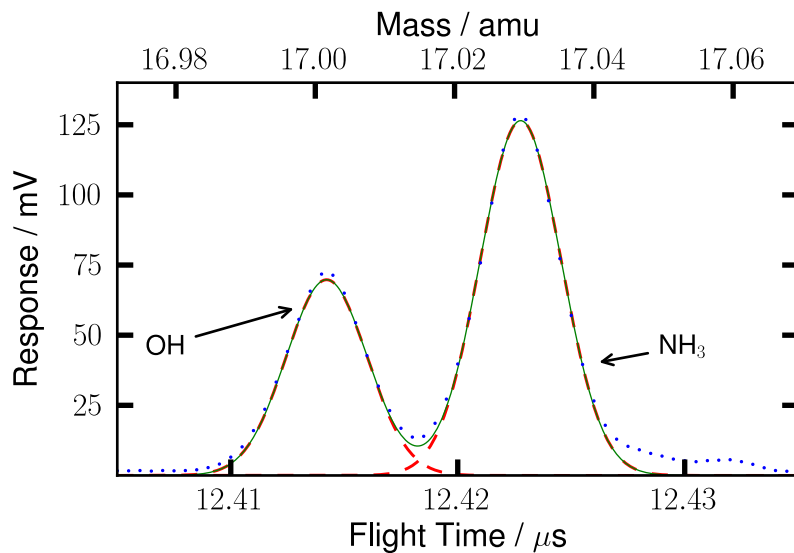


**Figure 8.4** – Example of two Gaussian fits to a measured double peak in the TOF-spectrum. It is evident that the two peaks can be completely resolved despite the small mass difference of 23.8 mili-amu.

The entire ionization structure is placed in a flange with a small orifice which is differentially pumped. Large amounts of gas can hence be dosed locally around the ion source while still maintaining a low pressure in the source region of the TOF-MS. The small orifice is essential in the setup to avoid high pressure in the acceleration region and thus also the drift tube which would cause an increase in dead counts on the MCP thus decreasing the signal-to-noise ratio of the recorded signal.

## 8.2 Data output

Unfortunately, we cannot judge instruments only on the coolness factor, they also need to deliver actual results to merit a position in the lab. Fortunately, the performance of the TOF is very good, the resolution is much better than a traditional QMS. The manufacturer of our device claims resolutions of up to  $m/\Delta m \approx 4000$  is possible under optimal conditions. Unfortunately, we are working far from optimal conditions, primarily due to our very primitive ion source which produces too few ions of too high energy with a too large energy spread. All this considered we are actually doing quite well and have reached resolutions better than  $m/\Delta m \approx 2000$  which is enough to separate many interesting ions which would normally be overlapping on traditional mass spectrometers. A primary example of this would be ammonia,  $\text{NH}_3$  and hydroxide,  $\text{OH}$ , which are both at 17 amu. However due to the different mass defects of the involved atoms, the exact mass of  $\text{NH}_3$  is 17.02655 amu and of  $\text{OH}$  17.00274 amu, leaving a mass difference of 23.8 mili-amu. This is a small difference, but as shown on Figure 8.4 it is enough to separate the two components into two distinct peaks that can be individually fitted and quantified.

The high resolution also completely eliminates any risk of spillover from one mass to another, a problem often seen in classic mass spectrometers, when a small mass is immediately next

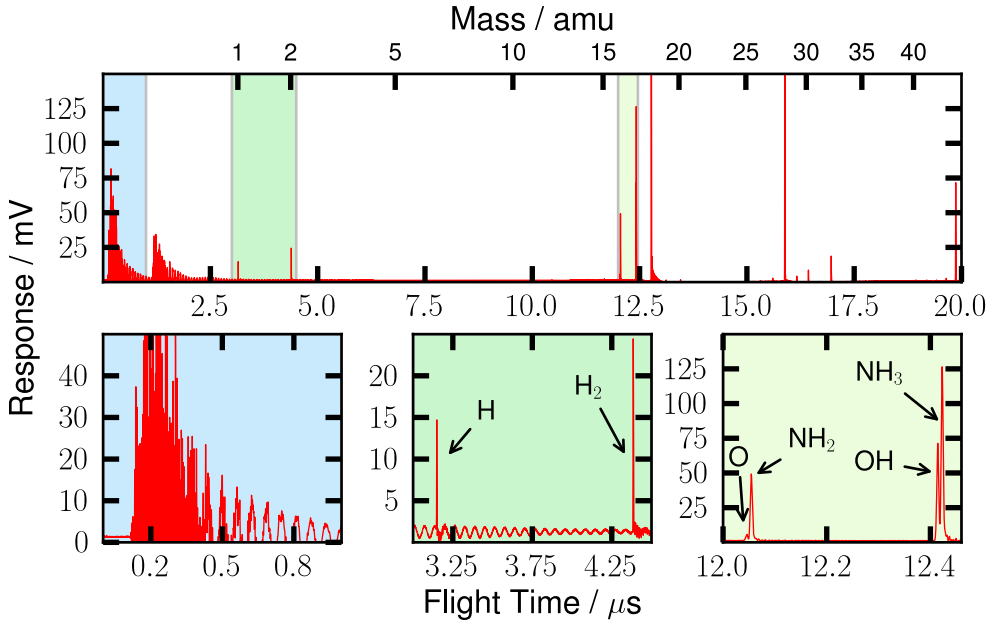


**Figure 8.5** – Example of raw data from an ammonia oxidation experiment measured with the TOF. The top panel shows the entire spectrum. Lower left panel shows the initial noise spike, which is always present in the spectra. Lower center panel shows the separation between 1 amu and 2 amu. Lower right panel shows that we are able to separate  $\text{NH}_3$  from  $\text{OH}$  and  $\text{NH}_2$  from  $\text{O}$ .

to a large mass. An example of a spectrum is shown in Figure 8.5 from which it is evident that the separation between all compounds separated by at least 1 amu is extremely large. Quantification of the various gas species is done by fitting the detector response for the corresponding peak to a Gaussian fit of the form

$$R = k \times e^{-(t-t_{center})^2/\sigma}$$

This type of function have a very convenient known solution for the integrated value:

$$\int_{-\infty}^{\infty} R dt = k \times \sqrt{\sigma} \times \sqrt{\pi}$$

In this way it is possible to deconvolute even partially overlapping peaks by fitting each peak and calculate the integrated responses separately.

### 8.3 Numerical model

Since the TOF-MS only measures flight time and not the actual mass of the measured molecules or atoms it is necessary to determine the relationship between flight time and mass. This can be done by recognizing known patterns in a mass spectrum, this could be

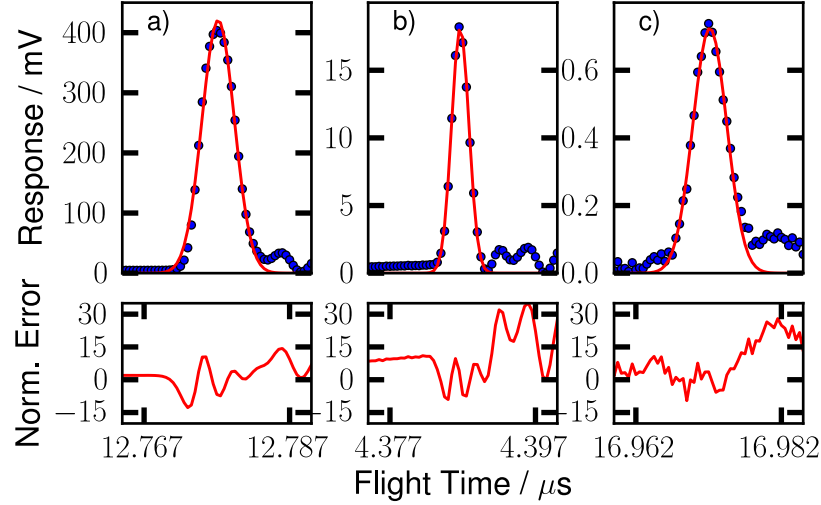


**Figure 8.6** – Gaussian fits (red solid line) to three different mass to charge ratios (blue points) from the same mass spectrum. In panels a), b) and c) the H<sub>2</sub>O (peak area: 2.35 mV·μs), H<sub>2</sub> (peak area:  $5.43 \times 10^{-2}$  mV·μs) and O<sub>2</sub> (peak area:  $4.24 \times 10^{-3}$  mV·μs) signals are shown, respectively. At the bottom panel the error normalized by peak area for each fit shows that the relative fit error is more or less independent of the total peak area

water at mass 18, CO at mass 28 and CO<sub>2</sub> at mass 44, and then use the measured flight times of these ‘known’ masses to fit an expression for the flight time as a function of mass. This approach is in some cases adequate but does have the significant drawback that several peaks of well known masses must be present in the spectrum which is not always the case. To determine the relationship between mass and flight time in another way, we have made a numeric model of the mass spectrometer which calculates the flight time based only on the voltages for the pulser,  $V_P$ , liner,  $V_L$ , and reflectron,  $V_{R1}$  and  $V_{R2}$ . The model is implemented as a very simple 1D iterative solution of the equation of motion of an ion initially positioned at a given position in the acceleration region. All instrument dimensions are based on the CAD-drawings as supplied by Jordan Instruments. A single free parameter, in the form of a correction to the length of the flight tube is allowed to be fitted to minimize systematic error. This free parameter turns out to be as small as 4.2 mm which actually fits rather well with the added length from the copper gaskets not included in the CAD-drawings.

Typically, the model is used together with the experimental determination of a single mass since this will help fix the unknown delays originating from the measurement trigger, rise time of the high-voltage pulse at the repeller plate and cable delays.

As seen in Figure 8.7 the performance of the model is good despite its simplicity. A total error in flight time estimation of  $\sim 10$  ns corresponding to  $\sim 50$  milli-amu at 70 amu is found. The model is written in Python and can be acquired as open source software at GitHub [41].

### 8.3.1 Simulation of the reflectron

An interesting side effect of the model is that besides predicting the expected flight time for a given particle, it will also plot the trajectory of an ion on its way through the flight

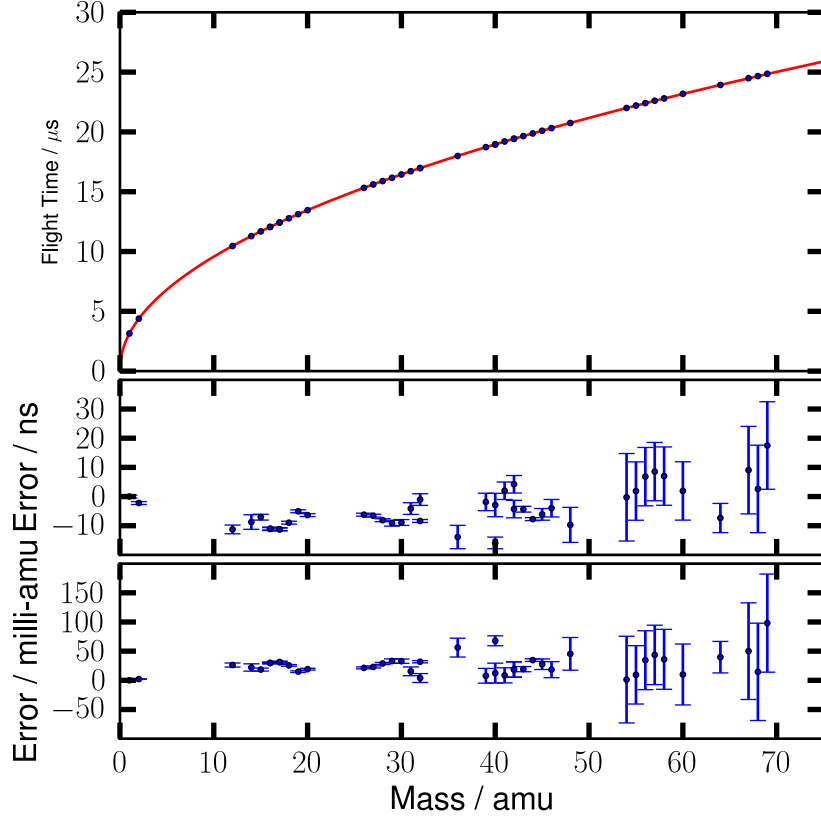


**Figure 8.7** – Plot of the model error as a function of mass.

tube. This means that it can be used to illustrate various concepts of the instrument. In Figure 8.8 it is illustrated how the reflectron improves the resolution of the Time Of Flight instrument. The point is, that in the real world, ions are not ideally positioned in the center of the acceleration region, some ions will be very close to the acceleration plate and some will be close to the ground grid. Ions starting exactly at the center will eventually reach a drift energy of  $E_{drift} = q(V_L + V_P/2)$ , ions initially closer to the acceleration plate will be faster, ions closer to the ground grid will be slower. This spread in energy inherently limits the resolution of a linear Time Of Flight instrument. However, as can be seen in Figure 8.8, if the voltages on the reflectron is chosen correctly, the reflectron will act as a focusing lens where the faster ions will dig deeper into the reflectron than the slower ions and thus compensate for the increased speed. The task for the constructor of the instrument is now to position the MCP in the focus point of the reflectron, which is exactly the case in our instrument.

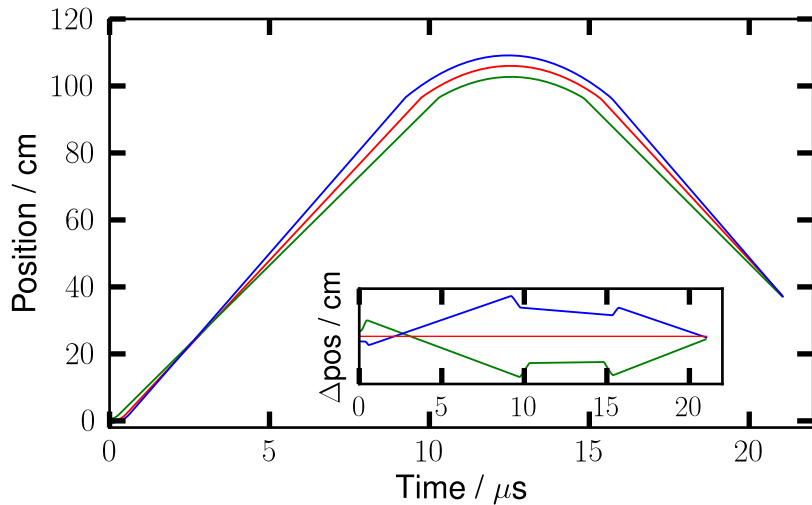


**Figure 8.8** – Trajectory plots of three different ions each with different initial position in the acceleration region. Insert shows the relevative position compared to ions starting from the center of the acceleration region.

## 8.4 Results

Since the TOF was not originally constructed for the  $\mu$ -reactor system, we did not have a long list of experiments to perform with this new piece of equipment. Rather the situation was the opposite, suddenly we had access to an unexpected device and we had to think of relevant applications for it. Rather soon we came up with two applications, benzene hydrogenation and ammonia oxidation. The benzene hydrogenation is in a very early state and the results presented here are highly preliminary. On the ammonia oxidation we have quite a lot of results and this will be thoroughly covered in the masters thesis of Mathias Kjærgaard Christensen[42], here I will just show a few selected results demonstrating the advantages of time-of-flight mass spectrometry for this reaction.

### 8.4.1 Benzene Hydrogenation

For a simple vacuum physicist, benzene is a frightening compound. Just the fact that it contains no less than 12 atoms ( $C_6H_6$ ) is certainly enough to turn a typical nice and clean mass-spectrum into a forest of peaks on a number of very non-typical masses. The number of ways for benzene to crack on a filament is large[43], and adding isotopic effects on top of this does not help the situation. The total mass of 78 amu is also a complication in itself. Even though most mass spectrometers are able to operate up to at least 100 amu, the sensitivity is typically both poor and not especially well known at masses much above 50 amu. The TOF will not solve all these problems, the cracking pattern is still complicated, but at least any sign of problems with the mass range is completely eliminated. Also the very high resolution is a great help since it eliminates cross talk between adjacent masses which can easily become a problem in a QMS, especially when the number of peaks in the mass spectrum is as high as in the case of benzene.

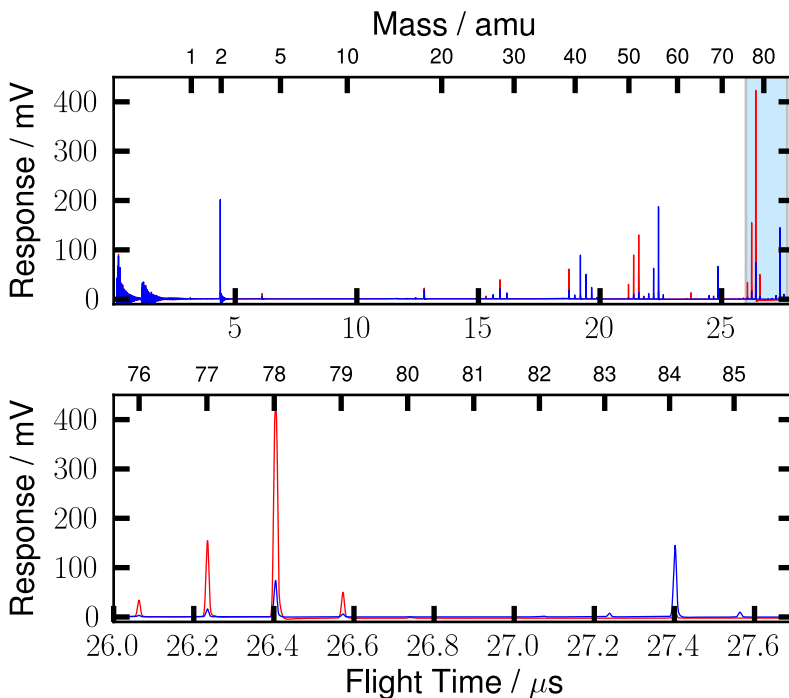


**Figure 8.9** – Benzene hydrogenation. Red spectrum is pure benzene. Blue spectrum is for a benzene/hydrogen mixture. Upper panel shows complete spectrums and lower panel show a zoom of the region where the hydrogenation process is visible.

The reason we are interested in measuring on this system is because changes in selectivity towards cyclohexane,  $C_6H_{12}$ , and cyclohexene,  $C_6H_{10}$ , has been shown to be dependent on if the reaction takes place on cubic or cuboctahedral nanoparticles[44]. Since correlations between structure and reactivity are always of interest in our group, we chose this as an interesting system for application of the TOF.

In Figure 8.9 the result of the very first (and so far only...) benzene hydrogenation experiment is shown. It turned out, that our Pt catalyst, in this case a thin film, was able to fully hydrogenate the Benzene into cyclohexane even at room temperature. The next logical step from here would of course be to cool the sample enough to bring down the conversion. From there the temperature can be raised in a controlled way and the activation energy and selectivity can be measured. However, due to time constraints when we performed this experiment for the first time, we chose to simply remove the hydrogen from the mixture which of course is also an efficient way of stopping the reaction. In this way we are able to get a simulated result of the cold sample with no activity. The next step from here will of course be to do a proper size dependence study, and hopefully find a size dependence of the selectivity.

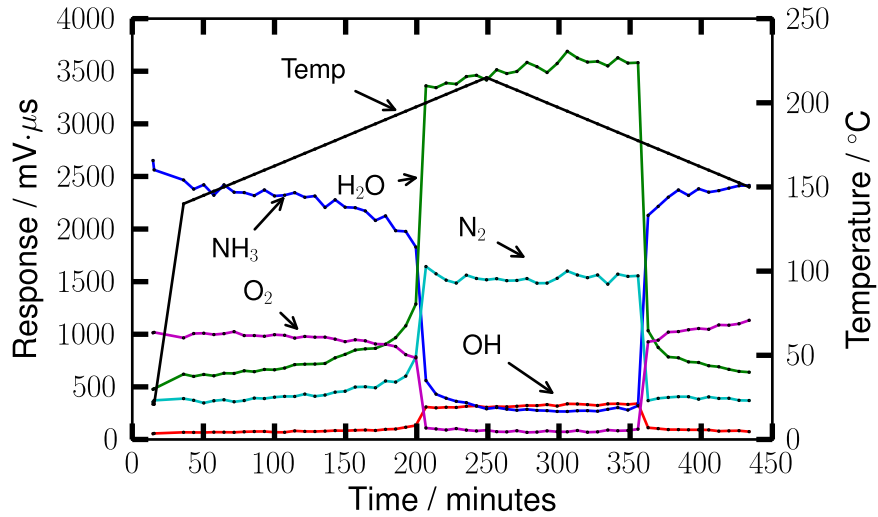


**Figure 8.10** – Time-of-flight mass spectrometry of ammonia oxidation on a Pt thin film. Notice that we are able to show the anti-correlation between OH and NH<sub>3</sub>.

#### 8.4.2 Ammonia Oxidation

A large project on time-of-flight mass spectrometer is a project on ammonia oxidation on Pt nanoparticles. Here we try to relate the activity of Pt nanoparticles to the particle size. The result of this study is thoroughly documented in the masters thesis by Mathis Kjærgaard Christensen[42] and here I will mostly focus on the new abilities the TOF-instrument has provided for this kind of project.

In this case we want to use the TOF in a time-resolved way much like a traditional QMS. This means that one needs to take many TOF spectrums at high repetition rate. This has the great advantage that one does not have to chose which masses to follow, instead the complete spectrum is acquired for each repetition. The negative side of this is that the measurements take up quite large amounts of storage space. In this mode of operation it is almost impossible to do real-time data analysis, especially not if the spectrum contains overlapping peaks, which would of course often be the case in situations where it would be interesting to prefer the TOF over the QMS. What we do instead is to simply blindly record the data (which is what we typically do anyway, since almost all measurements run unattended) and then treat the data after the experiment is finished.

The way the data is treated is to chose a list of wanted masses and then do the procedure of Gaussian fits as shown in Figure 8.4 for each mass for each recorded spectrum. These  $\sim 100 - 1000$  Gaussian fits (depending on the duration of the measurement) can be performed in a very short time using a simple home written piece of software. Of course one need to make sure that all the fits are performed correctly, and this is ensured by producing a pdf-file containing all the fits which can easily be inspected for fitting errors. An example of a page from such a file is shown in Figure 8.11.

Once all the Gaussian fits are performed correctly, it is an easy matter to plot the data in the same way that one would present data from a QMS. To compare the two measurement techniques, we performed a simultaneous measurement on both instruments, and the result is

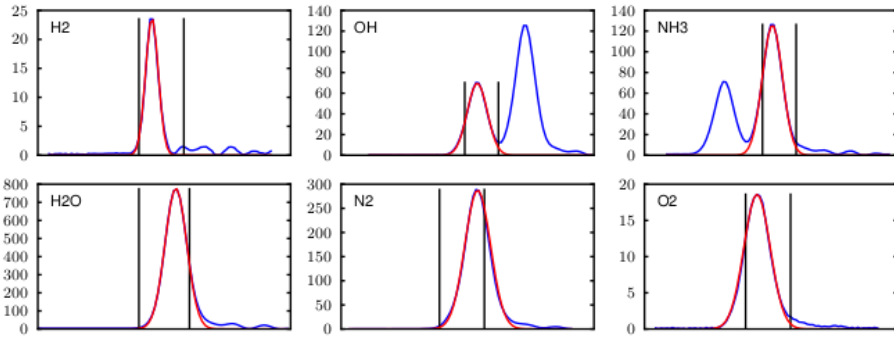


**Figure 8.11** – Example of a single page in the pdf produces for each mass-time measurement. The black lines indicates the data-range used for each fit. The blue lines are the raw data and the red lines the corresponding fit. By combining all the fits into a single pdf, it is extremely easy to verify that all fits are performed correctly.

shown in Figure 8.12. It is evident that opposite to the QMS, the TOF is able to document the fact that the ammonia is completely converted. In the QMS the water signal at mass 17 prevents this from being measured, it is almost impossible to tell, that the ammonia is actually gone. It is also easy to see, that the time resolution is currently not nearly as good as the QMS, this is very much due to our primitive ion source which forces us into rather long integration times to get good spectra. Also it is important to realize that for the QMS all the logged masses are shown in the plot, if we later find out we are interested in another mass, we have no way to retrieve this data. For the TOF data, the plotted masses are simply the ones, we have chosen to plot, we can at any time go back to the recorded data and plot the time evolution of any wanted mass, since the raw data contains complete mass spectra.

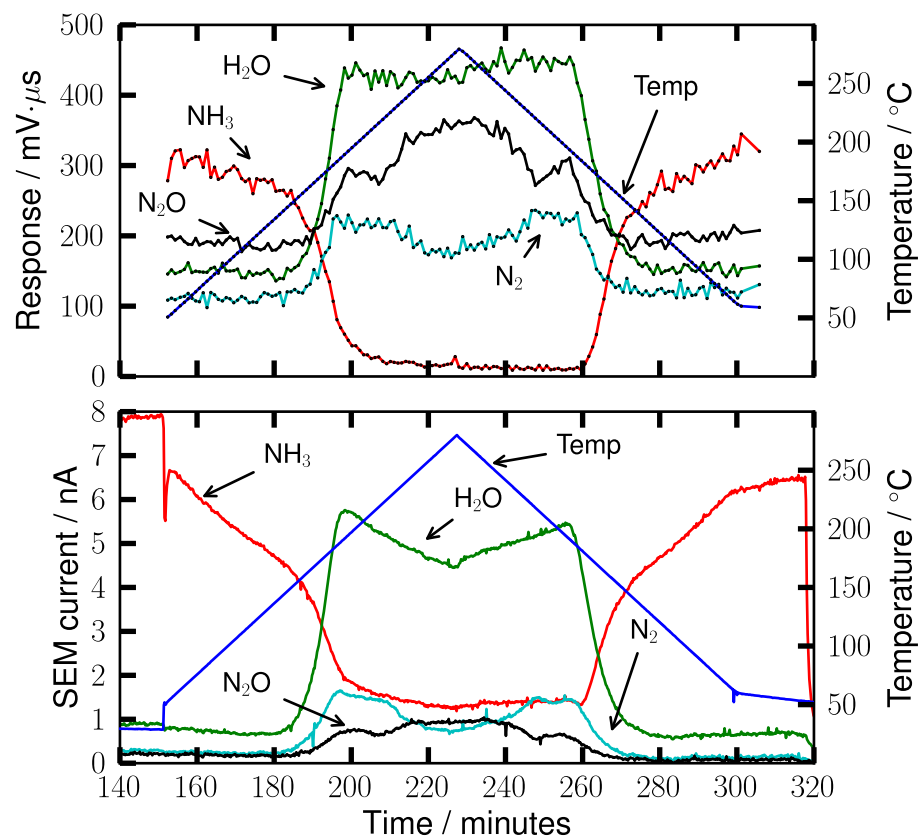


Figure 8.12 – Measurements from the QMS and TOF of the same sample at the same time.

# Chapter 9

## Hot Electron Devices

In the first part of my Ph.D. I was not working with  $\mu$ -reactors, but with a completely different system where the goal was to do non-thermal catalysis using a so-called Hot-Electron Device. The devices was originally developed at CINF by Ph.D. students Gunver Nielsen and Lasse Thomsen, who made a number of publication on the subject ([45, 46, 47]) as well as a Ph.D. thesis each ([48, 49]). In short the Hot Electron project was about trying to create a Metal-Insulator-Semiconductor (MIS) device which could be used as a tunnel device to perform chemistry with non-thermal electrons, also the device could work as a low-temperature free electron emitter. Below is a very short introduction as well as a report of some my work on the project.

### 9.1 Hot Electron Chemistry

The hot-electron work at CINF was based on an idea by Gadzuk ([50, 51, 52]) that certain chemical reactions can be induced by introducing a 'hot' (that is, having more energy than what would be expected from the temperature of the material) electron directly at the reaction coordinate. In this way it would in principle be possible to do certain chemical reactions extremely efficiently since all applied energy would go directly do the desired process and not as a general heating of the entire system. This would also in principle open a route to do extremely specific reactions even if they are thermodynamically competing with other unwanted reaction since one could simply tune the electron energy to the desired reaction.

### 9.2 The Hot-Electron Device

The original implementation of the device was done by Lasse and Gunver. The device is implemented as a Semiconductor-Insulator-Metal structure. The starting point is a plain Si-wafer (Figure 9.1) doped rather heavily with antimony (Sb) to achieve a high conductance of the wafer, in fact the conductance is so high that for the relevant current densities, it will act more or less as a metal conductor. The first step is then to grow a thick oxide on the wafer, the thickness being on the order of 750 nm, Figure 9.2. This oxide is grown as a co-called wet-oxide meaning that it is oxidized in a wet atmosphere which speeds up the process significantly. The price of the fast growth is that the quality of the oxide is rather poor, it contains a lot of defects and is general not nearly as good an insulator as perfect

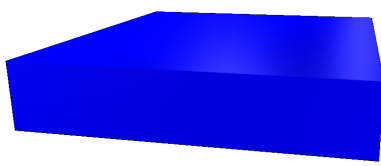


**Figure 9.1** – The original wafer

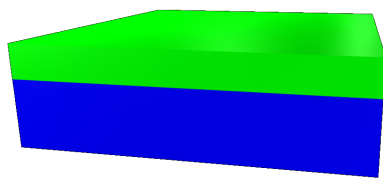


**Figure 9.2** – The wafer after growing the thick oxide

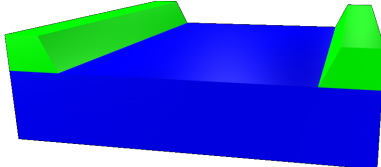


**Figure 9.3** – Back-etching the thick oxide in the active area

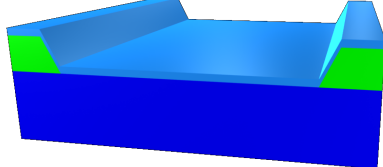


**Figure 9.4** – Growth of the high-quality thin oxide

$\text{SiO}_2$ . This is not a problem in this case since the oxide is not meant to be a part of the actual active hot-electron structure, but it will later work as an area of the chip that can be easily handled mechanically.

After the growth of the thick oxide, the area that is later to become the active area, is then back-etched in HF, with the rest of the oxide being protected by a protective layer applied by photo lithography, Figure 9.3. Etching in HF is extremely selective towards  $\text{SiO}_2$  and thus the etch will not introduce roughening of the otherwise almost atomically flat Si surface if the etch time is just decently adjusted to fit the time needed to remove the oxide layer. At this point we have a device structure of an outer rim of thick oxide for mechanical handling and the center part of the device etched back to the bare wafer. Next step is to grow the final thin, high-quality oxide, that will work as the tunnel barrier. To do this, the wafers are first so-called RCA cleaned and immediately after transferred into an extremely clean furnace where the oxidation is performed in a dry oxygen atmosphere, Figure 9.4. In the complete fabrication process, this is by far the most import step to get right, since the quality of the oxide is of extreme importance for the performance of the device. It is thus extremely important that the cleaning is done right, and that absolutely no particles is contaminating the surface when the wafers are transferred into the furnace.

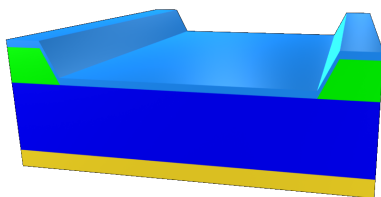


**Figure 9.5** – Metal is deposited on the backside for easy electrical contact.

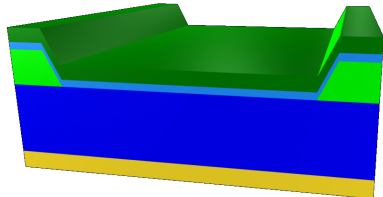


**Figure 9.6** – Finally metal is deposited on the front side.

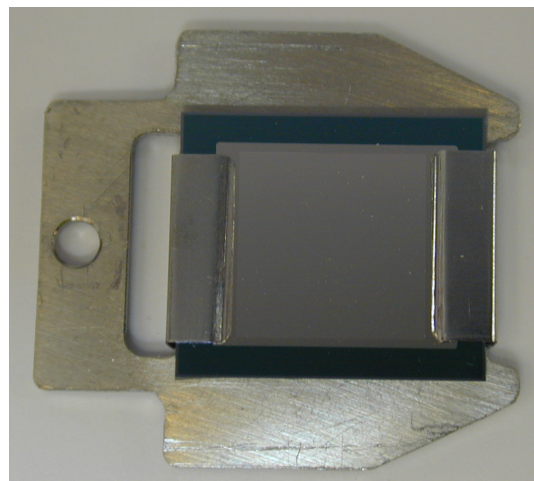


**Figure 9.7** – Photograph of the finished sample ready for mounting in the setup.

After growing the thin oxide, the next step is to deposit a metal layer on the backside of the wafer, Figure 9.5. This is done to ensure good electrical contact to the device, since the silicon itself is a very stiff surface, which can be hard to contact. The standard back-side metal is 100 nm Au on top of a few nm of Ti as an adhesion layer between the silicon and the gold. At this point the wafers are ready for the final step, which is to deposit the front side metal, Figure 9.6. The deposition is done using standard e-beam evaporation though a shadow-mask. The choice of metal is depending on what experiment one wants to perform, often we have worked with Pt, but other metals can also be deposited.

### 9.3 Experimental setup

The experiments are performed in a standard UHV chamber, at CINF known as the 'Volvo', the origin of name is not completely clear to me, but apparently it started its life at a Swedish car manufacturer. The chamber has a typical base pressure of  $1 \times 10^{-10}$  mbar and is pumped by a turbo pump ensuring a clean vacuum. The samples are mounted from a load-lock pumped by a separate turbo, and it is thus possible to change the samples without compromising the vacuum of the main chamber. A schematic drawing of the chamber is seen in Figure 9.8. The chamber is equipped with a hemispherical analyzer, a quadropole mass spectrometer, an x-ray gun and two ion guns. This means that techniques such as XPS, ISS and TPDs are easily available. The ion guns can also be used for sputter cleaning samples, even though this is not a very good technique on the hot-electron devices since most sputtering processes will severely degrade the gate-oxide thus introducing large leak-currents and possibly even destroying the device completely.

### 9.4 Results

The experimental work on the devices is divided into two main sections, hot-electron chemistry and free electron emission. The original goal for the project was to do hot-electron chemistry,

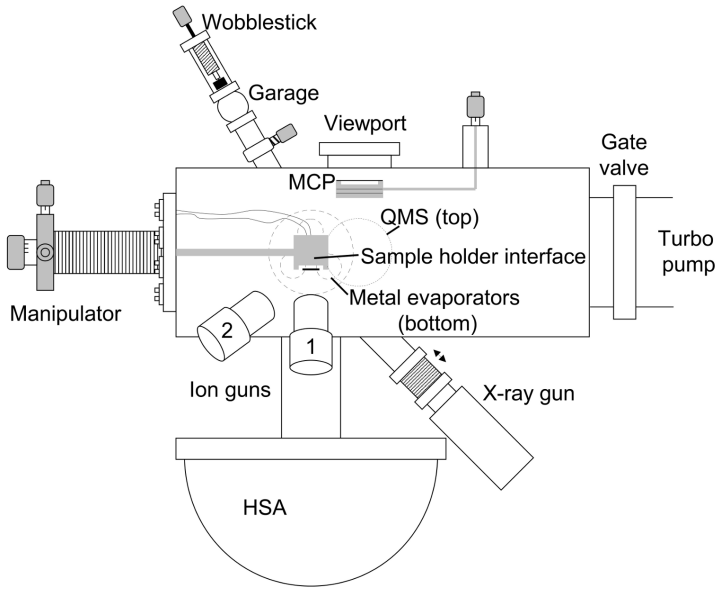


**Figure 9.8** – Schematic drawing of the UHV chamber. Drawing originally from [48].

but as it turned out, that the device could be used as a fairly efficient electron emitter, some amount of work was also put into optimizing this property. The overall scope of the two lines of work are very different, the attempt to do chemistry is highly ambitious and could potentially have significant consequences if it was actually brought to work. The free electron emission has a more technological perspective in areas of research or industry where one would like an electron source that is not heated to high temperatures like a filament.

#### 9.4.1 Hot Electron Chemistry

The status of this part of the project at the time Gunver wrote her thesis (and thus the last results to be presented in public) was that we had run a series of attempts to detect hot electron chemistry in two different ways. The test reaction was always CO desorption, since this has been theoretically predicted to be a favorable test reaction[53]. One way to detect this reactions, obviously is to position the sample beneath the mass spectrometer and try to run the reaction and look for CO in the mass spec. To lower the background, the experiments was always performed with isotopically labeled CO,  $^{13}\text{C}^{16}\text{O}$ . This experiment has been performed many times with a range of different electron energies, however we have never been able to detect any signs of hot electron induced desorption. Because of the failure of the direct detection, the other way of testing the reaction was to run a batch experiment. First two  $^{29}\text{CO}$  TPDs are performed, then hot electrons are applied for 60 min and finally another TPD is performed after 60 min without electrons. This method is potentially more sensitive, since it integrates the effect of the electrons over an extended period of time. However, the method also demands extremely high consistency, since the result is only visible as a difference between the two TPDs which of course is much more indirect than simply looking for the reaction product. As shown in Figure 9.9, also this method failed to show an effect of the electrons. Some difference between the TPDs was visible, but the difference was

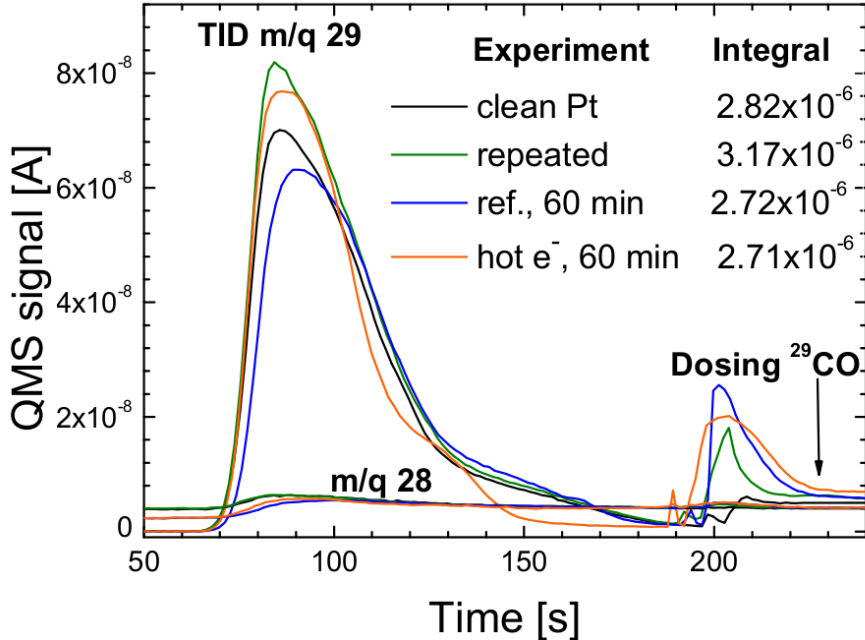


**Figure 9.9** – The result of the batch experiment. As can be seen, the difference in TPD signal with and without hot-electrons is not significantly larger than the difference among the individual TPDs. Figure originally from [48].

not even close to be significant enough to claim that this was due to the electrons.

The final attempt, performed after Gunver wrote her thesis, at detecting a hot-electron induced effect was to apply a simple lock-in technique. In many situations, lock-in amplification can be extraordinary efficient at measuring signals on a very large noise background, provided that the signal oscillates with a driven frequency that can be used for the lock-in. The idea in our case was to pulse the device and lock-in the mass-spectrometer signal on the pulse frequency. However, due to the non-vanishing capacitance of the device, it was only possible to pulse the device with a frequency of  $\frac{1}{3}$  Hz, which is at least 1000 times less than what one would typically use for lock-in amplification. To increase the sensitivity not only the mass spectrometer was used for the detection, also the ion gauge signal was monitored since the gauge has a much higher sensitivity than the mass spec, and since only a single gas-species is involved, it can safely be assumed that an increase in global pressure is equal to an increase in  $^{29}\text{CO}$  partial pressure.

A typical result of this kind of measurement is shown in Figure 9.10. Also this result was negative, no signal is visible neither in the direct measurements or in the Fourier transform, where a positive result should show up as a peak at 0.33 Hz. In Figure 9.11 is shown how the result should look in the case of a successful outcome. This particular sample had suffered a breakdown of the gate oxide and thus had electrical contact between the front side and the backside of the device resulting in ohmic heating of the device. The result of this pulsed heating is exactly the wanted pulsed desorption feature, however of course this is not due to the hot electrons. However, the result is interesting in so far as it puts a baseline on the magnitude of measurable signal. As can be seen from Figure 9.11 the pulses have a magnitude of  $\sim 2 \times 10^{-12}$  mbar in the ion gauge and no detectable signal in the mass spectrometer, ie.

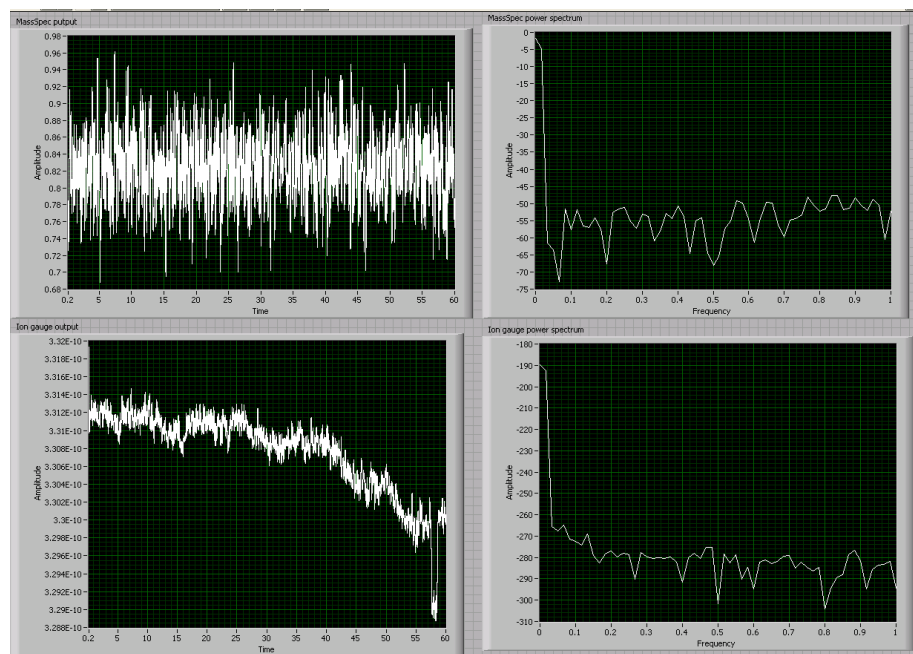


**Figure 9.10** – A typical result of the pulsed tests. The mass spectrometer is continuously measuring mass 29 and the output is shown on the top left. The output from the ion gauge is shown bottom left. The right column shows the Fourier transform of the corresponding signals. A hot-electron effect should show up as a peak at 0.33 Hz.

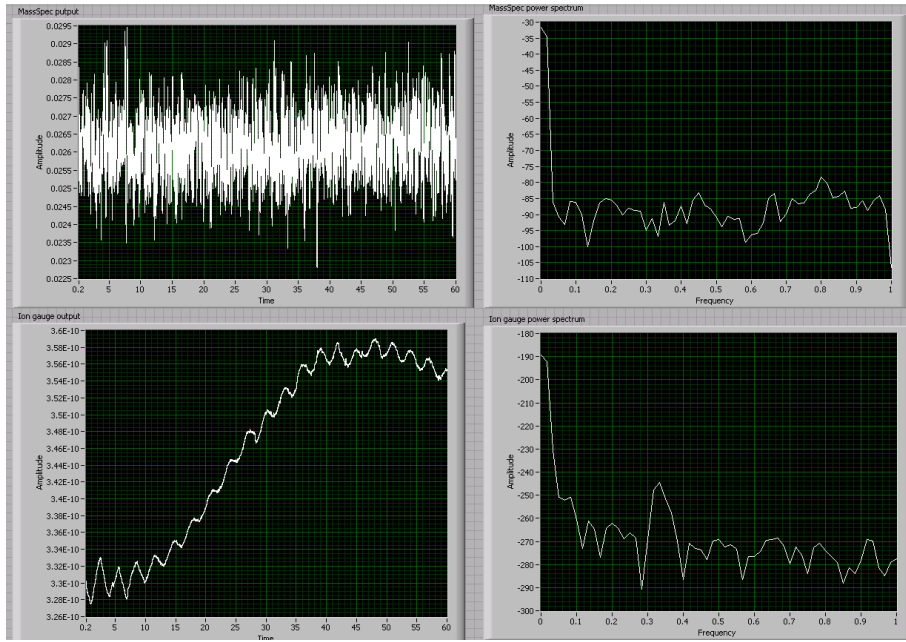


**Figure 9.11** – Simulated result of what would be the expected fingerprint of hot electron induced desorption. This spectrum was achieved with a device with a broken oxide which and thus ohmic currents provides extremely local heating which desorbs the CO.

only very few ions actually desorbed. This means that the actual effect of the hot electrons must be much smaller than this. Even if any effect should exists, it will certainly be difficult to talk about ultra efficient chemistry.

#### 9.4.2 Electron emission

The application of the devices as a free electron emitter is a very different project from the electron induced chemistry. This is a much more technological aspect and in many respects a much more realistic application. However, since our group is put in the world to do catalysis, not cold electron emitters, this project has always been a side-project even though one complete masters project did come out and documented many of the results[54]. Very conveniently, one potential application for a cold electron emitter (sorry for the slightly confusing terminology, a more correct name would perhaps be a cold emitter of free hot electrons...), is exactly UHV science, where the outgassing from a hot filament is typically unwanted. Therefore we wanted to test this application directly in our own setup. The principle would be to try to run the mass-spectrometer with the hot-electron device as electron source for the ionization instead of the normal filament. However, this involves to get the mass-spectrometer to actually operate without turning on the filament, in the normal mode of operation the mass-spectrometer hardware contains various safety mechanisms that will prevent the mass-filter from operating when the filament is not turned on (properly this is because a non-operating filament is an indirect indication that the vacuum is somehow compromised and it would then be dangerous to turn on the various voltages in the rod-system). However, a mail to Pfeiffer support revealed that this safety mechanism can be



**Figure 9.12** – Mass spectrum of clean chamber taken using an external filament as ion source. Helium and Argon was dosed into the chamber while running the experiment.

by-passed by connecting the filament wires to a resistor of approximately  $1\Omega$  and connect the resistor to ground through approximately  $100\text{ k}\Omega$ . If this procedure is followed, the mass spectrometer will turn on all electronics and work fully as a mass spectrometer, however now without an ion source. The idea would now be to position the sample physically underneath the mass spectrometer and simply emit electrons from the device. This is in principle a simple strategy, however in real life it is slightly more complicated. Partly because of the mentioned issues getting the mass spec to run in this mode at all, partly because the hot electron devices are very fragile and breaks down very often, especially when biased enough to emit electrons into the vacuum. This means that these experiments are plagued by infinite amounts of practical problems which slows down the project a lot. In the end, I ended up running the experiment in 'cheat' mode, that is, without using the actual device. Instead a spectrum was taken using an external filament, just to prove that it is indeed possible to provide external ions to a mass spectrometer. As shown in Figure 9.12, this works fine. However, the real demonstration with an actual cold ion source did not succeed before we closed the entire hot electron project, and I moved to the  $\mu$ -reactors.

## 9.5 Conclusions on the hot electron project

Perhaps the most productive result achieved doing my time with the hot electrons, was the very sensitive demonstration of the absence of a hot electron effect for CO desorption. The pulsed experiments showed that if of hot electron induced desorption takes place at all, the reaction rate is extremely low and even if we some day should succeed in showing the effect, any claim of high efficiency is certainly wrong. Regarding the electron emission, I see much more perspective. However, getting this to work reliably is a huge amount of work, and since this application is so far away of the core focus of the group, it is not really a project that fits in, which is of course also the reason we eventually decided to close down the project.

# Chapter 10

## Future plans

Ever since I joined the  $\mu$ -reactor team, the setup has been in a permanent state of flux, and I am very happy that this condition does not seem to end any time soon. So far we have several plans for enhancements, some is almost guaranteed to be implemented and others are perhaps somewhat more optimistic. Here I will present a list of ideas that I hope will be implemented within the coming years.

**Storing the flow-files with the data** It would be a great advantage in the daily work to know exactly what flow-file was used to run a given experiment. Right now we log all measured parameters, but we do not log the intended values of these parameters. This means that if an experiment does not run exactly as expected, it can be hard to tell whether it was simply the operator that set up the experiment wrong, or if it was some sort of malfunction that prevented the experiment from running correctly.

**Better software** Most of the software is currently written as a few rather monstrous LabView programs because this has been the default language at the department. However, these very large LabView problems suffers from poor stability, a steep learning curve for new students and very difficult debugging. Thus we are now slowly moving to a more modular approach where sub-sections of the code can be separated into individual programs, preferably written in other programming languages. So far we already interface quite a few instruments in Python[55] on other setups and it would be obvious to gradually also turn the  $\mu$ -reactors in this direction.

**Mounting for a microscope on the NG setup.** As mentioned in chapter 7, it could be interesting to be able to do high-quality optical imaging of the sample while running experiments. However, actually getting good images has turned out to be a nightmare of practicalities. What would be a perfect solution would be a holder mounted in a fixed position compared to the sample to allow for self-consistent images. If one is allowed to be even slightly more ambitious, the holder should contain an actuated x-y stage and a computer interfaced microscope to allow for scanning the position and do systematic imaging. This would be necessary if one wants to do high resolution imaging of the sample to search for temperature fingerprints of the reactions in the reactor.

**Adding an optional pumping path between the buffer chambers and the turbo**

Currently the buffer chambers are pumped by a turbo pump through 1/4" tubing because this limited radius protects the turbo when large amount of gas is being dumped in the buffer volume. However, often one knows that no further gas is going to be dumped into the buffer volume and just want to pump down it sufficiently to be able to start the experiment. In situations like this, it would be extremely useful to have an optional pumping path of much larger diameter. This could easily be achieved by mounting a 2 3/4"-bellow and a pneumatically controlled valve between the buffer and the turbo. Such a device would significantly reduce the time needed to pump down a new sample before starting measurements and thus increase the overall throughput considerably.

**Re-building the old setup** Currently only one of our setups are equipped with the newest improvements of full automation and an evacuated containment volume, these improvements obviously need to be applied to the other setup as well.

**Higher pressures** Currently we are able to work in the pressure range of 0-2.5 bars. For some reactions it would very useful to be able to reach higher pressures. A prime example that is currently being investigated is methanol production on Cu/Zn nanoparticles, where the output of the process is expected to increase with the pressure squared. Currently we are limited by the pressure controllers but these could of course be replaced simply by buying new ones. However, even though replacing the pressure controllers is an easy task, the rest of setup also puts severe limits on the pressure. The next limit will be the flow controllers, which are only designed for 4 bars on the high pressure side. On the next level, none of our tubing are certified for high pressures, and thus the ultimate pressure limit will mostly be a question of how high the operators dares to pressurize these tubes.

**In-situ deposition and bonding under UHV conditions** This is a slightly ambitious project but with a potentially very high value. The point would be to build a chamber where it is possible to deposit cluster samples on a  $\mu$ -reactor, perform various kinds of analysis and finally bond the sample, all under UHV conditions. This would significantly enhance the  $\mu$ -reactor platform as a tool to bridge the pressure gap between traditional UHV analysis and the high pressure conditions of the  $\mu$ -reactor, since we would be able to measure on truly clean samples that have never been exposed to air. Of course transfer between this setup and the  $\mu$ -reactor setup would be a weak point since this cannot possibly be done under UHV conditions. My proposal for the transfer would be to fill the reactor with 1 bar of inert gas before removing it from the bonding setup. Filled with gas, the reactor will only see air if the sample is exposed to air long enough that it will diffuse all the way through the mixing channels and into the reactor volume. The time-scale for this should be sufficiently long that it is possible to either mount the sample in the  $\mu$ -reactor setup and evacuate it, or to store it in a suitable clean environment.

**UHV connection between sputter deposition chamber and cluster deposition** CINF recently acquired a high-quality sputter deposition system capable of depositing a very large range of materials, including many oxides. If this system is attached to the future in-situ bonding setup, it would be possible to use the  $\mu$ -reactor for exploring a wide range of substrate effects, since we could sputter-deposit the wanted substrate, then deposit clusters, characterize the sample using either auger or TPDs before finally bonding the sample. All under highly clean conditions.

---

**Application of in-situ techniques** This is of course the crown jewel of all wishes for the future. There can be no doubt that the single greatest weakness of the  $\mu$ -reactor platform is the lack of in-situ (or even ex-situ for that matter...) surface sensitive techniques. As discussed in chapter 7, this is not an easy task. However, considering the benefits of gaining such insights into the system, the operators of the setup, should at all times keep in mind new ways to try fulfill this goal. As my supervisor, Ib, always says; You've got to have a dream, to have a dream come true...



# Bibliography

- [1] BTM Consult. *World Market Update 2011*. 2012.
- [2] International Monetary Fund. Report for selected country groups and subjects. Web, 2112.
- [3] International Energy Agency. Key world energy statistics. Technical report, International Energy Agency, 2011.
- [4] D. Heide, L. von Bremen, M. Greiner, C. Hoffmann, M. Speckmann, and S. Bofinger. Seasonal optimal mix of wind and solar power in a future, highly renewable europe. *Renewable Energy*, 35(11):2483–2489, November 2010.
- [5] T. R. Henriksen, J. L. Olsen, P. Vesborg, I. Chorkendorff, and O. Hansen. Highly sensitive silicon microreactor for catalyst testing. *Review of Scientific Instruments*, 80(12):124101, December 2009.
- [6] Toke Riishøj Henriksen. *Silicon Microreactors for Measurements of Catalytic Activity*. PhD thesis, 2010.
- [7] Zübeyr Yüksel. Reactivity of mass selected nano particles measured in micro reactors. Master's thesis, 2011.
- [8] Peter C. K. Vesborg. *Photocatalysis in  $\mu$ -reactors and related activities*. PhD thesis, 2010.
- [9] Jakob Lind Olsen. *Heterogeneous catalysis in highly sensitive microreactors*. PhD thesis, 2010.
- [10] P. C. K. Vesborg, J. L. Olsen, T. R. Henriksen, I. Chorkendorff, and O. Hansen. Note: Anodic bonding with cooling of heat-sensitive areas. *Review of Scientific Instruments*, 81(1):016111, January 2010.
- [11] <http://www.mksinst.com/product/Product.aspx?ProductID=648>.
- [12] <http://www.m seals.dk>. O-ring. Technical report, M Seals A/S, 2012.
- [13] <http://www.chem.agilent.com/en US/Products/Instruments/vacuum/vacuummeasurement/gaugecontrollers/xgs-600/Pages/default.aspx>.
- [14] Alex Willumsen. Development of integrated labview programs for micro-reactors for test of heterogeneous and photo catalysts. Bachelors Thesis, 2008.
- [15] <http://www.keithley.com/products/dcac/currentvoltage/lowcurrent/?mn=2635A>.

---

## BIBLIOGRAPHY

- [16] Mikkel Rykær Kraglund. Reactivity of mass selected nanoparticles measured in microreactors, 2011.
- [17] D. L. Bashlakov, L. B. F. Juurlink, M. T. M. Koper, and A. I. Yanson. Subsurface oxygen on pt(111) and its reactivity for co oxidation. *Catalysis Letters*, 142(1):1–6, January 2012.
- [18] S. B. Simonsen, I. Chorkendorff, S. Dahl, M. Skoglundh, J. Sehested, and S. Helveg. Direct observations of oxygen-induced platinum nanoparticle ripening studied by in situ tem. *Journal of the American Chemical Society*, 132(23):7968–7975, June 2010.
- [19] R. M. Nielsen, S. Murphy, C. Strelbel, M. Johansson, J. H. Nielsen, and I. Chorkendorff. A comparative stm study of ru nanoparticles deposited on hopg by mass-selected gas aggregation versus thermal evaporation rid a-9089-2011 rid c-7282-2008. *Surface Science*, 603(24):3420–3430, December 2009.
- [20] R. M. Nielsen, S. Murphy, C. Strelbel, M. Johansson, I. Chorkendorff, and J. H. Nielsen. The morphology of mass selected ruthenium nanoparticles from a magnetron-sputter gas-aggregation source rid c-7282-2008 rid a-9089-2011. *Journal of Nanoparticle Research*, 12(4):1249–1262, May 2010.
- [21] M. Eiswirth and G. Ertl. Kinetic oscillations in the catalytic co oxidation on a Pt(110) surface. *Surface Science*, 177(1):90–100, November 1986.
- [22] B. L. M. Hendriksen and J. W. M. Frenken. Co oxidation on Pt(110): Scanning tunneling microscopy inside a high-pressure flow reactor. *Physical Review Letters*, 89(4):046101, July 2002.
- [23] B. L. M. Hendriksen, S. C. Bobaru, and J. W. M. Frenken. Bistability and oscillations in co oxidation studied with scanning tunnelling microscopy inside a reactor. *Catalysis Today*, 105(2):234–243, July 2005.
- [24] B. L. M. Hendriksen, M. D. Ackermann, R. van Rijn, D. Stoltz, I. Popa, O. Balmes, A. Resta, D. Wermeille, R. Felici, S. Ferrer, and J. W. M. Frenken. The role of steps in surface catalysis and reaction oscillations. *Nature Chemistry*, 2(9):730–734, September 2010.
- [25] J. Singh, M. Nachtegaal, E. M. C. Alayon, J. Stotzel, and J. A. van Bokhoven. Dynamic structure changes of a heterogeneous catalyst within a reactor: Oscillations in co oxidation over a supported platinum catalyst. *Chemcatchem*, 2(6):653–657, June 2010.
- [26] V. P. Zhdanov and B. Kasemo. Kinetic oscillations on nm-sized catalyst particles: Surface restructuring. *Surface Science*, 513(1):L385–L390, July 2002.
- [27] P. A. Carlsson, V. P. Zhdanov, and M. Skoglundh. Self-sustained kinetic oscillations in co oxidation over silica-supported Pt. *Physical Chemistry Chemical Physics*, 8(23):2703–2706, 2006.
- [28] X. Q. Gong, R. Raval, and P. Hu. General insight into co oxidation: A density functional theory study of the reaction mechanism on platinum oxides. *Physical Review Letters*, 93(10):106104, September 2004.
- [29] H. P. Bonzel and R. Ku. Kinetics of oxygen adsorption on a pt(111) surface. *Surface Science*, 40(1):85–101, 1973.

---

## BIBLIOGRAPHY

- [30] I. Chorkendorff and H. Niemantsverdriet. *Concepts of Modern Catalysis and Kinetics*. Wiley-VCH, Weinheim, 2007.
- [31] R. T. Bayard and D. Alpert. Extension of the low pressure range of the ionization gauge. *Review of Scientific Instruments*, 21(6):571–572, 1950.
- [32] <http://www.thinksrs.com/downloads/PDFs/ApplicationNotes/IG1BAgasapp.pdf>.
- [33] A. M. Contreras, X. M. Yan, S. Kwon, J. Bokor, and G. A. Somorjai. Catalytic co oxidation reaction studies on lithographically fabricated platinum nanowire arrays with different oxide supports. *Catalysis Letters*, 111(1-2):5–13, October 2006.
- [34] E. M. Larsson, C. Langhammer, I. Zoric, and B. Kasemo. Nanoplasmonic probes of catalytic reactions. *Science*, 326(5956):1091–1094, November 2009.
- [35] <http://www.rmjordan.com/OrthogoTOF/orthogotof.html>.
- [36] <http://www.rmjordan.com/mcpdetector.html>.
- [37] M. Krems, J. Zirbel, M. Thomason, and R. D. DuBois. Channel electron multiplier and channelplate efficiencies for detecting positive ions. *Review of Scientific Instruments*, 76(9):093305, September 2005.
- [38] W.B. Nottingham. *Vacuum Symposium Transactions*. Committee on Vacuum Techniques, Boston, 1955.
- [39] L. J. Kieffer and G. H. Dunn. Electron impact ionization cross-section data for atoms atomic ions and diatomic molecules .i. experimental data. *Reviews of Modern Physics*, 38(1):1–&, 1966.
- [40] Stanford Research Systems. Bayard-alpert ionization gauges. Technical report, Stanford Research Systems.
- [41] <https://github.com/robertjensen/FlightTime>.
- [42] Mathias Kjærgaard Christensen. Ammonia oxidation studied in  $\mu$ -reactors. Master’s thesis, 2012.
- [43] NIST Mass Spectrometry Data Center. Benzene - the NIST webbook.
- [44] K. M. Bratlie, H. Lee, K. Komvopoulos, P. D. Yang, and G. A. Somorjai. Platinum nanoparticle shape effects on benzene hydrogenation selectivity. *Nano Letters*, 7(10):3097–3101, October 2007.
- [45] L. B. Thomsen, G. Nielsen, S. B. Vendelbo, M. Johansson, O. Hansen, and I. Chorkendorff. Electron emission from ultralarge area metal-oxide-semiconductor electron emitters. *Journal of Vacuum Science & Technology B*, 27(2):562–567, March 2009.
- [46] L. B. Thomsen, G. Nielsen, S. B. Vendelbo, M. Johansson, O. Hansen, and I. Chorkendorff. Ultralarge area mos tunnel devices for electron emission. *Physical Review B*, 76(15):155315, October 2007.
- [47] G. Nielsen, L. B. Thomsen, M. Johansson, O. Hansen, and I. Chorkendorff. Electron emission from mos electron emitters with clean and cesium covered gold surface rid c-4480-2011 rid c-7282-2008. *Applied Surface Science*, 255(17):7657–7662, June 2009.

---

## BIBLIOGRAPHY

- [48] Gunver Nielsen. *Production of Hot Electrons for Enhancement of Surface Reactivity*. PhD thesis, 2009.
- [49] Lasse Thomsen. *MIS hot electron devices for enhancement of surface reactivity by hot electrons*. PhD thesis, 2009.
- [50] J. W. Gadzuk. Inelastic resonance scattering, tunneling, and desorption. *Physical Review B*, 44(24):13466–13477, December 1991.
- [51] J. W. Gadzuk. Resonance-assisted, hot-electron-induced desorption. *Surface Science*, 342(1-3):345–358, November 1995.
- [52] J. W. Gadzuk. Resonance-assisted hot electron femtochemistry at surfaces. *Physical Review Letters*, 76(22):4234–4237, May 1996.
- [53] T. Olsen, J. Gavnholt, and J. Schiotz. Hot-electron-mediated desorption rates calculated from excited-state potential energy surfaces. *Physical Review B*, 79(3):035403, January 2009.
- [54] Paolo Malacrida. Optimization of hot electron emitter devices. Master’s thesis, 2009.
- [55] <https://github.com/CINF/PyExpLabSys>.

---

*BIBLIOGRAPHY*

**Paper 1**

**Self-sustained carbon monoxide oxidation oscillations on size-selected platinum nanoparticles at atmospheric pressure**

Submitted to Angewandte Chemie.

---

# Self-sustained carbon monoxide oxidation oscillations on size-selected platinum nanoparticles at atmospheric pressure

Robert Jensen<sup>b</sup>, Thomas Andersen<sup>b</sup>, Anders Nierhoff<sup>b</sup>, Thomas Pedersen<sup>c</sup>, Ole Hansen<sup>c</sup>, Søren Dahl<sup>b</sup> and Ib Chorkendorff<sup>a</sup>

High-quality mass spectrometry data of the oscillatory behavior of CO oxidation on SiO<sub>2</sub> supported mass selected Pt-nanoparticles at atmospheric pressure has been acquired as a function of pressure, coverage, gas composition and nanoparticle size. The oscillations are self-sustained for several days at constant temperature, pressure and CO/O<sub>2</sub> ratio. The frequency of the oscillations is very well defined and increases over time. The oscillation frequency is furthermore strongly temperature dependent with increasing temperature resulting in increasing frequency. A plausible mechanism for the oscillations is proposed based on a oxidation/reduction cycle of the nanoparticles which change the rate of CO oxidation on the particles.

## 1 Introduction

CO oxidation is one of the most studied reactions due to its importance in both automotive catalysis and in the removal of trace CO in hydrogen streams. A large effort and a large number of experiments with a variety of surface sensitive techniques have been conducted on single crystal surfaces greatly improving the understanding of this reaction. Single crystal surfaces are well suited model systems due to the high degree of achievable control of parameters compared to industrial catalysts. Here we report on studies in a microreactor model system of Pt nanoparticles. The size-selected nanoparticles supported on a SiO<sub>2</sub> substrate show oscillatory behavior of CO oxidation at atmospheric pressure.

Oscillating reactions on single crystals at UHV conditions have been studied extensively and is known to originate from surface reconstructions of the surface during the oscillations<sup>1</sup>. It has previously been shown<sup>2</sup> that CO oxidation at atmospheric pressures also shows oscillatory behavior on single crystals of Pt, Pd and Ir. Recent studies have proposed a mechanism on Pd<sup>3</sup> attributed to a cycle of surface oxide formation, oxide roughening and clean metal surface formation. CO oxidation oscillations has also been observed on Pt thin films<sup>4</sup>, in macroscopic flow reactors<sup>5</sup> and on Pt nanoparticles synthesized from wet chemical synthesis and subsequent annealing<sup>6</sup>. Here we investigate CO oscillations in a microreactor model system on size selected Pt nanoparticles by high sensitivity mass spectrometry.

## 2 Experimental Methods

The experiments were performed in Si-based  $\mu$ -reactors<sup>7</sup>. The reactor design makes sure that all gases exposed to the catalyst under investigation is measured by the quadrupole mass spectrometer (QMS) ensuring an extremely high sensitivity of the system.

Pt nanoparticles were deposited in the reactor using a gas-aggregation source. The nanoparticles were size-selected by a quadrupole mass selection filter according to their mass-to-charge ratio. Using this setup Pt nanoparticles with diameters in the range of 2–16 nm can be produced<sup>8</sup>. After deposition the reactors were anodically cold-bonded<sup>9</sup> to a pyrex lid to avoid sintering of the nanoparticles while bonding.

## 3 Results

An oscillation measurement is performed by mounting a sample in the setup directly after cluster deposition and anodic bonding. Initially a light-off CO- oxidation measurement is performed (shown in Figure 1) where the temperature is increased at 3 °C/min until the sample ignites and achieves full conversion of CO to CO<sub>2</sub>. At CO:O<sub>2</sub> ratio of ~ 0.08 and a geometrical Pt coverage of ~ 0.1% light-off occurs at approximately 180 °C. The temperature ramp is typically continued up to 260 °C whereafter the temperature is decreased at 3 °C/min. After the initial light-off the sample is cooled to room temperature. When at room temperature the temperature is again increased at 3 °C/min until sustained oscillations occur. A typical initial treatment is seen in Figure 1. Often the sample will show oscillations either directly upon light-off or on the falling temperature ramp.

Nanoparticles with sizes ranging from 3 nm to 9 nm have been tested but 3 nm particles with a geometrical coverage of 0.1% of the reactor area gave the most stable oscillations. No

---

<sup>a</sup> CINF, Department of Physics, Technical University of Denmark, Fysikvej 312, 2800 Lyngby, Denmark. E-mail: ibchork@fysik.dtu.dk

<sup>b</sup> CINF, Department of Physics, Technical University of Denmark, Fysikvej 312, 2800 Lyngby, Denmark

<sup>c</sup> CINF, Department of Micro- and Nanotechnology, Technical University of Denmark, Ørsted Plads 345 East, 2800 Lyngby, Denmark

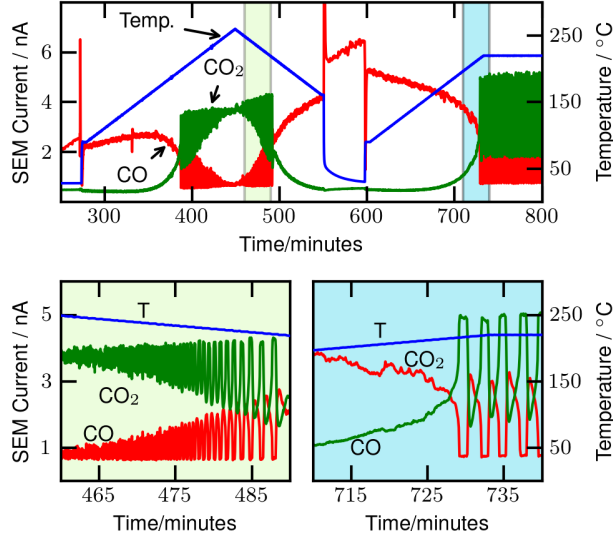


**Fig. 1** A typical example of the initial treatment of a new sample. After performing a light-off ramp where oscillations can be seen the temperature is increased to a constant value where sustained oscillations take place. The non-zero value of CO during high conversion periods is consistent with the expected QMS background signals from CO<sub>2</sub> and O<sub>2</sub>.

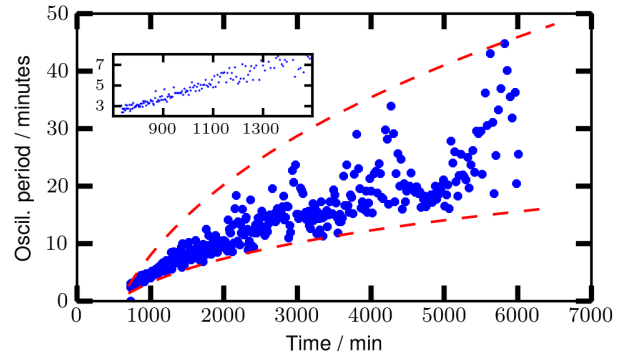
consistent dependency on oscillation frequency and duty cycle was found that could be attributed to the size of the particles.

The oscillations on all samples are qualitatively similar but the oscillation period varies from a few seconds (the time-constant of the reactor is  $\sim 7$  s) up to more than an hour. Once a sample starts to oscillate it will perform self-sustained oscillations for as long as the experiment is allowed to run. We have not observed a single sample stop oscillating once the self-sustained oscillations had started.

An example of a single very slow oscillation is seen in Figure 2. After a short on-cycle (at  $\sim 1030$  min) where all CO is converted to CO<sub>2</sub> (notice the CO signal does not go to zero due to the cracking pattern of CO<sub>2</sub> and CO background in the QMS) the reaction shows a fast deactivation. After the deactivation the sample quickly regains  $\sim 30\%$  conversion (at  $\sim 1040$  min). Hereafter the conversion increases slowly over time until approximately 50% conversion is reached (at  $\sim 1118$  min). Shortly after reaching 50% conversion the sample again ignites and converts all CO to CO<sub>2</sub>. After a short full conversion period the sample again deactivates and the cycle repeats itself.

After prolonged measurements over several days an increase in oscillation period was observed as shown in Figure 3. Initially, the oscillation period is  $\sim 2.5$  min and increases linearly with time until 1500 min of total oscillation time. Here-

after the oscillations become more irregular as shown in Figure 4 and in the lower panel of Figure 3. At experiment end the oscillation period is between 20 and 45 min.



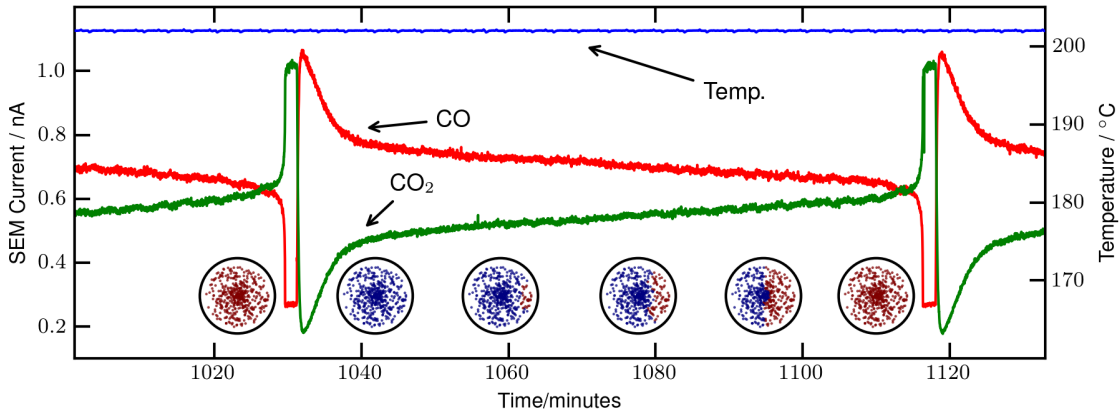
**Fig. 3** Summary of the oscillation period as a function of time for a sample oscillating under constant temperature, pressure and reactant composition. The sample went through a total of 439 oscillations in 4 days. Time is defined from experiment start and hence includes initial treatment. The inset shows the initial steady increase in oscillation period. The red lines indicate max and min oscillation time to guide the eye.

Figure 4 shows extracts of mass spectrometry data of oscillations extracted from the same four days measurement. Data from shortly after the initial treatment, after 2800 min of oscillation time and after 5900 min are shown. After 5900 min the oscillations are more irregular which is consistent with the data shown in Figure 3. Also, oscillations in between full conversion oscillations with smaller amplitude and much higher frequency than the full on-off cycles become more visible as time progresses.

The oscillation frequency becomes more irregular with progressing experiment time as shown in Figure 4. However, the ratio between CO and CO<sub>2</sub> integrated over a full period remains constant throughout the entire experiment time, i.e. the samples maintains a constant average rate independent of oscillation frequency.

A very strong temperature dependence on the oscillation frequency was also found as shown in Figure 5. By changing the temperature 5°C the oscillation period was changed by more than a factor of 10. The magnitude of the change is not completely consistent across all measured samples but all samples show a very large temperature dependency where in some cases a provoked small change in temperature will consistently turn on and off the oscillations. This is illustrated in the supplementary material, Figure S4.

The pressure dependence of the oscillations was also investigated. In the pressure range of 0.1 bar to 1 bar no change of the oscillation frequency or qualitative behavior that could be



**Fig. 2** A full oscillation period first showing a steep ignition of the sample followed by an almost immediate deactivation. For the next 65 minutes the sample slowly recovers activity until full conversion is reached again and the cycle repeats itself. This extremely long oscillation period is not commonly seen and was a result of careful parameter tuning. Typical oscillation periods are normally between  $\sim 30$  s and  $\sim 30$  min. Inserted circles illustrates the proposed model. At high conversion the platinum is oxidized (red) while in low conversion the sample is reduced (blue).

attributed to the pressure was found. Similarly, only a weak dependence on the CO/O<sub>2</sub> ratio was observed. At a CO/O<sub>2</sub> ratio of  $\sim 0.025$  only very small amplitude oscillations were observed. Increasing the CO/O<sub>2</sub> ratio showed clear oscillations with a significant increase in oscillation amplitude compared to lower CO concentrations. Generally, a tendency towards longer oscillation periods for higher CO/O<sub>2</sub> ratio was observed. Richer CO mixtures than 0.175 did not produce any oscillations in our system.

Although oscillations have previously been observed on extended Pt thin films<sup>5</sup> as well as single crystals<sup>10</sup> at atmospheric pressure no oscillations could be provoked on thin films of comparable geometrical coverage to the nanoparticles in our system at any CO/O<sub>2</sub> ratio.

#### 4 Discussion

Due to the long timescales between full conversion and low conversion plateaus the oscillations cannot be attributed to the reactor setup itself which due to its small size has timescales on the order of seconds. Furthermore, a series of experiments was performed to exclude the oscillations as an instrumental artifact. Firstly, experiments were performed on a reactor with five times larger volume and thus five times increased residence time in the reactor. Secondly, the oscillations were reproduced on a comparable but not identical setup. Finally, attempts at reproducing the phenomenon on Pt-thin films of comparable coverage did not produce any oscillations. All of

these experiments suggest that the oscillations is a property of the Pt nanoparticles.

It has previously been shown using STM<sup>11</sup>, FT-IR<sup>6</sup>, Monte Carlo simulations<sup>12</sup> as well as DFT<sup>13</sup> that the activity of Pt towards CO oxidation at atmospheric pressures is highly dependent on the oxidation state of the surface. A detailed proposal for the reaction mechanism on Pd has been developed by Hendriksen *et. al.*<sup>3</sup> and our data is consistent with this model.

According to the proposed model in ref. 3 the bare metal surface is less active than the oxidized surface. Oscillations originate from a switch between an oxidized surface and the bare metal surface. Initially, with CO present in the inlet gas a smooth metal surface is exposed due to the general high adsorption energy of CO on metal surfaces. As the Pt nanoparticles convert the CO to CO<sub>2</sub> the partial pressure of CO will decrease and a Pt oxide will start to form in the high partial pressure of O<sub>2</sub> thus increasing the rate. The model<sup>3</sup> suggests that the oxidized nanoparticles will roughen during CO oxidation resulting in the formation of an increasingly rough oxide surface. As the oxide becomes rougher the bare metal surface is increasingly favored resulting in a return to the lower rate rough metal state. As the rate decreases the CO partial pressure increases which results in a transition from rough metal surface to a smooth metal surface. When the sample is sufficiently smooth it will again oxidize and thus complete the oscillation cycle.

In this study Pt nanoparticles were investigated which, compared to a single crystal or a thin film, have a very rough surface. It is to be expected that the particles will initially favor

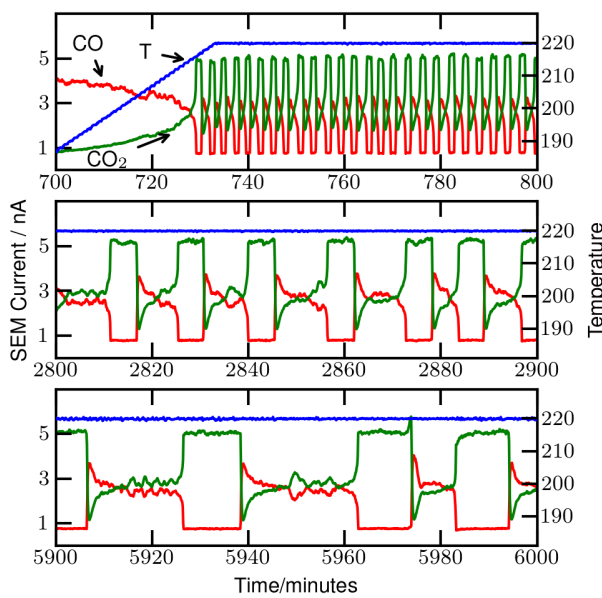


**Fig. 4** Extracts from the 4 days long experiment. The oscillation period becomes more irregular with time while the total integrated conversion remains constant. Furthermore, small oscillations in between full conversion cycles become more prominent as time progresses.

the reduced state. As the reaction runs the gas composition towards the outlet of the reactor will become more oxidizing increasing the oxidation rate of the particles (illustrated in the bottom of Figure 2). Gradually, as the particles toward the outlet oxidizes the turn-over will increase and the general CO concentration will decrease promoting more and more particles to oxidize which will gradually be seen in the QMS as an increase in  $\text{CO}_2$  and a decrease in CO. As the CO concentration decreases the light-off temperature will decrease hence approaching the constant temperature of the sample resulting in a steep increase in reactivity. It is important to note that the fraction of oxidized particles needed to achieve full conversion is not known. We are currently investigating new methods for gaining insight into the nature of the nanoparticles in the reactor but the low coverage and the design of the reactor makes this a challenging task. If all particles are not oxidized at light-off they will now oxidize much faster due to the low CO-concentration. The further increased rate will not be visible in the QMS since the reactor is already in full conversion. As most of the particles are now oxidized they will become more and more roughened and gradually return to the reduced state. Fewer and fewer oxidized particles will be responsible for the activity increasing the roughing rate of the remaining

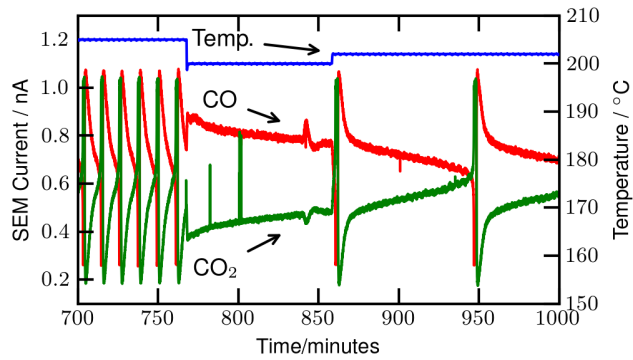


**Fig. 5** Illustration of the strong temperature dependence of the oscillation period. After about 10 hours of steady oscillations at 205°C the temperature is lowered by 5°C immediately decreasing the oscillation frequency. The temperature is hereafter increased by 2°C resulting in an increase in oscillation frequency. At 205°C the oscillation period was approximately 500 s while the oscillation period at 203°C is approximately 5000 s.

active particles. Just before the overall activity drops only a fraction of the particles participates in the reaction and the deactivation will happen very suddenly. Once these potentially few particles eventually becomes sufficiently rough they will reduce and lose activity hence completing the oscillation cycle. It should be noted that our group has recently measured turnover frequencies of CO oxidation on Pt of almost  $10^5 \text{ s}^{-1}$  per site corresponding to as little as  $\sim 50000$  Pt nanoparticles contributing to the reactivity just before the end of the high-activity cycle. This corresponds to an area of  $\sim 0.5 \text{ ppm}$  of the reactor area suggesting that in situ studies become challenging as such a minority of the reactor volume could account for all the reactivity. Attempts to see any thermal signal from such small areas has so far been in vain.

The oscillation period increases with time and becomes increasingly less stable as shown in Figure 4. This phenomena is consistent across all measured samples. The large scatter in oscillation period can be attributed to the smaller oscillations in between on/off cycles. Occasionally, these small amplitude oscillations will trigger a full switch thus introducing more short-period oscillations despite the trend of increasingly longer oscillation period. A possible explanation of the phenomenon could be sintering of the particles during the oxidation and reductions cycles. However, since the average conversion integrated over full oscillation periods is constant we do not expect sintering to be the cause since an average loss in activity of the sample would then be expected.

Oscillations were only seen in  $\text{CO}/\text{O}_2$  ratio below 0.175. This ratio agrees well with literature<sup>5,10</sup> where oscillations have been observed in oxygen rich  $\text{CO}/\text{O}_2$  mixtures. The

---

needed low concentration of CO in the inlet gases can be attributed to the much higher sticking coefficient of CO on Pt which poisons the nanoparticle surface during the low reactivity region of the cycle.

Nanoparticles of several different sizes were tested and all showed oscillations. However, no change in duty cycle or frequency that could be attributed to the size of the nanoparticles was found. This may be due to the fact that even nominally identical samples also show a large variation in oscillation frequency and duty cycle thus possibly shadowing a nanoparticle size effect.

An interesting feature in the data is the very large temperature dependence of the oscillation frequency. This property agrees well an earlier suggested model<sup>3</sup> and it is, to our knowledge, the first time the temperature dependence of oscillations at atmospheric pressure has been measured.

## 5 Conclusion

Self-sustained CO oxidation oscillations at atmospheric pressure on Pt nanoparticles ranging from 3 nm to 9 nm in diameter have been measured with high-quality mass-spectrometry. It was found that the samples increased the oscillation period over time and showed a strong temperature dependence of the oscillation period. A model is proposed where the nanoparticles go through repetitive oxidation/reduction cycles which change the change rate of CO oxidation on the particles. The fact that extremely few nanoparticles may account for the activity make in situ investigations a challenge.

## 6 Acknowledgments

This work was carried out as part of the Catalysis for Sustainable Energy Initiative, which is funded by the Danish Ministry of Science, Technology and Innovation. The Center for Individual Nanoparticle Functionality is funded by the Danish National Research Foundation.

## References

- 1 G. Ertl, *Angewandte Chemie-international Edition*, 2008, **47**, 3524–3535.
- 2 B. C. Sales, J. E. Turner and M. B. Maple, *Surface Science*, 1982, **114**, 381–394.
- 3 B. L. M. Hendriksen, M. D. Ackermann, R. van Rijn, D. Stoltz, I. Popa, O. Balmes, A. Resta, D. Wermeille, R. Felici, S. Ferrer and J. W. M. Frenken, *Nature Chemistry*, 2010, **2**, 730–734.
- 4 C. D. Lund, C. M. Surko, M. B. Maple and S. Y. Yamamoto, *Surface Science*, 2000, **459**, 413–425.
- 5 J. Singh, M. Nachtegaal, E. M. C. Alayon, J. Stotzel and J. A. van Bokhoven, *Chemcatchem*, 2010, **2**, 653–657.
- 6 P. A. Carlsson, V. P. Zhdanov and M. Skoglundh, *Physical Chemistry Chemical Physics*, 2006, **8**, 2703–2706.
- 7 T. R. Henriksen, J. L. Olsen, P. Vesborg, I. Chorkendorff and O. Hansen, *Review of Scientific Instruments*, 2009, **80**, 124101.
- 8 R. M. Nielsen, S. Murphy, C. Strebel, M. Johansson, J. H. Nielsen and I. Chorkendorff, *Surface Science*, 2009, **603**, 3420–3430.
- 9 P. C. K. Vesborg, J. L. Olsen, T. R. Henriksen, I. Chorkendorff and O. Hansen, *Review of Scientific Instruments*, 2010, **81**, 016111.
- 10 B. L. M. Hendriksen, S. C. Bobaru and J. W. M. Frenken, *Catalysis Today*, 2005, **105**, 234–243.
- 11 B. L. M. Hendriksen and J. W. M. Frenken, *Physical Review Letters*, 2002, **89**, 046101.
- 12 V. P. Zhdanov and B. Kasemo, *Surface Science*, 2002, **513**, L385–L390.
- 13 X. Q. Gong, R. Raval and P. Hu, *Physical Review Letters*, 2004, **93**, 106104.

---

# Self-sustained carbon monoxide oxidation oscillations on size-selected platinum nanoparticles at atmospheric pressure

## - Supplemental Material

### 1 The $\mu$ -reactor platform

The experiments were performed in Si-based 20x16 mm  $\mu$ -reactors<sup>1</sup>. The reactor consists of two inlets, a mixing zone allowing for diffusional mixing of reactants, an outlet, a reactor volume of 240 nL and a 5.4  $\mu$ m wide, 3  $\mu$ m high and 1500  $\mu$ m long capillary used for sniffing gases from the reactor volume. The reactor is sealed by anodic bonding of a pyrex lid to the Si reactor and is able to operate in a pressure range of 0–2.5 bar. The reaction gases are supplied to the two inlets by flow controllers capable of controlling the gas flow from 0–10 mL/min. The capillary flow is fed into a quadrupole mass-spectrometer (QMS) for analysis while any surplus of gas from the inlets is passed directly through to the outlet via a pressure controller allowing control of reactor pressure. The design makes sure that all gases exposed to the catalyst under investigation are measured by the QMS ensuring an extremely high sensitivity of the system.

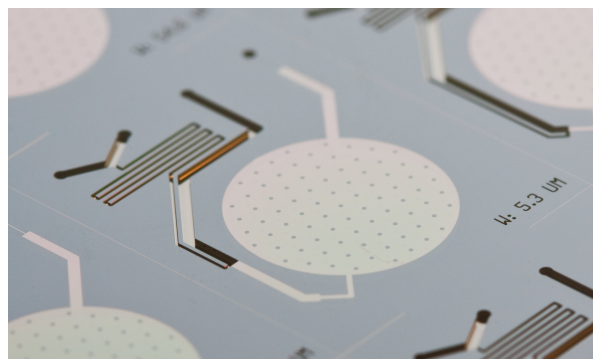


**Fig. S1** Image of the 20x16 mm microreactor showing the circular reactor area and gas channel system

Before any measurements are performed the reactor is pumped by a turbopump to minimize contaminants in the system. When an evacuated reactor is mounted the base pressure of the mass spectrometer chamber is  $\sim 5 \times 10^{-9}$  mbar and in operation at 1 bar in the reactor volume the pressure is  $\sim 5 \times 10^{-7}$  mbar in the QMS chamber.

The reactor is heated by joule heating of a Pt strip evaporated on the backside of the reactor chip. The introduction of two additional contacts on the backside of the reactor allows for 4 wire measurements of the resistance of the Pt strip using it as a RTD for temperature measurement of the reactor. An external thermocouple acts as room-temperature calibration of the RTD as well as sanity check of the RTD measurement

during operation. The measured RTD temperature is always compared to the thermocouple at room temperature both before and after an experiment to be sure the RTD did not change resistance due to annealing during the experiment.

The gas handling including flow and pressure controllers and the mass spectrometer is fully automated allowing for measurements during several days without human intervention allowing for self-consistent measurements of many samples.

### 2 Pt nanoparticle deposition

Pt nanoparticles were deposited in the reactor using a gas-aggregation source (Mantis Deposition Ltd., Nanogen 50). Pt clusters were formed by gas-phase condensation of Pt atoms produced by impinging argon ions on a 99.99% Pt target in a magnetron sputter source. After condensation the ionised fraction (60–80%) of the clusters were size-selected by a quadrupole mass selection filter according to their mass-to-charge ratio. Using this setup Pt nanoparticles with diameters in the range of 2–16 nm can be produced<sup>2,3</sup>. The size-selected nanoparticles were after size-selection soft-landed in the reactor volume of the microreactor. The coverage was kept at approximately 0.1% geometric coverage determined by measuring the current on the reactor during deposition. After deposition the reactors were anodically cold-bonded<sup>4</sup> to a pyrex lid to avoid sintering of the nanoparticles while bonding.

### 3 CO concentration dependence

The dependence of the CO concentration on the period of the oscillations was investigated. The result shows that the period increases slightly with increasing CO-concentration. However, the effect is small compared to the general trend of slower oscillations as the experiment progresses. In Figure S2 the oscillation periods are summarized and the actual massspectrometry data of the entire experiment is shown in Figure S3.

### 4 Temperature dependence

As mentioned in the main paper, the oscillations shows a very strong temperature dependence. In Figure S4 we show an example where the oscillations are turned on and off by changing the temperature 20°C.

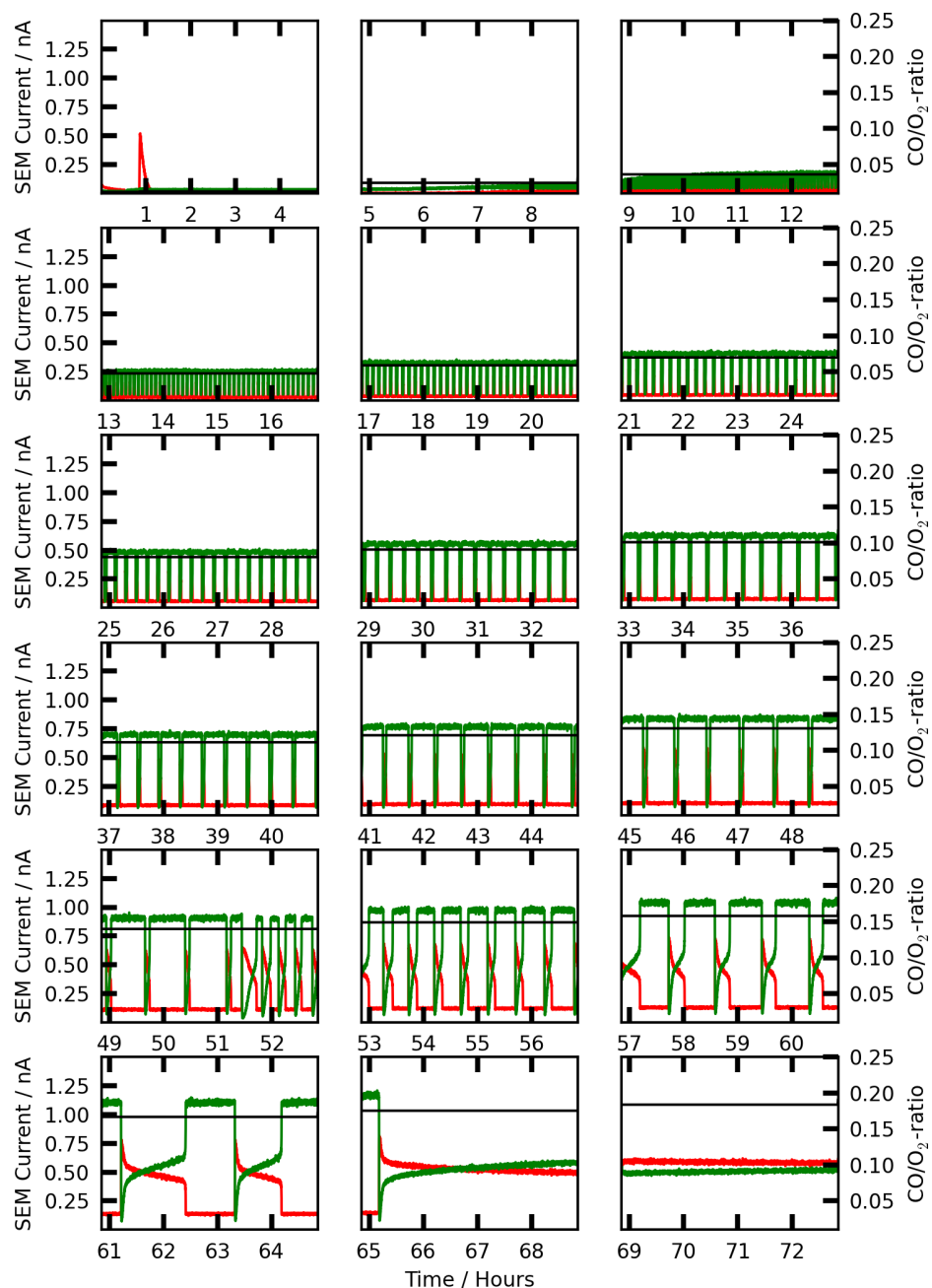


**Fig. S3** Complete series of data from an oscillating sample, showing CO (red) and CO<sub>2</sub> (blue). The temperature is constant at 210°C during the entire measurement. For every frame the CO-concentration is increased.

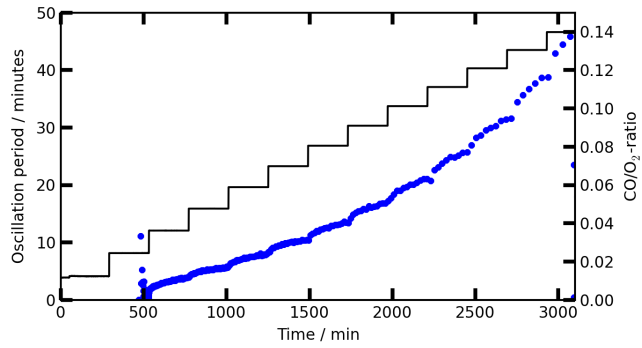


**Fig. S2** Oscillation period (blue) as a function of time and CO concentration (black). The overall trend of increasing oscillation period with time is superimposed with small discontinuous steps when the CO concentration is increased.

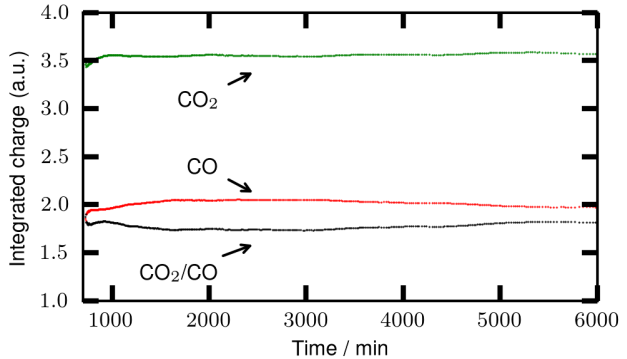


**Fig. S5** Running average of the CO and CO<sub>2</sub> concentrations and their ratio during a 4-day long experiment. The individual data-points is calculated as the integral of CO (red) or CO<sub>2</sub> (green) during the individual oscillation periods. The ratio between CO and CO<sub>2</sub> is drawn in black.

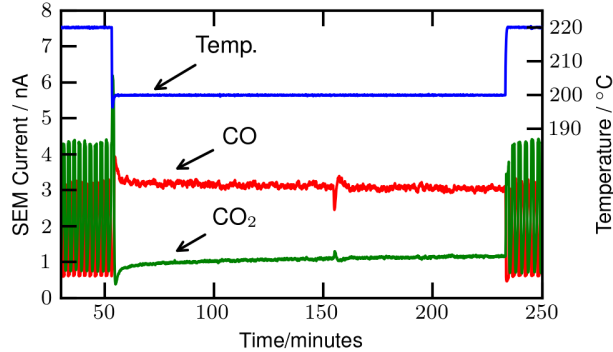


**Fig. S4** Another example of the very pronounced temperature dependence.

## 5 Duty cycle

Even though the period of the oscillations increases with time, the total integrated conversion rate during a complete cycle is almost constant. In Figure S5, the value of the mean value of CO and CO<sub>2</sub> is plotted for every oscillation in the four-day long experiment. It is evident that the ratio between CO and CO<sub>2</sub> is almost constant and thus the average activity of the sample is almost unchanged despite the development in the oscillation frequency.

## References

- 1 T. R. Henriksen, J. L. Olsen, P. Vesborg, I. Chorkendorff and O. Hansen, *Review of Scientific Instruments*, 2009, **80**, 124101.
- 2 R. M. Nielsen, S. Murphy, C. Strelbel, M. Johansson, I. Chorkendorff and J. H. Nielsen, *Journal of Nanoparticle Research*, 2010, **12**, 1249–1262.

- 3 R. M. Nielsen, S. Murphy, C. Strelbel, M. Johansson, J. H. Nielsen and I. Chorkendorff, *Surface Science*, 2009, **603**, 3420–3430.
- 4 P. C. K. Vesborg, J. L. Olsen, T. R. Henriksen, I. Chorkendorff and O. Hansen, *Review of Scientific Instruments*, 2010, **81**, 016111.

**Paper 2**

**High Mass Resolution Time of Flight Mass Spectrometer for Measuring Products in Heterogeneous Catalysis in Highly Sensitive Microreactors**

Accepted for publication in Review of Scientific Instruments

# High Mass Resolution Time of Flight Mass Spectrometer for Measuring Products in Heterogeneous Catalysis in Highly Sensitive Microreactors

T. Andersen,<sup>1</sup> R. Jensen,<sup>1</sup> M.K. Christensen,<sup>1</sup> T. Pedersen,<sup>2</sup> O. Hansen,<sup>2</sup> and I. Chorkendorff<sup>1, a)</sup>

<sup>1)</sup>*Department of Physics, Danish National Research Foundation's Center for Individual Nanoparticle Functionality (CINF), Technical University of Denmark, Building 312, DK-2800 Kgs. Lyngby, Denmark*

<sup>2)</sup>*Department of Micro- and Nanotechnology, Technical University of Denmark, DTU Nanotech Building 345 East, DK-2800 Kgs. Lyngby, Denmark*

(Dated: 24 April 2012)

We demonstrate a combined microreactor and time of flight system for testing and characterization of heterogeneous catalysts with high resolution mass spectrometry and high sensitivity. Catalyst testing is performed in silicon-based microreactors which have high sensitivity and fast thermal response. Gas analysis is performed with a time of flight mass spectrometer with a modified nude Bayard-Alpert ionization gauge as gas ionization source. The mass resolution of the time of flight mass spectrometer using the ion gauge as ionization source is estimated to  $m/\Delta m > 2500$ . The system design is superior to conventional batch and flow reactors with accompanying product detection by quadrupole mass spectrometry or gas chromatography not only due to the high sensitivity, fast temperature response, high mass resolution and fast acquisition time of mass spectra but it also allows wide mass range (0–5000 amu in the current configuration). As a demonstration of the system performance we present data from ammonia oxidation on a Pt thin film showing resolved spectra of OH and NH<sub>3</sub>.

---

<sup>a)</sup>[ibchork@fysik.dtu.dk](mailto:ibchork@fysik.dtu.dk)

## I. INTRODUCTION

In heterogeneous catalysis optimization and development of analytic equipment is important both to minimize the cost of equipment but also to be able to experimentally study complicated systems. As a platform for testing heterogeneous catalysts microfabricated reactors or microreactors have been found suitable due to both high surface-to-volume ratio, fast temperature response and minimization of thermal and concentration gradients<sup>1,2</sup>. Such a platform has been developed to test and characterize model catalysts in our department<sup>3</sup>. However, a suitable reactor platform is only part of the task; reactant and product detection and characterization is essential to determine catalyst performance. Typically, quadrupole mass spectrometers (QMSs) are used in low pressure regimes to analyze gas composition while gas chromatographs (GCs) are used for high pressure measurements. The QMS, however, suffers from a low mass resolution ( $m/\Delta m \gtrsim m$  up to  $m \sim 200$ ) which makes analysis of complicated spectra difficult and cumbersome. Furthermore, QMSs are typically operated by logging a single (or a few) masses as a function of time to increase time resolution. This is at the expense of acquisition of full mass spectra during the experiment limiting operation by potentially losing interesting features in other masses not monitored. GCs have inherently low time resolution which make them unsuitable for fast time response measurements as in the case of microreactors and are in general difficult to use as mass spectrometers due to the difficult interpretation of measurements on complex mixtures. Furthermore, GCs only sample a very small part of the converted gas making them unsuitable for small amounts of reactant and product gases due to the low sensitivity. As an alternative to GCs or QMSs time of flight mass spectrometers (TOF-MS) offer both high mass resolution ( $m/\Delta m > 1000$ ), fast acquisition of full mass spectra ( $>1\text{ Hz}$ ) and high sensitivity making them suitable for characterization of very small amounts of catalyst, i.e. model systems, and a mass range only limited by the detector. With a standard available microchannel plate (MCP) used as detector a mass range of 0–5000 amu can be obtained.

Typically, TOF-MS in heterogeneous catalysis is used as a surface analytic tool, i.e. TOF-SIMS<sup>4–7</sup>. Measurements of reactants and products on heterogeneous catalysts by TOF-MS have previously been performed<sup>8,9</sup> but, until now, to our knowledge, the testing of catalysts in a microreactor with subsequent gas analysis by a TOF-MS has not been demonstrated. Here we describe a microreactor and TOF-MS system which combines the high sensitivity

of microreactors and the high mass resolution TOF-MSs for testing and characterizing of heterogeneous catalysts.

## II. SYSTEM DESIGN

The setup consists of three main components. The microreactor, where the catalyst under investigation is deposited, an ionization source which ionizes the gas from the microreactor and a TOF-MS used for gas analysis. In addition a QMS is connected to the capillary of the microreactor which enables direct comparison between the QMS and TOF-MS.

The catalyst under investigation is deposited in the microreactor reactor volume by e.g. evaporation<sup>3</sup>, drop casting<sup>10</sup> or gas aggregation formed size-selected nanoparticles. The gas composition in the microreactor reactor volume is ionized by the modified ion gauge and is subsequently focused by the Einzel lenses into the source region. From the source region the ions are pushed into the flight tube by a repelling voltage pulse and is after mass separation in the flight tube detected by a MCP. A schematic of the entire setup is shown in Figure 1.

### A. The microreactor platform

Catalyst characterization and performance evaluation is performed in a microreactor<sup>3</sup>. The microreactors are silicon-based and measures 20x16 mm. The reactor consists of two gas inlets, a gas outlet, a reactor volume and a capillary used to restrict the gas flow from the reactor volume. The reactor volume is  $3\text{ }\mu\text{m}$  deep and 1 cm in diameter corresponding to a 236 nL volume. The diffusion length of the reactants and products gases in the microreactor reactor volume is almost an order of magnitude longer than the radius of the reactor volume ensuring full contact of the gas with the catalyst. This has been proven to hold by reproducible CO oxidation measurements on small Pt spots located at different points in the the reactor volume. The two gas inlets are combined on the chip where the inlet gases mix by diffusion. The capillary is designed such that approximately  $3 \times 10^{14} \text{ molecules}\cdot\text{s}^{-1}$  are probed from the reactor volume when operated at 1 bar. Any surplus of gas from the two inlets that does not enter the reactor volume is directed through an outlet to a turbo pump. The design ensures that all molecules or atoms entering the reactor volume, and hence exposed to the catalyst under investigation, are detected by mass spectrometry ensuring high

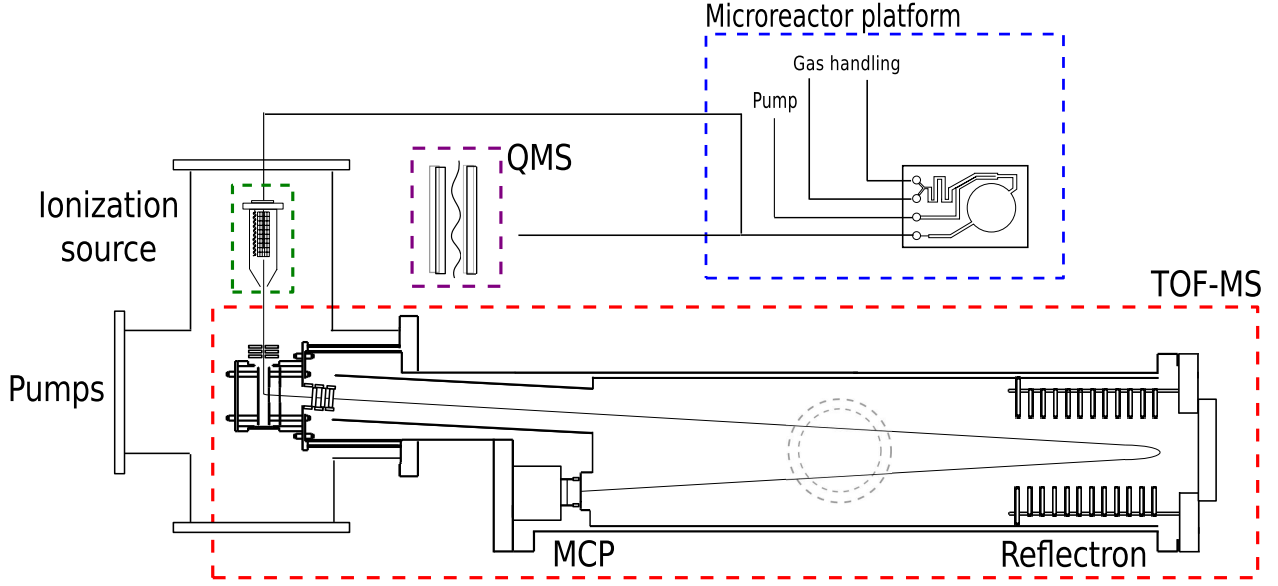


FIG. 1. Schematic of the total system (not to scale). The capillary outlet from the microreactor can be directed to either a QMS or the TOF-MS. For measurements by the TOF-MS the gas is fed into a modified ion gauge which ionizes the gas. The ionized gas hereafter enters the TOF-MS through a series of Einzel lenses from where they are pushed into the flight tube by a repelling voltage,  $V_p$ . Ions are separated in the field free region and focused by the reflectron. The ions are subsequently detected by the MCP.

sensitivity. This feature makes the microreactors especially well suited for characterization of model systems where small amounts of catalyst are typically used.

The microreactor is heated by joule heating of a 100 nm platinum strip (on top of a 3 nm Ti adhesion layer) evaporated through a shadow mask on the backside of the chip . The heating element is contacted by two pogo pins which are connected to a power supply. Two additional contacts are placed on the chip facilitating a 4 wire measurement of the resistance of the heating element. The heating strip can in this way be used as a resistance temperature detector (RTD) to determine the temperature of the chip. Currently, temperatures from room temperature to approximately 450 °C can be reached due to apparatus limitations. The high temperature limit is expected to be ~ 600 °C where the pyrex lid used for sealing the reactor will melt.

## B. Gas handling for the microreactor

The two gas inlets on the microreactor chip are connected to a macroscopic gas handling system which is constructed entirely from UHV compatible elements to ensure extremely clean gas handling. A total of 6 gases with accompanying flow controllers are used to control the inlet gas flow to the microreactor. Currently, the system is configured in a 4+2 setup where 4 gases are connected to the first inlet and two gases connected to the secondary inlet. At the time of writing He, CO, O<sub>2</sub>, CH<sub>4</sub>, NH<sub>3</sub> and H<sub>2</sub> are connected to the setup. All gases used on the setup are N6 quality gases, i.e. 99.9999 % purity. All valves and flow controllers are interfaced to a computer enabling remote control of the system and the ability to run experiments over several days without human intervention.

## C. Time of flight mass spectrometer

The time of flight chamber is pumped by a turbo pump and two ion pumps. A 120 l/s ion pump is used to pump the flight tube while a 400 l/s ion pump and a 450 l/s turbo pump are used to pump down the source region which is mounted on a 8" 4-way cross. Opposite to the source region of the TOF-MS the pumps are mounted while the two remaining flanges are occupied by the ionization gauge and a blanked flange (see Figure 1). While idling the pressure in the source region is  $\sim 1 \times 10^{-9}$  mbar and  $\sim 2 \times 10^{-9}$  mbar in the flight tube.

The time of flight equipment used for detection of gas molecules flown through the capillary of the microreactor is designed as an orthogonal mass spectrometer and is assembled from modules purchased from Jordan TOF Products, Inc.<sup>11</sup>.

Ions enter the source region of the TOF-MS through a series of entry Einzel lenses used for focusing the beam hence minimizing divergence. In the source the beam is pushed into the flight tube by an initial repelling push voltage,  $V_p$ . The ions are hereafter further accelerated from ground potential to the liner potential,  $V_L$ . Using this setup the drift velocity of an ion starting exactly from the center of the acceleration region corresponds to an energy of  $Ze(V_L + V_p/2)$  where  $Ze$  is the charge of the ion. At the end of the flight tube a reflectron is installed. The reflectron is controlled by voltages  $V_{R1}$  and  $V_{R2}$ . The reflectron has two primary purposes: i) The effective drift length is increased hence increasing the resolution of the TOF-MS. ii) The reflectron works as a focusing lens (cf. Figure 2) compensating

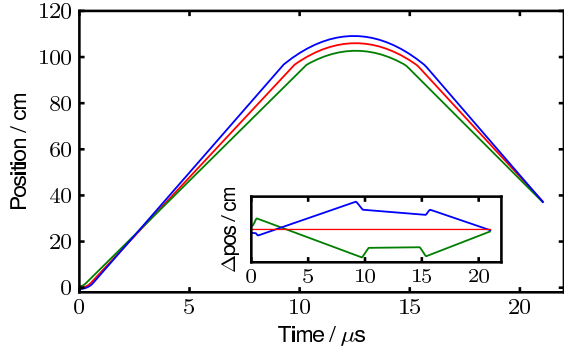


FIG. 2. Simulated trajectories of ions ( $m/q = 50$ ) with initial position variations in the source region illustrating the focusing effect of the reflectron. Red curve corresponds to ions with an initial position in the center of the source region while blue and green curves illustrate trajectories of ions with non-ideal initial positions displaced 6.3 mm towards and further away from the repelling plate, respectively. Insert shows the difference between displaced ions and the center positioned ion. The models does not include initial velocity dispersion of the ions.

for any initial velocity dispersion of the ions, i.e. ions with an initial higher velocity will have an increased flight length compared to slower ions. The MCP used for ion detection is placed in the focal point of the reflectron giving maximum compensation for initial velocity dispersion. According to the manufacturer a resolution  $m/\Delta m \gtrsim 4000$  of the TOF-MS has been shown.

The prize of the TOF including ionization gauge, 8" 4-way cross, control electronics, data acquisition hardware and MCP detector is comparable to the prize of a high quality QMS with electronics making the TOF-MS a serious alternative to a QMS.

In Figure 3 an example spectrum of ammonia oxidation ( $\text{NH}_3:\text{O}_2$  4:3, 195 °C) is shown. Here the high resolution of the TOF-MS is demonstrated by resolving ammonia ( $\text{NH}_3$ ) and hydroxyl ( $\text{OH}$ ) which have a mass difference of 23 milli-amu.

### 1. Gas ionization

As ionization source of the gas flow from the microreactor capillary a modified nude UHV Bayard-Alpert ion gauge is used. A current of approximately 3 A is run through the filament resulting in 10 mA emission current. The grid is biased approximately 40 V

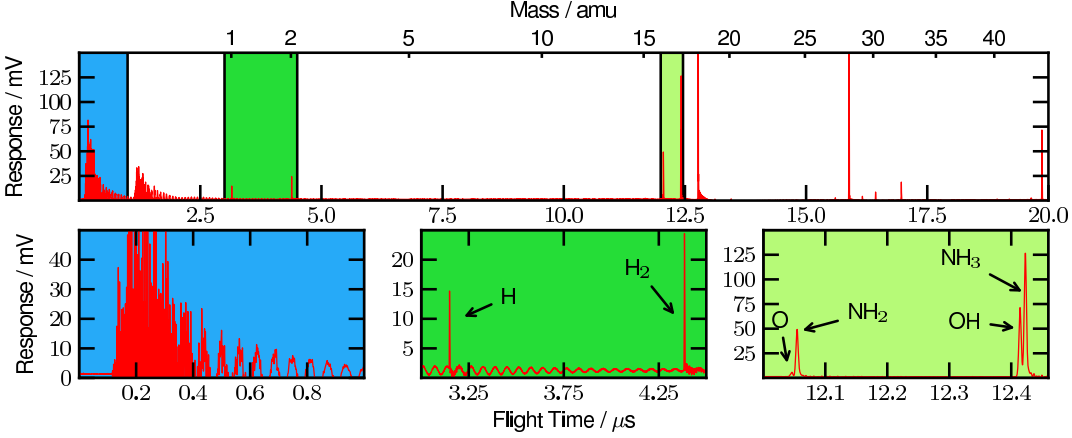


FIG. 3. Raw data acquired from the TOF-MS during  $\text{NH}_3$  oxidation by  $\text{O}_2$  ( $\text{NH}_3:\text{O}_2$  4:3,  $195^\circ\text{C}$ ). Subfigures show three different regions of the spectrum. From the first subfigure in the lower panel a delay between the acquisition trigger and the noise signal from the rise of the high voltage pulser of approximately 150 ns can be seen. This is due to delays in cables and the repeller pulser. In the center subfigure the extremely good separation between individual masses is shown. It is evident that 1 amu corresponds to approximately  $1.4 \mu\text{s}$  difference in flight time in our system in the mass regime around 1 amu. In the last subfigure a zoom of the ammonia and hydroxyl peaks region shows separation between OH and  $\text{NH}_3$  as well as O and  $\text{NH}_2$  (23 milli-amu mass difference).

negative compared to the filament to accelerate electrons emitted from the filament towards the grid. Contrary to standard operation of an ion gauge the collector in the center of the grid is short-circuited to the grid ensuring a homogeneous field distribution within the grid. To allow ionized ions to escape from the gauge the lid of the grid has been removed. Using this configuration approximately half of the ionized ions are expected to leave the ionization gauge<sup>12</sup>. The entire construction is placed in a flange with a small orifice which is differentially pumped by a turbo pump. Large amounts of gas can hence be dosed locally around the ion gauge while still maintaining a low pressure in the source region of the TOF-MS. The small orifice is essential in the setup to avoid high pressure in the acceleration region and drift tube of the TOF-MS which would cause an increase in dead counts on the MCP thus decreasing the signal-to-noise ratio of the recorded signal.

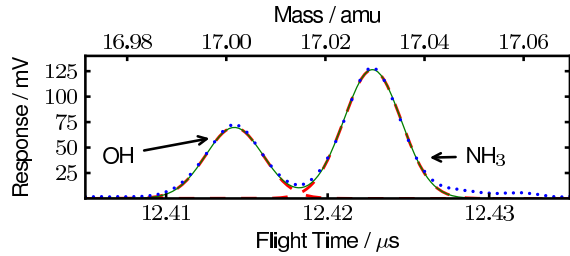


FIG. 4. Example of two gaussian fits (dashed red lines) and the sum of the two fits (green solid line) to a double peak (blue dots) consisting of NH<sub>3</sub> and OH both at approximately 17 amu demonstrating the resolution of the TOF-MS. The entire graph section represents a mass difference of 100 milli-amu.

## 2. Data treatment

Raw data plotted with accompanying gaussian fits are shown in Figure 4. Here the closely lying peaks from OH due to cracking of both residue water and water as reaction product and uncombusted NH<sub>3</sub> is shown. The ability to separate these contributions substantially simplifies quantification of ammonia and allows for easier characterization of catalyst performance.

In Figure 5 raw data from water, hydrogen and oxygen from three different regions are shown illustrating the dynamic range of the TOF-MS. At constant MCP voltage all the peaks are clearly visible although the ratio of the oxygen to water amplitude is  $\sim 400$ . In reality the dynamic range is limited mostly by the data acquisition hardware as well as the quality of the ion source. Even with the home-built ionization source and a 8-bit digitizer the dynamic range is, from Figure 5, estimated to  $\sim 1000$  using an integration time of  $\sim 5$  s. The dynamic range of the TOF-MS is hence comparable to the dynamic range offered by a QMS at constant preamplifier range while covering a much larger mass range. The TOF-MS, however, acquires mass spectra (0–5000 amu) at high frequency ( $> 1$  Hz) which is impossible with a QMS where only a few masses can be followed as a function of time to increase time resolution. The possibility of fast acquisition of complete mass spectra by the TOF-MS thus ensures that all masses are monitored simultaneously during the experiment. The problem of selecting appropriate masses for logging by the QMS is hence eliminated.

Since the TOF-MS only measures flight time and not the actual mass of the measured ions it is necessary to determine the relationship between flight time and actual mass. This

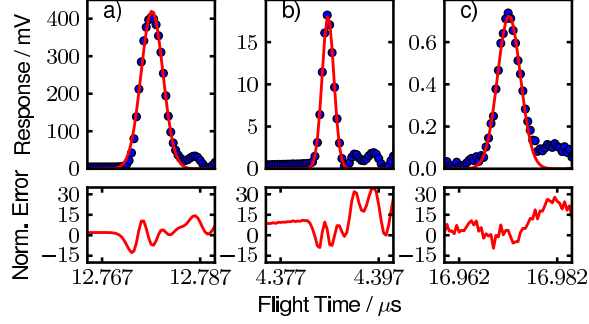


FIG. 5. Gaussian fits (red solid line) to three different mass to charge ratios (blue points) from the same mass spectrum. In panels a), b) and c) the  $\text{H}_2\text{O}$  (peak area:  $2.35 \text{ mV}\cdot\mu\text{s}$ ),  $\text{H}_2$  (peak area:  $5.43 \times 10^{-2} \text{ mV}\cdot\mu\text{s}$ ) and  $\text{O}_2$  (peak area:  $4.24 \times 10^{-3} \text{ mV}\cdot\mu\text{s}$ ) signals are shown, respectively. As seen from the response a high dynamic range of the TOF-MS is demonstrated by good gaussian fits to all peaks. The TOF-MS can hence be used to monitor both very small and very large signal masses. At the bottom panel the area normalized error for each fit shows that the relative fit error is independent of the total peak area.

can be done by calibration masses expressing known patterns in the mass spectrum. In this way masses can be reasonably well determined with subsequent fitting of these values to get an expression for the flight time as a function of mass. This approach is in some cases adequate but has the significant drawback that several peaks of well known masses must be present in the flight spectrum which is not always necessarily feasible. To determine the relationship between mass and flight time we have made a numeric model of the TOF-MS which calculates the flight time based only on the voltages for the pulser,  $V_p$ , liner,  $V_L$ , and reflectron,  $V_{R1}$  and  $V_{R2}$ , and thus provides a relationship of flight time to mass. Typically, the model is used together with the experimental determination of a single mass since this will help fix the unknown delays originating from the measurement trigger, rise time of the high-voltage pulse at the repeller plate and cable delays. As seen in Figure 6 the performance of the model is good despite its simplicity giving a total error in flight time estimation of  $\sim 10 \text{ ns}$  corresponding to  $\sim 50 \text{ milli-amu}$  at 70 amu. The model is written in Python and can be acquired online<sup>13</sup>.

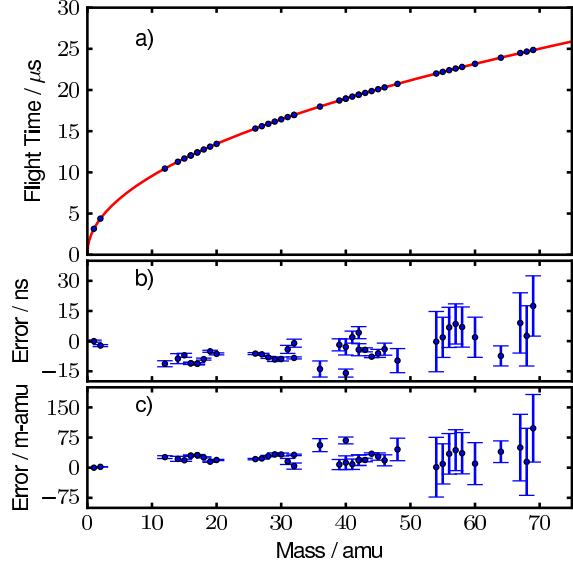


FIG. 6. Comparison of the simulated model (red curve, top panel) to actual measured experimental values (blue dots) of flight time as a function of mass. In the lower panels the difference between acquired experimental data and data calculated from the model in time and mass units are shown. Error bars represents only the uncertainty in the experimental data. As seen from the lower panels a deviation of  $\sim 10$  ns corresponding to  $\sim 50$  milli-amu at 70 amu is present.

### III. OXIDATION OF AMMONIA

To demonstrate the system capability ammonia oxidation on a 1% geometrical coverage Pt thin film has been used as test reaction. The catalytic oxidation of ammonia can proceed along primarily three different routes<sup>14</sup>.



All of these systems are difficult to analyze both qualitatively and quantitatively due to the overlap of  $\text{NH}_3$ , which is a reactant, and  $\text{OH}$  originating from cracking of  $\text{H}_2\text{O}$ , which is a product from the combustion and is a part of the residue gas. Specifically, hydroxyls ( $\text{OH}$ ) from cracking of trace water in the system and the combustion reaction and the primary

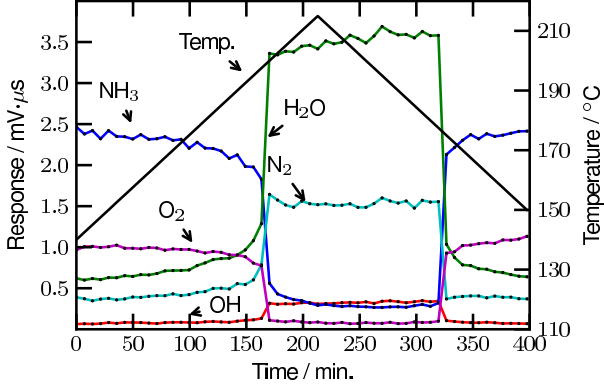


FIG. 7. Ammonia oxidation as a function of temperature on a 1% geometrical coverage Pt thin film. As the temperature is increased ammonia is oxidized to  $\text{H}_2\text{O}$  and  $\text{N}_2$ . Furthermore, the  $\text{OH}$  and  $\text{NH}_3$  signals are anticorrelated demonstrating the ability to resolve these two close lying masses as shown in Figure 4.

peak of ammonia ( $\text{NH}_3$ ) are both detected at  $m/q \simeq 17$ . Without adequate mass resolution it is not possible to separate the two contributions resulting in difficult analysis. Often a charge to mass ratio without cracking from both products and residual gas in the system is used to quantify the amount of ammonia and water. In the case of ammonia,  $m/q = 15$  or  $m/q = 8.5$  is typically chosen since water does not contribute to these masses. However, both of these masses contains only a very small fraction of the main peak since it involves either the loss of two hydrogen atoms or a double charged ammonia ion which are both formed in processes with very low yields. The measurement of these masses have a very poor signal to noise ratio making measurements on ammonia very difficult with traditional mass spectrometry methods.

At experiment start the microreactor is equilibrated with  $\text{NH}_3$  and  $\text{O}_2$  in a 4:3 ratio corresponding to stoichiometry for this reaction. After equilibration the temperature is increased in steps of  $2.5^\circ\text{C}$  from  $150^\circ\text{C}$  to  $215^\circ\text{C}$ . The gas composition in the microreactor is continuously probed by the TOF-MS which is connected to the capillary of the microreactor. In Figure 7 the integrated  $\text{N}_2$ ,  $\text{NH}_3$ ,  $\text{H}_2\text{O}$ ,  $\text{O}_2$  and  $\text{OH}$  peaks acquired from the raw TOF-MS spectrum as a function of temperature are shown. At each individual temperature step a mass scan is performed from triggering of the acceleration pulse up to  $25\,\mu\text{s}$  of flight time corresponding to 70 amu. As seen from Figure 7 the combustion of  $\text{NH}_3$  increases substan-

tially at approximately 200 °C and drops again at approximately 175 °C. The combustion of ammonia to molecular nitrogen and water in this temperature range agrees well with literature<sup>14,15</sup>.

In Figure 7 an anticorrelation between OH and NH<sub>3</sub> is seen. The inverse relation between these two masses can only be measured because these peaks are resolved in the mass spectrum. As expected a strong correlation between H<sub>2</sub>O and OH is seen as a direct result of water cracking to hydroxyls. The data shown in Figure 7 hence demonstrates the usability of the combined microreactor and TOF-MS setup especially simplifying data analysis of complicated mass spectra while maintaining a high sensitivity from the microreactor platform.

#### IV. CONCLUSION

We have demonstrated a combined microreactor and TOF-MS system which can be employed to test and characterize model heterogeneous catalysts. An automated gas handling system is used to flow gas over a catalyst in a microreactor volume from where gases can be probed. The reactor gas composition is directed through a flow restriction in the microreactor and subsequently analyzed by a TOF-MS combining high sensitivity and high mass resolution.

As a demonstration of the system performance ammonia oxidation on 1 % geometrical coverage Pt thin film was performed. The ability to resolve OH and NH<sub>3</sub> which is separated by 23 milli-amu was demonstrated. The resolution of reactants and products enables simple and straightforward quantification of the ammonia and water signals. This greatly simplifies the analysis compared to conventional QMSs used for gas analysis. The setup is furthermore superior to conventional QMSs where only a limited mass resolution at high masses can be obtained and can be applied to the study of small amounts of catalysts.

#### V. ACKNOWLEDGEMENTS

This work was carried out as part of the Catalysis for Sustainable Energy initiative, which is funded by the Danish Ministry of Science, Technology and Innovation. The Center for Individual Nanoparticle Functionality is funded by the Danish National Research

Foundation.

## REFERENCES

- <sup>1</sup>K.F. Jensen. Microreaction engineering – is small better? *Chemical Engineering Science*, 56(2):293–303, January 2001.
- <sup>2</sup>K. Jähnisch, V. Hessel, H. Löwe, and M. Baerns. Chemistry in microstructured reactors. *Angewandte Chemie International Edition*, 43(4):406–446, 2004.
- <sup>3</sup>T.R. Henriksen, J.L. Olsen, P. Vesborg, I. Chorkendorff, and O. Hansen. Highly sensitive silicon microreactor for catalyst testing. *Review of Scientific Instruments*, 80(12):124101, December 2009.
- <sup>4</sup>A. Benninghoven. Chemical-analysis of inorganic and organic-surfaces and thin-films by static time-of-flight secondary-ion mass-spectrometry (TOF-SIMS). *Angewandte Chemie-international Edition In English*, 33(10):1023–1043, June 1994.
- <sup>5</sup>F. De Smet, M. Devillers, C. Poleunis, and P. Bertrand. Time-of-flight sims study of heterogeneous catalysts based on praseodymium and molybdenum oxides. *Journal of the Chemical Society-faraday Transactions*, 94(7):941–947, April 1998.
- <sup>6</sup>J. Grams, J. Goralski, and T. Paryjczak. High resolution surface imaging of Co/ZrO<sub>2</sub> catalyst by TOF-SIMS. *Surface Science*, 549(1):L21–L26, January 2004.
- <sup>7</sup>G. E. Johnson, M. Lysonski, and J. Laskin. In situ reactivity and tof-sims analysis of surfaces prepared by soft and reactive landing of mass-selected ions. *Analytical Chemistry*, 82(13):5718–5727, July 2010.
- <sup>8</sup>E.J. Levy, E.D. Miller, and W.S. Beggs. Application of time of flight mass spectrometry and gas chromatography to reaction studies. *Analytical Chemistry*, 35(8):946–949, 1963.
- <sup>9</sup>K. Okumura, Y. Sakamoto, T. Kayama, Y. Kizaki, H. Shinjoh, and T. Motohiro. Quantitative analysis of transient surface reactions on planar catalyst with time-resolved time-of-flight mass spectrometry. *Review of Scientific Instruments*, 78(10):104102, October 2007.
- <sup>10</sup>P.C.K. Vesborg, J.L. Olsen, T.R. Henriksen, I. Chorkendorff, and O. Hansen. Gas-phase photocatalysis in mu-reactors. *Chemical Engineering Journal*, 160(2):738–741, June 2010.
- <sup>11</sup><http://www.rmjordan.com/OrthogoTOF/orthogotof.html>.
- <sup>12</sup>W.B. Nottingham. *Vacuum Symposium Transactions*. Committee on Vacuum Techniques, Boston, 1955.

<sup>13</sup><https://github.com/robertjensen/FlightTime>.

<sup>14</sup>R. Imbihl, A. Scheibe, Y.F. Zeng, S. Gunther, R. Krahnert, V.A. Kondratenko, M. Baerns, W.K. Offermans, A.P.J. Jansen, and R.A. van Santen. Catalytic ammonia oxidation on platinum: mechanism and catalyst restructuring at high and low pressure. *Phys. Chem. Chem. Phys.*, 9(27):3522–3540, 2007.

<sup>15</sup>Y.F. Zeng and R. Imbihl. Structure sensitivity of ammonia oxidation over platinum. *Journal of Catalysis*, 261(2):129–136, January 2009.

## Paper 3

### An Open Source Data Storage and Visualization Backend for Experimental Data

In preparation. To be submitted to Journal of the Association for Laboratory Automation.

# An Open Source Data Storage and Visualization Backend for Experimental Data

K. Nielsen, T. Andersen, R. Jensen, J.H. Nielsen and I. Chorkendorff

June 4, 2012

## **Abstract**

This is the paper's abstract...

## **1 Introduction**

In every experimental laboratory the need for acquisition and subsequent logging of data is essential. The acquired data from a given experiment is typically stored locally on a laboratory computer and is often acquired in highly specialized proprietary software tightly integrated with the experimental equipment by the manufacturer. These software suites often saves to closed proprietary formats which are difficult to exchange across several computers (e.g. a laboratory computer and a office computer) as specialized software both to read and export the data files is required. The software furthermore typically also requires additional licenses increasing complexity and cost. The exchange of acquired data between different computers with different operating systems, setup etc. is hence cumbersome and difficult due to the nature of closed proprietary formats.

To avoid difficult data exchange and simplify data processing an open source software platform is a much more attractive solution[1, 2, 3]. To accommodate these demands we

have written an open source platform for saving, logging, treating and visualizing experimental data.

In the present work we describe a totally open source system consisting of data acquisition, storage in a centralized database and a comprehensive display module including simple data treatment algorithms licensed as open source software.

## 2 System description

The system consists of three logically separate components as illustrated in Figure 1; 1) the equipment component where all communication with equipment and acquisition of data is performed 2) the servers which consist of the MySQL server that stores the acquired data from experiments and the Apache webserver which interacts and presents the user with data retrieved from the database and 3) the user component which consists of the clients wishing to access the data.

The system is highly flexible meaning the servers can accept data from a range of different sources. In the current setup equipment interfaced with RS232, GPIB, USB and analog/digital data acquisition cards standards are logged to the MySQL database. The user can furthermore use programs written in a wide variety of languages. As a testimony to this, software written in both LabView and Python[4] are used to save data to the database. How the integration with the server and subsequent storage of data in the database is performed is hence a user determined design decision. This has a number of advantages. The user(s) can integrate existing software with the databases quickly and without the need to rewrite any previous interface software written for experimental setups. Furthermore, due to the flexibility of the system, if storage in the database during acquisition is not possible due to software limitations the data can still be saved in the database by subsequent post experiment parsing of data files. This, however, still requires that the file format, which holds the data, is specified or the data can be exported to a flat

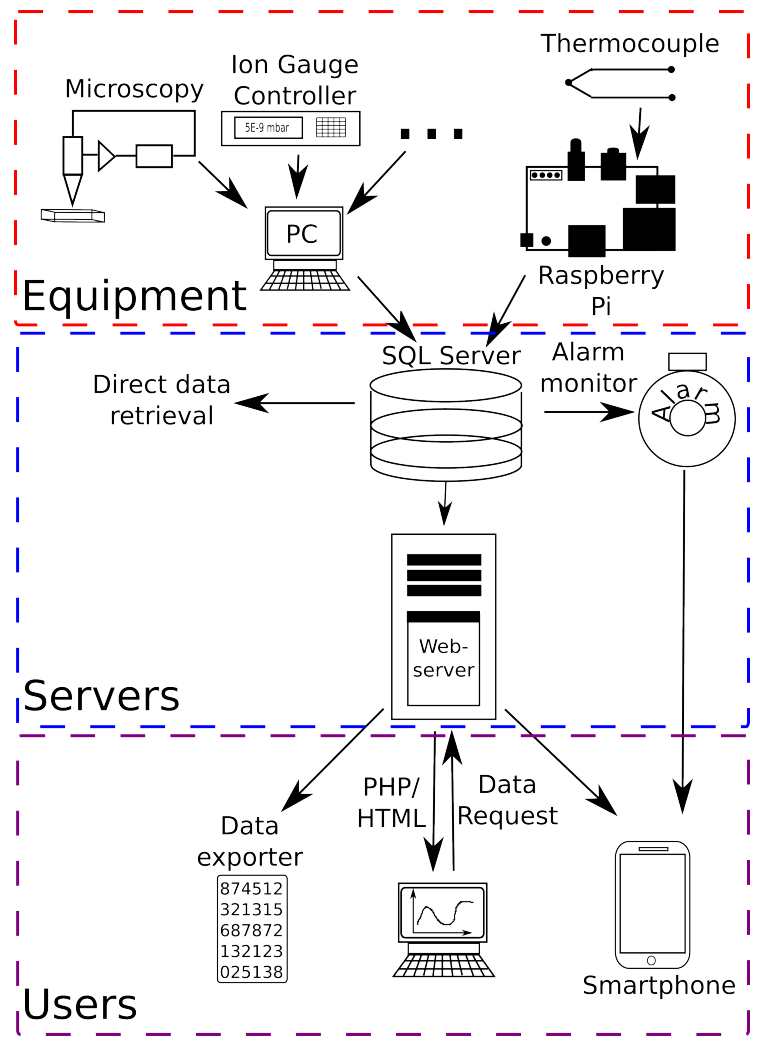


Figure 1: A schematic representation of the structure of data handling system.

text format from the acquisition software.

The servers consist of a MySQL server and a web server. All experimental data acquired by the user is stored in the MySQL database and is presented to the user from the web server. If needed, experimental data from the MySQL server can be retrieved directly for later analysis. The web server runs a LAMP (Linux, Apache, MySQL, PHP/Python) package. Python, PHP and HTML/CSS and is used to extract data from the database and present them to the end user in a simple interactive web interface for data visualization and simple treatment algorithms. Python was primarily chosen due to its tight integration with scientific packages, such as SciPy and NumPy, which makes data analysis and treatment more convenient[5]. PHP and HTML/CSS is used to display data in standardized formats suitable for web browsers and process input from the user. The combination of PHP and HTML/CSS to process user input from web pages is very flexible and has proven successful in other parts of the scientific community[6]. To accommodate a range of users and provide the largest flexibility the web server displays both a standard HTML/CSS site for desktop PCs and a mobile version suitable for tablet/smartphone users.

The web interface, which takes user input and displays data to the user, is also capable of routine data treatment. This can either be zoom of data, plotting on a log scale, performing a running average, etc. The data treatment is easily extendable allowing the user to add any function necessary. In this way the user can easily and quickly get an overview of acquired data.

### 3 Data aquisition

In research departments consisting of several experimental setups decentralized data acquisition from independent clients to a central server is the most attractive solution. This is due to the larger flexibility of the system, lower probability of dataloss and to simplify the backup of all experimental data. To be able to save acquired data from a range of

different computer hardware and instrumentation interfacing of many types of equipment is necessary.

In practice this is achieved by formulating a set of general design goals that will serve as computer language and hardware independent pseudo-code which will help the process of designing a new acquisition client to obtain conformity of the system. The design goals of our implementation are:

- \* To minimize data loss and to provide live data access in the laboratory from the server all clients must store data for as short amount of time as possible before handing of the data to a central server. Preferably, the data should be stored on the server as soon as it is acquired. For data being recorded over longer time-spans this means that data must be live-streamed to the server.

- \* To avoid data-loss in the event of no network connection or maintenance of the central server all clients collecting critical data must implement a local queue that will temporarily hold data until the central server can again be accessed. The client must continuously check if the server is available again and as soon as possible deliver queued data to the server.

- \* For continuous measurements (e.g. temperature of pumps, pressure in vacuum chambers, etc.) data logging must be implemented in a way that ensures that all significant events are recorded and at the same time does not use excessive amounts of storage. This is typically implemented by sampling data with a much higher rate than they are recorded. The local client will then, based on relevant heuristics, decide whether a new data point should stored on the server. This is implemented by waiting for either a given relative change in the signal or a predefined time since last recording of a data point. An example of such an implementation is shown below.

```
max_time_between_points = 600; deviation = 0.1
now = time.time(); current_measurement = get_measurement()
time_triggered = (now - last_recorded_time) > max_time_between_points
```

```

value_triggered = not (last_recorded_value * (1-deviation)
                      < current_measurement <
                      last_recorded_value * (1+deviation))

if time_triggered or value_triggered:
    last_recorded_value = current_measurement
    last_recorded_time = now
    send_measurement_to_db(now, current_measurement)

```

\* For stand-alone offline measurements (e.g. spectrometry, electrical characterization, etc.) it is important to measure as much metadata as possible to ensure that all information connected to the experiment is preserved. Along with accurate time information this will ensure that questions that were not yet formulated at the time of the experiment can in some cases be answered in retrospect using the metadata along with the continuously measured data.

## 4 Data storage

For storage of acquired data a centralized server has been implemented as opposed to other non-centralized systems[7]. Storing all acquired experimental data in a database on a centralized server running open source software has a number of attractive features. Firstly, by storing the data on a centralized server, backup of all experimental data is enormously simplified compared to backup of individual computers. Backup of experimental data is, hence, from a user's point of view automatic as this can be performed by routine jobs on the server. Secondly, the data is stored in a standardized and open format which allows for easy export of the data to any platform, open formats or software source. This makes data exchange across different platforms immensely more simple. Thirdly, by open sourcing all of the code used to visualize and treat data from the database, collaboration between several different groups is possible thus increasing the number of developers to

optimize the code and further increase functionality.

A centralized storage of data can be accomplished in many ways. However, in experimental laboratories where large amounts of data are recorded a database is an obvious choice for storage. To keep the server backend simple a relational database has been chosen. As specific implementation MySQL has been chosen due to its GNU General Public License[8], simplicity, fast performance, flexibility and scalability.

A system design of many highly decentralized clients all pushing data continuously to a central MySQL server requires high server performance, high uptimes as well as a flexible storage ensuring easy expansion of storage space if needed. To ensure these properties of the system it has been implemented with as few modification to the configuration of the standard server software as possible, which helps to ensure that this central component can easily be managed by the professional IT-staff at the department. It is important to realize that while the clients can easily have the "age diversity" of accumulated scientific equipment, be exposed to harsh conditions in the lab and be managed by the scientific staff the server needs to be managed and handled with all the care associated with a production environment server.

To protect against pollution of the various setups tables in the database each client has its own username and password which is not part of the code (typically it will be managed in the local ODBC-settings of the client). In this way, interface code can flow back and forth between different setups without the risk of one setup accidentally logging data to other setup's tables.

For each of the setups that is connected to this system, the following table structure is implemented. Each of the measurements that are continuously logged has their own table, where the values are logged as a function of date and time. All the specific measurements, such as spectra, scans and values monitored over a well-defined time span are stored in two tables in the database, a metadata table and a data table. In the metadata table **all** metadata pertaining to the measurement is saved in one row. In the data

table xy-values and a measurement id is saved in one row per xy-value entry. The metadata in the metadata table is then connected to the data points in the data table by a unique id attached to each xy-value entry. This structure is a compromise between space usage and simplicity as it leads to extra space being used to store the measurement id once for every data point. This, on the other hand, makes it possible and simple to store all the different kinds of xy-data in just two tables.

## 4.1 Data extraction

The flexible nature of SQL allows one to extract data in many ways. Complete datasets, data in a certain time interval for a continuously logged measurements or data pertaining a specific measurements can be retrieved by simple statements,

```
SELECT * FROM table_name  
SELECT * FROM table_name WHERE time BETWEEN {from} AND {to}  
SELECT * FROM table_name WHERE measurement={id}
```

(where the entities marked by {} are variables that should be replaced with specific values)

This data can then be handled using the programming environment most comfortable for the user and can be used to perform automatic reporting, data treatment or as input to scripts that will produce plots based on the data. SQL also allows for very efficient data treatment directly from the SQL-server, which can be very useful to get a quick overview of the acquired data, as illustrated e.g. in section 6.1.

A further advantage of SQL servers is the standardization, which makes it easy to change the choice of implementation, if it is wanted for some reason. Several open source implementations of SQL-servers exists including Firebird, PostgreSQL, Oracle, Mimer SQL.

## 5 Data access

As mentioned in section 4.1 it is both possible and very easy to access data directly from the database using either direct SQL statements or programming. This is very practical for the cases where it is desired to perform data treatment on the data or to produce high quality graphs. However, most of the time it is sufficient to simply look at the data and possibly perform light data treatment. For this kind of data analysis it would be highly impractical to write small custom pieces of software for each kind of data that the users wish to look at. For this reason we have developed a framework for visualization of the stored data that allows quick and easy access to all data. The framework includes support for basic data treatment as well as the option to plot several data sets at the same time for easy comparison of results and to export the data to local files.

The goal for the visualization module has not been to provide high quality plots since this is a large task that is best solved with either dedicated software suites or custom scripts. Instead, the quality of the plots was targeted such that it is sufficient for different kinds of everyday use including presentations at informal group meetings, as starting point for discussion of data, quick data comparison etc. To realize this form of visualization a frontend/backend topology has been implemented. The code that handles user input is retrieved in HTML and PHP thus allowing user input to be acquired from a web browser. The backend consists of an open source plotting library, interface code to feed data into the plotting code and plot preferences specific to each experimental setup. The backend is mainly written in Python and the configuration read from a XML file unique to each setup. The preferences file contain a settings section for each different kind of plot. Below is shown an example of a continuously logged pressure:

```
<!-- PRESSURE -->  
<graph type='pressure'>  
<query>SELECT unix_timestamp(time), pressure FROM pressure_SETUP
```

```

where time between " {from}" and "{to}" order by time</query>

<ylabel>Pressure / Torr</ylabel>
<title>Pressure in {setup}</title>
<default_yscale>log</default_yscale>
<default_xscale>dat</default_xscale>
</graph>
```

The system is flexible towards choice of plotting library which is a great advantage since different plotting libraries are optimal for different tasks. At the moment all plotting is performed by matplotlib[9]. As a testimony to the flexibility of the setup we have moved from our original backend based on JpGraph[10] to a backend based on matplotlib without significant changes to the backend code. Currently, we are investigating moving some of the display code to the JavaScript based dygraphs[11] thus producing a dual display system since this plotting library allows for real-time manipulation of the data using a mouse through an ordinary web browser.

## 6 Cases

The existence of this data system is paramount to several automation and system health monitoring tasks in our lab. Below a few examples are described of the use of the data system for these purposes. The examples given are how to create a system health development graph from the continuously logged pressure data, how we use the continuously logged data to monitor the health and status of long duration experiments from home and finally how it can be used to create alarms if some of the system parameters fall outside specified security ranges.

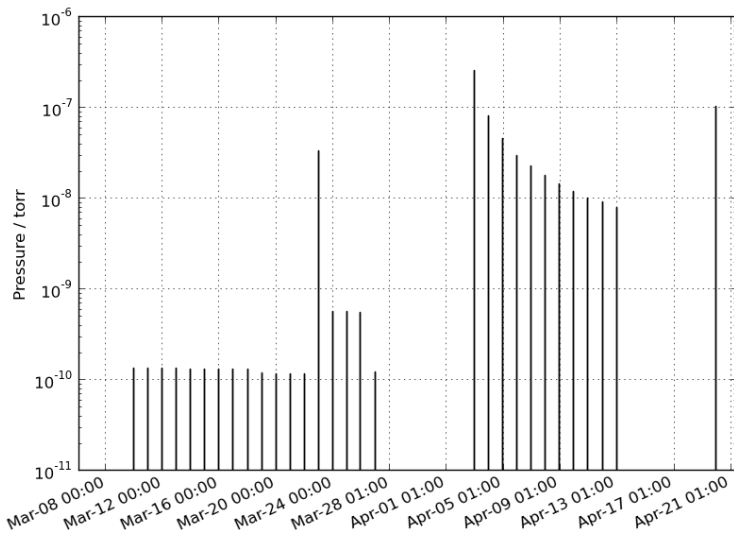


Figure 2: The morning pressure in a vacuum chamber at the department. The pressure gauge is unable to read high pressures, and thus no data is available from periods where the chamber is vented for maintenance.

## 6.1 Monitoring system health

As mentioned in section 4.1 the flexibility of SQL provides the possibility to do advanced data selection and very efficient elementary data treatment directly in the database by means of the SQL query. This can be used as in the example below, where the pressure in a vacuum chamber at 1 A.M. in the morning (where all the system parameters have settled down) for the last month is extracted for plotting;

```
SELECT DATE(time), AVG(pressure) FROM pressure_microreactor WHERE hour(time) = 1 AND
minute(time) BETWEEN 00 AND 20 AND time BETWEEN {from} AND {to} GROUP BY
date(time) ORDER BY time DESC LIMIT 30;
```

where {from} and {to} should be replaced with the relevant date interval.

The output from a statement such as the one above is illustrated in Figure 2. Plots like these can be a useful tool to monitor the general health of the chamber, i.e. if leaks have developed, a valve is failing, a roughing pump is malfunctioning etc. It should be mentioned that this is a function that has been sought after for quite some time as ultra

high vacuum is required for surface science studies. Previously, this has simply not been possible before the automated logging and selective plotting, as it would have required a person to log the data in the middle of the night and to manually periodically make new plots of the latest time period.

## 6.2 Status of experiments with long durations

Within surface science it is not unusual to have experiments or a preparation procedures before an experiment running for extended periods of time i.e. overnight, or over several days. Obviously, for such procedures running when no-one is present to monitor it, the programs that execute the procedure are themselves responsible for the safety of the system/equipment and for shutting it down if something unintentional happens. But with continuous logging, it is now a simple task to add surveillance to these procedures that alerts the user if the procedure has been stopped. When this happens, it is then possible for the operator to access if it is safe to start the experiment again, even from home. This can help to prevent a loss of experimentation time if the experiment stopped e.g. during unsupervised experimentation time intervals like a weekend.

One example where this is used is for the cleaning of metal single crystal samples before experimentation. The cleaning of the surface is achieved by running a number (5-20) of cleaning cycles. Each of these cycles can take up to several hours. Before this task was automatized, it typically required simple manual intervention 2-4 times during a 30 to 120 minute cycle. Obviously, this was a suboptimal solution, since a lot of time was spent, with only small time intervals to work on other things, before the next manual intervention. After the total automation of the task and the implementation of the surveillance features mentioned above this procedure can now run e.g. for 10-16 hours over night and produce a sample ready for experimentation at the beginning of the workday.

Another use of the monitoring of extended procedures are in the experiments on microreactor setups [12]. For these devices, it is very common to have quite long experimen-

tation times. They can be used to allow for sufficient system settle time when parameters have been changed, to study long time stability effects on the samples or to thoroughly search the parameter space for the experiment. Obviously, for all these purposes the more experimentation time the better and being able to un-problematically and safely utilize nights and weekends is a noticeable improvement.

### **6.3 Cooling water alarms**

Several important pieces of equipment in our lab require cooling. If the cooling disappears it can result in the break down of this equipment, which can be quite expensive both in repair costs and lost equipment up-time. Using the continuously logged data critical system parameters can be monitored and used to trigger alarms when these fall out of specified ranges. To use this feature to implement surveillance of the cooling temperature measurements on all the equipment with critical cooling requirements have been mounted and all of these temperatures logged via the data system. This approach has the desirable side effect that system health can be monitored (to the extent it is given by the temperature) of each piece of equipment individually to evaluate if the equipment is getting old or requires maintenance. To implement the alarms a program has been written that retrieves the latest temperatures from the database, compares them with values from a previous time interval and sends out an alarm via email if they increased out of range. Appropriately coupled with email alarms, e.g. on smartphones, this feature provides the real-time user notification of critical cooling loss.

## **7 Summary**

...

## References

- [1] Neil D. Benn and Joe Liscouski. Discussion of open-source methodologies in laboratory automation. *Journal of the Association for Laboratory Automation*, 14(2):82–89, April 2009.
- [2] Glenn A. Murray and David P. Crocker. Applying open-source software to laboratory data management. *Journal of the Association for Laboratory Automation*, 16(5):327–334, October 2011.
- [3] I. So, D. P. Siddons, W. A. Caliebe, and S. Khalid. Hard real-time quick EXAFS data acquisition with all open source software on a commodity personal computer. *Nuclear Instruments & Methods In Physics Research Section A-accelerators Spectrometers Detectors and Associated Equipment*, 582(1):190–192, November 2007.
- [4] <http://www.python.org/>.
- [5] Matthew H. Cahn and Mark F. Russo. Python and automated laboratory system control. *Journal of the Association for Laboratory Automation*, 12(1):46–55, February 2007.
- [6] M. K. Crane, L. J. Storrie-Lombardi, N. A. Silbermann, and L. M. Rebull. MySQL/PHP web database applications for IPAC proposal submission - art. no. 701626, 2008.
- [7] Roger L. McIntosh and Alfred Yau. A flexible and robust peer-to-peer architecture with XML-based open communication for laboratory automation. *Journal of the Association for Laboratory Automation*, 8(1):38–45, February 2003.
- [8] <http://www.gnu.org/licenses/gpl.html>.
- [9] <http://matplotlib.sourceforge.net/>.
- [10] <http://jpgraph.net/>.

[11] [http://dygraphs.com/.](http://dygraphs.com/)

[12] T. R. Henriksen, J. L. Olsen, P. Vesborg, I. Chorkendorff, and O. Hansen. Highly sensitive silicon microreactor for catalyst testing. *Review of Scientific Instruments*, 80(12):124101, December 2009.